Nanoporous Elements in Microfluidics for Multi-scale Separation of Bioparticles

by

Grace Dongqing Chen

B.A. Engineering, University of Cambridge (2006)
M.Eng. Electrical Engineering, University of Cambridge (2006)

Submitted to the Division of Health Sciences and Technology
in partial fulfillment of the requirements for the degree of

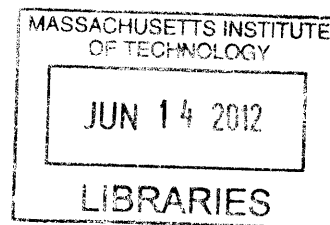Doctor of Philosophy in Biomedical Engineering

at the

MASSACHUSETTS INSTITUTE OF TECHNOLOGY

June 2012

Signature of Author: _____

Harvard-MIT Division of Health Sciences and Technology
March 27rd 2012

Certified by: _____

Mehmet Toner, PhD
Professor of Bioengineering and Health Sciences and Technology
Thesis supervisor

Certified by: _____

Brian L. Wardle, PhD
Associate Professor of Aeronautics and Astronautics
Thesis committee chair

Accepted by: _____

Ram Sasisekharan, PhD
Director, Harvard-MIT Division of Health Sciences and Technology
Edward Hood Taplin Professor of Health Sciences & Technology and Biological Engineering

Nanoporous Elements in Microfluidics for Multi-scale Separation of Bioparticles

by

Grace Dongqing Chen

Submitted to the Division of Health Sciences and Technology
in partial fulfillment of the requirements for the degree of
Doctor of Philosophy in Biomedical Engineering

Abstract

The efficient isolation of specific bioparticles in lab-on-a-chip platforms is important for many applications in clinical diagnostics and biomedical research. The majority of microfluidic devices designed for specific particle isolation are constructed of solid materials such as silicon, glass, or polymers. Such devices are hampered by some critical challenges: the low efficiency of particle-surface interactions in affinity based particle capture, the difficulty in accessing sub-micron particles, and design inflexibility between platforms for different particle sizes. Existing porous materials do not offer the structural properties or patterning capabilities to address these challenges. This work introduces Vertically Aligned Carbon Nanotubes (VACNTs) as a new porous material in microfluidics, and demonstrates the different ways in which it can improve bioparticle separation across both the micro and nano size scales.

Our devices are fabricated by integrating patterned VACNT forests with ultra-high (99%) porosity inside of microfluidic channels. We demonstrated both mechanical and chemical capture of particles ranging over three orders of magnitude in size using simple device geometries. Nanoparticles below the inter-nanotube spacing (80 nm) of the forest can penetrate inside the forest and interact with the large surface area created by individual nanotubes. For larger particles (>80 nm), the ultra-high porosity of the nanotube elements enhances particle-structure interactions on the outer surface of the patterned nanoporous elements. We showed using both modeling and experiment that this enhancement is achieved through two mechanisms: the increase of direct interception and the reduction of near-surface hydrodynamic resistance. We verified that the improvement of interception efficiency also results in an increase in capture efficiency when comparing nanoporous VACNT post arrays with solid PDMS post arrays of the same geometry, using both bacteria and cells as model systems. The technology developed in this thesis can provide improved control of bioseparation processes to access a wide range of bioparticles, opening new pathways for both research and point-of-care diagnostics.

Thesis supervisor: Mehmet Toner

Title: Professor of Surgery and Health Sciences and Technology

Acknowledgments

First and foremost, I would like to thank my thesis advisor, Mehmet Toner, for guiding me through my whole PhD process. He gave me freedom to explore different ideas, but is always there to point me in the right direction when I needed it.

A big thank you to my committee chair Brian Wardle, who also took on the role of a co-advisor in the past couple of years. His energy and enthusiasm really made the project fun to work on, and his expertise on CNTs was critical to its success. Thanks also to my committee member Jongyoon Han, for the generosity with his time and valuable input.

Special thanks to my collaborator extraordinaire, Fabio Fachin, who not only fabricated all the CNT samples used in my experiments, but was there brainstorming with me on every experiment and every paper. He was truly a joy to work with, and I'm glad that we have now turned him to the 'bio'-side of engineering!

A heartfelt thank you to Bill Rodriguez, who inspired me to work on point-of-care diagnostics in the first place, and who continues to be so generous with his time and advice even with his busy schedule as a CEO. Thanks also to everyone else in (or previously in) the global health diagnostics group: Marta Fernandez-Suarez, Xuanhong Cheng, Sukant Mittal, Anh Hoang, Dylan Tierney, Aaron Oppenheimer, Ali Yanik. I am grateful for their feedback, and even more grateful for their friendship, over the years.

I would like to thank all the lab managers at the BioMEMS Resource Center, past and present: Octavio Hurtado, A.J. Aranyosi, Harrison Prentice-Mott, Bashar Hamza, and Vijay Ambravaneswaran, for helping me with all my fabrication needs and always coming up with creative solutions to any problems. Vijay, you will always be remembered.

Thanks to everyone else at the Center for Engineering in Medicine, for letting me borrow cells and reagents, for help with microscopy and chemistry and other day-to-day issues, and for stimulating lunch time conversations. I truly enjoyed my interactions with everyone here.

I would not be here without the support of family and friends. The biggest thanks goes to my parents, who supported my decision to come to the US even though it meant separation from their only daughter by half a globe. Special thanks to my grandfather Chen Lian He, whose life lessons I will always remember, and who, despite never going to university, is one of the most intelligent and erudite people I know. Thanks also to the rest of my extended family in Chongqing, who welcomes me back every time from my long absence as if I had never left. It means a lot to me.

The final thanks goes to my soon to be husband, Eric, who has been with me every step of the way, and provided me with laughter, strength and encouragement throughout the whole experience.

Contents

List of Figures

11

List of Tables

Chapter 1

Introduction

The efficient isolation of specific bioparticles in lab-on-a-chip platforms is important for many applications in clinical diagnostics and biomedical research. Such particles, including cells, bacteria, and viruses, can span more than three orders of magnitude in size. The majority of microfluidic devices designed for specific particle isolation are constructed of solid materials such as silicon, glass, or polymers. Such devices are hampered by some critical challenges: the low efficiency of particle-surface interactions in affinity based particle capture, the difficulty in accessing sub-micron particles, and design inflexibility between platforms for different particle types. Existing porous materials, consisting mainly of 2-dimensional porous membranes, or monolithic porous plugs, do not offer the structural properties or patterning capabilities to address these challenges. The goal of this thesis is to introduce Vertically Aligned Carbon Nanotubes (VACNTs) as a new porous material in the microfluidic toolkit, and to demonstrate the different ways in which it can improve bioparticle separation across both the micro and nano size scales.

1.1 Motivation

Most clinical diagnostics and basic research studies aimed at understanding the causes underlying disease require isolation of specific bioparticles from complex samples such as blood, sputum, and cell culture supernatant. Examples include circulating tumor cells and antigen-specific T-cells (10-20μm), respiratory bacteria such as *Mycobacteria tuberculosis* (~1μm), and viruses including the Human Immunodeficiency Virus (~100nm) and Hepatitis B Virus (~40nm). Figure 1-1 illustrates the richly diverse range of particles present in blood, and their typical concentrations. The information contained within these bioparticles hold the key to a wealth of information on the biological state of their host, both in health and in disease.
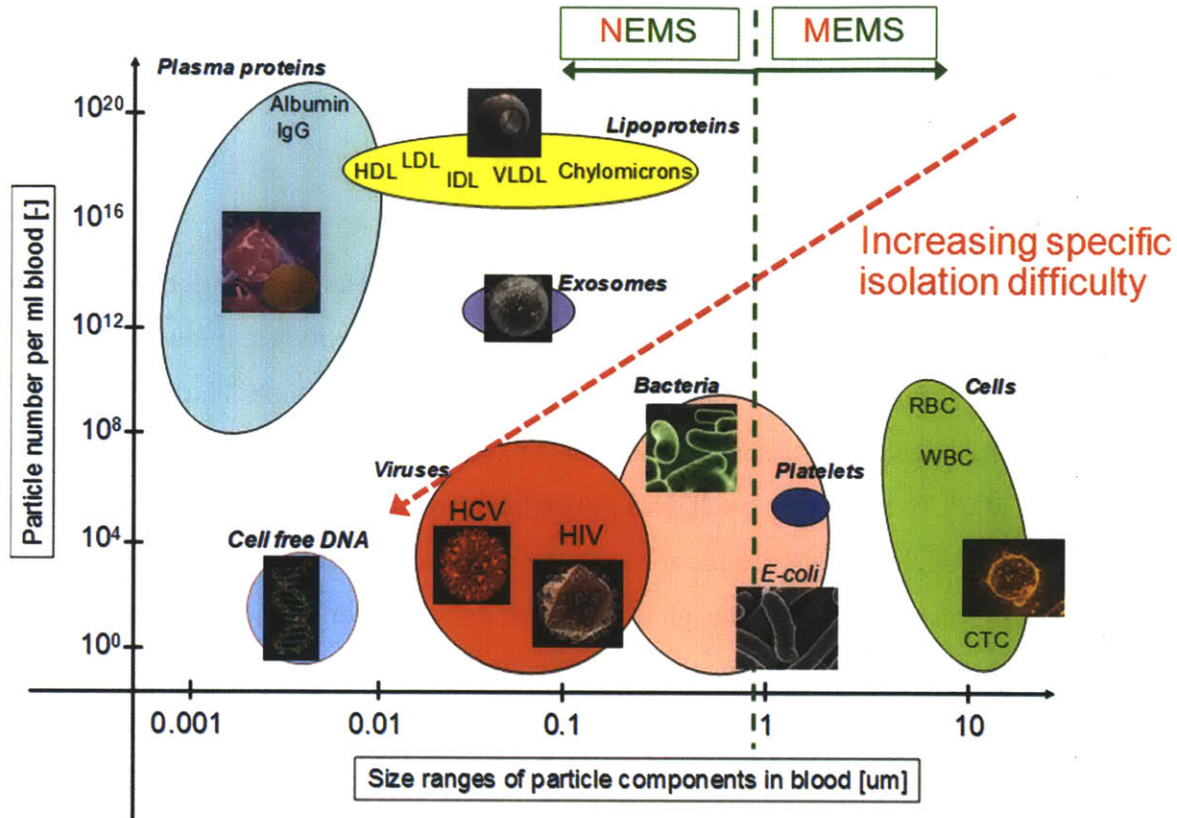
Fig. 1-1: Size and concentration ranges of bioparticles in human blood

Microelectromechanical Systems (MEMS), in particular microfluidics, has proven to be a valuable tool in the study of bioparticles, since the size range of its operation falls within the same scale as many of the larger bioparticles. However, accessibility to smaller, nanometer sized bioparticles has fallen in the realm of Nanoelectromechanical Systems (NEMS), through the use of nano-fabricated channels or nanoporous materials. In this work, we demonstrate a new method for incorporating nanoporous elements into microfluidics, to allow simultaneous access to a large spectrum of bioparticle sizes.

The majority of microfluidic systems designed for specific bioparticle isolation operate on the principle of immunoaffinity capture [14-16], where chemical binding moieties specific for the particle in question are attached to surfaces. The majority of these devices are constructed using entirely solid materials such as silicon, glass, or a polymer. However, the isolation efficiency of solid surfaces for particles suspended in liquid is extremely low. There are two main reasons for this. One is a bulk flow effect where flow stagnation occurs at the solid-liquid interface due to the no-slip boundary condition at solid surfaces. The other is a near-surface effect due to

14

hydrodynamic resistance as a particle approaches a solid surface. Previous devices using solid elements had to compensate for the low efficiency of each element by using large arrays occupying many square centimeters of footprint area in order to achieve the overall device efficiency they need.

Isolation efficiency is a function of the interception efficiency (the fraction of particles in flow that is intercepted by the collector) and the binding efficiency (the probability that a particle will bind to the collector if it is intercepted). This work focuses on the former. Different factors that affect interception efficiency in the flow regime of a typical microfluidic system were examined, and it was shown that interception efficiency can be greatly improved by using nanoporous elements instead of solid ones.

Until now, the inclusion of porous elements in microfluidics has largely been limited to membranes sandwiched between microchannel layers [17] or polymer monoliths that fill the inside of channels [18]. With membranes, geometrical control of the porous region is restricted to two dimensions, defined by the overlap between channels on either side of the membrane. Their application is mostly in size exclusion filtration and dialysis [17, 19, 20]. For polymer monoliths, examples have been limited to simple porous plugs in the channel that are commonly utilized for chromatography and solid phase extraction applications [21, 22]. A fundamental limitation to both of these techniques is the lack of geometrical control other than what is provided by the non-porous channel walls. This has restricted their application to simple size-based separation, and do not lend themselves to take full advantage of the exquisite control of fluid dynamics possible within microfluidics. In addition, the low porosity (5%-80%) of these materials means that when their pore sizes are adjusted to the nanometer range, their permeability is very low, thus severely limiting the sample flow rate at this scale.

In contrast, the nanoporous CNT elements presented in this thesis have an ultra-high porosity of 99%, while still maintaining sufficient structural rigidity to withstand flow inside a micro-channel. They allow for three-dimensional geometrical control of the porous elements independently from the channel boundaries: photolithography of the catalyst layer allows precise definition of the microscale geometry, and varying the time of growth can finely control the forest height. With these added levels of control and flexibility, this approach transforms the capabilities of porous elements in microfluidics to enable manipulation of fluid flow, particle

15

flow and molecular diffusion in ways that have not been previously feasible, opening up new capabilities and applications.

1.2 Thesis structure

This thesis introduces the incorporation of nanoporous VACNT elements in microfluidics, and showcases their advantages in bioparticle separation across different size ranges. Chapter 2 provides background on the current state-of-the-art in bioparticle separation, both at the macroscale and in microfluidic lab-on-a-chip systems. Some non-specific separation techniques are outlined, but focus is placed on specific particle capture methods. Current technologies in porous materials for microfluidics are also explored, as well as currently applications of carbon nanotubes in biology. Limitations of existing platforms for specific bioparticle separation are explained, providing the motivation for our study.

Chapter 3 presents the fabrication methodology and characterization of the nanoporous VACNT micro-devices. Our work represents one of the first efforts to combine VACNT forests into microfluidics. Although we use a previously developed method for the CNT growth, we had to develop new methods for integration of VACNT forests into microfluidic channels. We present two methods for achieving this, one of which allows for top sealing of the forest with the channel, and the other allows for both top and side sealing. The behavior of the VACNT elements in wetting and flow is characterized, and its permeability to liquid flow measured. When permeability measurements were conducted, we discovered that the material permeability of the VACNT forest is significantly higher than those known for other nanoporous materials, and is in fact comparable to that of many microporous materials. An analytical explanation is given as to why this is. We show that we can make adjustments to the permeability by varying growth parameters of the VACNT forest. Finally, we investigate different known functionalization strategies for CNTs to identify one most suited to our needs, and compare it to standard PDMS functionalization.

Chapter 4 explores various examples of particle separation, taking advantage of both the nanoscale porosity and the microscale patternability of the VACNT elements for mechanical separation, as well as the chemically functionalized elements for specific particle capture. We start with a simple mechanical filter that uses the nanoporosity of the VACNT forest as the

filtration cut-off size. Next, we functionalize the forest to allow specific capture of nanoparticles inside a rectangular filter whilst mechanically trapping microparticles in front of the filter. Then, instead of rectangular filters, we used a circular post to specifically isolate nanoparticles and microparticles on the inside and outside of the post respectively. We demonstrate simultaneous mechanical and chemical separation of three different particle types across four orders of magnitude in size, using an array of nanoporous microposts. Finally, we show isolation examples of real biological particles (bacteria and cells), and observe that capture efficiency is 5-7 folds higher with nanoporous capture elements compared to solid elements of the same external geometry.

Chapter 5 aims to understand particle interception of both solid and porous elements through theory and experiment. We chose the popularly used, and simple to model geometry of a cylindrical post. We begin in with some qualitative observations on interception improvement. Next, we examine the different factors that affect interception efficiency in the flow regime of a typical microfluidic system, and understand the mechanisms that limit interception in solid elements. We lay down the theoretical foundation for modeling mixed porous and free media flow, and continuo on to describe our own model for particle interception for solid and porous cylindrical posts. We put our model to the test against experimental results for particle interception using both isolated posts and post arrays. In each case, there is good agreement of theory and experiment to prove that we can greatly improve interception efficiency by using nanoporous posts instead of solid posts of the same geometry. Finally, we return to capture of real biological particles to show that the interception efficiency increase also translates to isolation efficiency enhancement.

Chapter 6 summarizes the main findings of the previous chapters and provides suggestions for future directions. Ideas for future work include refinement of the theoretical model, application of the device for specific particle capture from real clinical samples, improvement in control of the CNT forest geometry, and integration of particle capture with particle sensing.

Chapter 2

Background and Prior Work

Most clinical diagnostics and basic research studies aimed at understanding the causes underlying disease require isolation of specific biomolecules or cells from complex samples such as blood, saliva and cell culture supernatant. Unfortunately, these studies are sometimes hampered by the fact that the bioparticles of interest are present in the samples in very small quantities. This is the case, for example, of antigen-specific T-cells, circulating tumor cells (CTCs), or HIV viral particles for monitoring immune responses, cancer and AIDS progression, respectively. Section 2.1 will introduce traditional methods for bioparticle isolation in research and clinical laboratories. Microfluidics is increasingly becoming important as a tool for biological analysis and research. As miniaturized detection methods are becoming increasingly sensitive, capable of single cell [23, 24] and even single virus detection [25, 26] , efficient capture of specific bioparticles is now the rate limiting step to achieving complete lab-on-a-chip assays for particle identification. There is huge diversity in current microfluidic methods for bioparticle isolation, a selection of which will be introduced in section 2.2. Section 2.3 will additionally discuss current state of the art in porous materials in Microsystems, and their use in bioparticle separation. Section 2.4 will introduce carbon nanotubes (CNTs) and their current use in biomedical applications. Section 2.5 will discuss limitations in currently microfluidic particle separation technologies and how the work on patterned VACNT elements in microfluidics has the potential to overcome many of these challenges.

2.1 Bioparticle separation in clinical and research laboratories at the macroscale

The majority of methods currently used in clinical and research laboratories for bioparticle separation have been around for many decades. Most of these methods require multiple manual steps, large sample volumes (hundreds of microliters or more) and could take hours to complete. They are divided below into two major categories: methods that are primarily based on

18

differences in physical attributes between particles, and methods that incorporate specific biomolecular recognition.

2.1.1 Macroscale separation methods based on physical properties

Physical properties can include size, density, deformability, charge, mobility in an electric field. Methods that take advantage of these properties are often faster and higher throughput than the biomolecular recognition methods, but suffer from lack of specificity. As such, they are more often used for preconcentration upstream of a more specific selection or identification step.

Centrifugation: An indispensable tool in any clinical or research laboratory, the centrifuge accelerates the process of sedimentation that would naturally occur due to differences in density between bioparticles in suspension. The first centrifuges were introduced in the 19th century, and were hand-cranked (Fig. 2-1a). Now, ultracentrifuges in laboratories can reach relative centrifugal forces (RCF) of up to 1000,000g (Fig. 2-1b). In addition, a number of density gradient media are available for improving separation in certain applications. Widely used examples include Ficoll (a polysaccharide media used for separating blood into its cellular components), Percoll (a coilloidal silica media used for separating cells, viruses and organelles), and sugar media such as sucrose. The centrifuge is very often the first step in the preparation of a biological sample for analysis or bioparticle isolation, but it is rarely the only step.
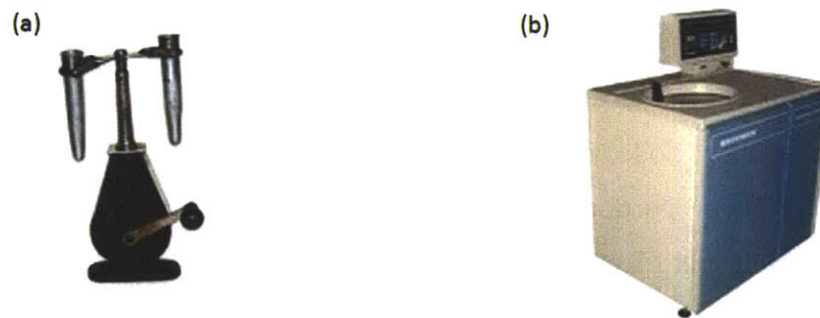
Fig. 2-1: (a) 19th century hand-cranked centrifuge [27] (b) modern day ultracentrifuge [28]

Size-based filtration: One of the simplest approaches to bioparticle separation is to use porous membranes to divide a population of particles into two via a geometrical size cut-off. To date, a large variety of membrane materials and fabrication methods have been developed, covering size ranges across multiple orders of magnitude. Commonly used membrane types in laboratory

settings include nitrocellulose, polycarbonate track-etch, PTFE, nylon and aluminum oxide. Membranes are typically used by clamping them inside of membrane holders, and frequent replacement is needed due to fouling and caking of membrane pores by particles. Because of the detrimental effects of fouling on separation efficiency, membrane filtration is more suited to dilute solutions with few particles, and like centrifugation, it usually only provides a first step in the particle separation process.

Chromatography: Chromatography is a collective term for a group of techniques that involve the passage of a mixed sample in a mobile phase through a matrix known as the stationary phase. Components within the sample can be separated by differences in their attenuation by the stationary phase. The stationary phase can take the form of a packed bed of beads, a monolithic column, or a flat piece of paper. Particles can be attenuated by surface charge (e.g. in ion-exchange chromatography), size (in size exclusion chromatography), or surface functionalization (in affinity chromatography). Affinity chromatography is a specific separation method and will be discussed in section 1.1.2. The following books offer comprehensive introductions to chromatographic techniques [29, 30].

Electrophoresis: When a dispersion of charged particles are placed under an electric field, they will migrate at different rates according to their electrophoretic mobility. This is one of the most widely used methods for separating proteins and nucleic acids due to its simplicity and relative low cost. Apparatus consists of a high-voltage supply, electrodes, buffer, and a support for the buffer such as filter paper, cellulose acetate strips, polyacrylamide gel, or a capillary tube. When the detergent SDS (sodium dodecyl sulfate) is used with proteins, all of the proteins take on a negative charge roughly proportional to their mass. The procedure SDS-PAGE (Sodium Dodecyl Sulfate PolyAcrylamide Gel Electrophoresis) is a standard means for molecular weight determination [31]. To increase separation resolution, electrophoresis can also be performed in two dimensions based on two different properties, for example mass and isoelectric point [32].

2.1.2 Macroscale separation methods based on specific recognition

The techniques introduced in this section all make use of specific biological interactions to select bioparticles of choice from a mixed sample. Examples of specific interactions include antibody-antigen, aptamer-target, enzyme-substrate, and receptor-ligand pairs. Of the methods below, fluorescent activated cell sorting and magnetic activated cell sorting are liquid phase

techniques, in which the specific ligands are mixed into the sample. Affinity chromatography is a solid phase technique, in which the specific ligands are immobilized onto a solid matrix.

Fluorescent Activated Cell Sorting (FACS): Flow cytometry is a widely used technique that allows identification of specific bioparticle from complex samples by fluorescently tagging the particle of interest and then probing all particles in the sample using laser beams. Hydrodynamic focusing is typically used to line up the particles so that they can be interrogated by the laser beam one by one. Fluorescence-activated cell sorting is a variation of flow cytometry that additionally allows for sorting of the cells into two or more populations based on their fluorescence results (Fig. 2-2 and [1]). It is a high-throughput and effective tool for bioparticle identification and sorting. However, the complexity, bulk, and costliness of the apparatus required limits its applicability outside of high volume clinical and research laboratories.
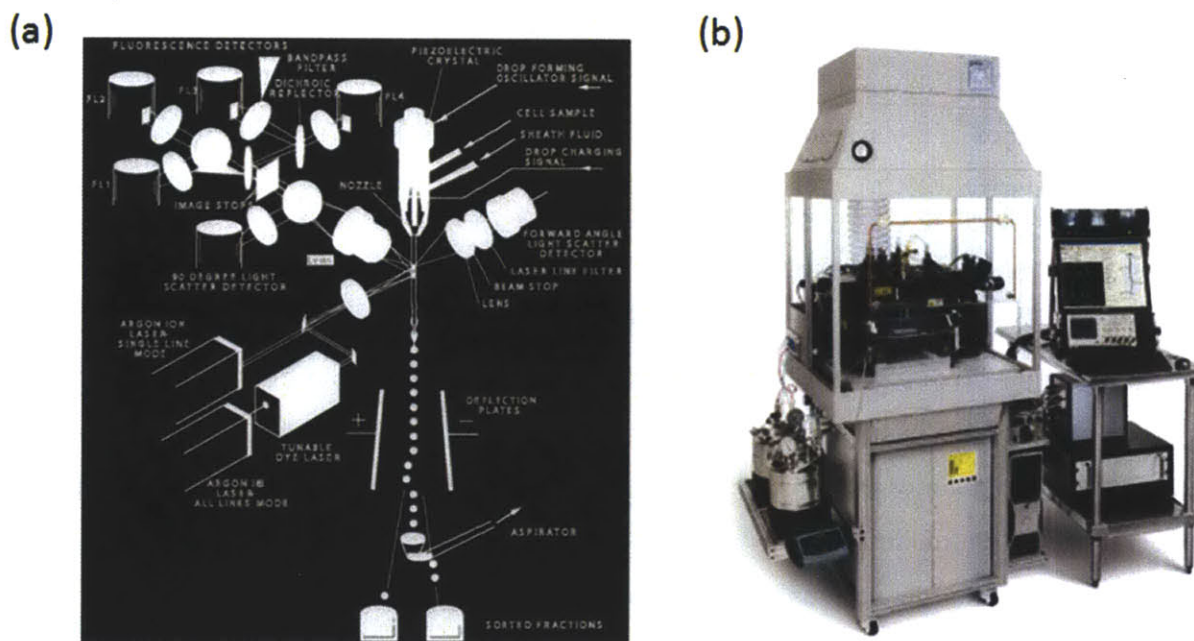
Fig. 2-2: (a) Schematic of a FACS machine [1]   (b) Example of a FACS machine set-up [33]

Magnetic Activated Cell Sorting (MACS): Magnetic bead-based separation is widely used in biology for the concentration and purification of a variety of bioparticles from complex samples [34-36]. The basic steps in magnetic separation are: 1) mixing and incubation of sample with functionalized magnetic beads to allow beads to bind with target analyte; 2) magnetic retention of beads and any bound analytes; 3) rinsing of the beads under magnetic retention to wash off unbound contaminants; 4) elution of the desired analyte into a final volume. Commercially, all

the steps are performed on the macro-scale either manually or with the aid of robotic systems. The whole process typically takes 1-2 hours to perform. Two types of beads are popularly used: micron sized (1-10um) beads with a paramagnetic core, and nanometer sized (20-100nm) beads with a superparamagnetic core. The magnetic cores are typically coated with silica or polymers that can then be functionalized to target the bioparticle of choice. Both types of particles are widely available commercially with a variety of surface chemistries.

Affinity chromatography: Affinity chromatography is a specific type of chromatography in which the stationary phase contains specific ligands for the target analyte [37]. The stationary phase may consist of a porous gel or a column of beads which is chemically functionalized (covalently or non-covalently) with the ligand of choice. The most commonly used matrix material is agarose gel beads, for which functionalization techniques are well known [38]. The sample is then allowed to flow through the functional matrix, onto which the bioparticles of choice are captured. However, because the pore arrangements inside the separation columns are random, the fluidics of the system is difficult to control, resulting in unreliable separation efficiency and purity.

2.2 Microfluidic bioparticle separation using solid materials

The advantages offered by microfluidics in the area of bioseparation have been one of the major drivers of advances in the field [39]. These advantages include small sample volumes, predictable fluid dynamics, faster separation times, low cost, disposable devices, and the ability to integrate detection modules downstream. As a result, a wide range of technical platforms have been developed that target various types of bioparticles. Microfluidic separation methods can again be categorized into those that rely only on differences in physical characteristics, and those that utilize specific biomolecular recognition. Some techniques are direct counterparts of macroscopic methods, whilst others are unique to microfluidics. This section covers only methods that use solid materials such as silicon, glass, polymers and metals, as structural elements. The use of porous materials in microfluidic separation will be discussed in the next section.

22

2.2.1 Microfluidic separation platforms based on physical properties

Microfluidic channels and features can be fabricated in the same length scale that mirrors many bioparticles of interest such as mammalian cells, yeast particles, and even bacteria cells. This allows the refinement of a number of physical separation methods such as optical tweezers, dielectrophoresis, and acoustic traps, to perform highly accurate levels of manipulation that would have been difficult at the macro-scale. The unique fluid dynamic properties at the micro scale also allows for the development of new flow-based separation techniques such as inertial focusing and deterministic hydrodynamics.

Filtration using patterned solid substrates: Porous membranes are widely used for filtration in microfluidics and will be covered in section 1.3. However, their integration into microfluidic devices is rather cumbersome. Some groups instead choose to photopattern porous barriers directly using the same substrate material as the rest of the microfluidic system. Examples include a micropatterned sieve for leukapheresis [40] and a micromachined high aspect ratio pillar array to trap beads [41]. There are a couple of major limitations to this technique. The first is the resolution of photolithography, which limits feature sizes to around a micron, even with the more expensive chrome photomasks. Thus nanometer range cut-off sizes are not usually achievable, except in the height dimension [42]. The second is filtration area, which is usually limited by the cross sectional area of the channel. In addition, the geometry of the gaps created this way tend to be rectangular slits rather than rounded pores, which may or may not be desirable.

Inertial focusing: The low Reynold number flow regime in most microfluidic channels means that viscous effects dominate over inertial ones. However, a group of techniques have been developed that take advantage of inertial forces at high flow rates for continuous bioparticle separation with very high throughput (Figure 2-3). Examples include the asymmetric curved channels by Dicarlo et al [2], spiral channels by Russom et al [43], and high aspect ratio straight channels by Bhagat et al [44]. Particles can be separated by size and shape.
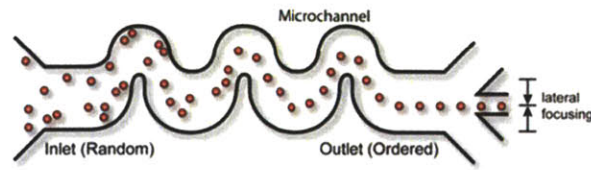
Fig. 2-3: Schematic of an asymmetrically curved inertial focusing channel [2]

Deterministic hydrodynamics: In contrast to inertial focusing, deterministic hydrodynamics takes advantage of the low Reynolds number, laminar flow regime typically found in microfluidics. The approach exploits the asymmetrical bifurcation of laminar flow around obstacles to deterministically sort particles based on their size. This technique is also known as "bumping", and it has been applied to the fractionation of micron-sized particles such as cells and bacteria [3, 45]. An experimental example of the bumping method is shown in Figure 2-4, where a silicon-based device for separating particles between $0.4\mu m$ and $1\mu m$ in in size is demonstrated.
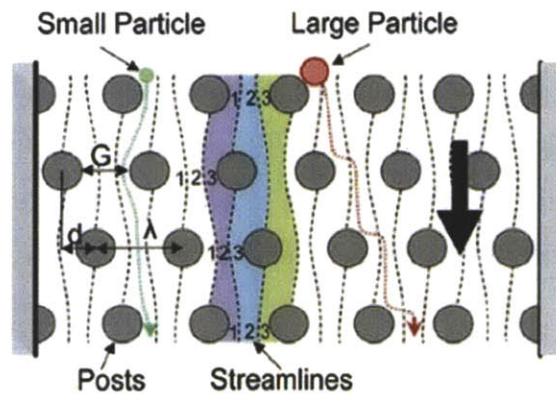
Fig 2-4: Schematic of particle separation by deterministic hydrodynamics [3]

Optical manipulation: Optical traps, the most common of which is the optical tweezer, consist of tightly focused laser beams that can confine dielectric particles in 3 dimensions. Optical traps are attractive in many microfluidic applications due to their non-contact, contamination free nature, and high precision. Manipulation of bioparticles ranging from several angstroms to 10 microns is possible [46]. It is also possible to use optical forces in cell sorting without trapping. For example Kovac et al. used optical forces to selectively release cells that have been trapped at the bottom of microfabricated wells [47].

24

Dielectrophoresis (DEP): When a dielectric particle is placed in a non-uniform electric field, it experiences a force as a result of the polarization induced by the uneven field. This phenomenon was first described by Pohl in 1951[48], and is the electrical analog of an optical tweezer. In one application, Voldman et al. developed a microfluidic cytometer where DEP was used to confine cells against fluid flow streams [49]. The micro cytometer consisted of a cell array chip, an optical system luminescently interrogating cells, and a control system for sorting (Fig. 2-5). DEP has been widely explored in microfluidics to manipulate bioparticles ranging from viruses, bacteria, to mammalian cells [50-52].
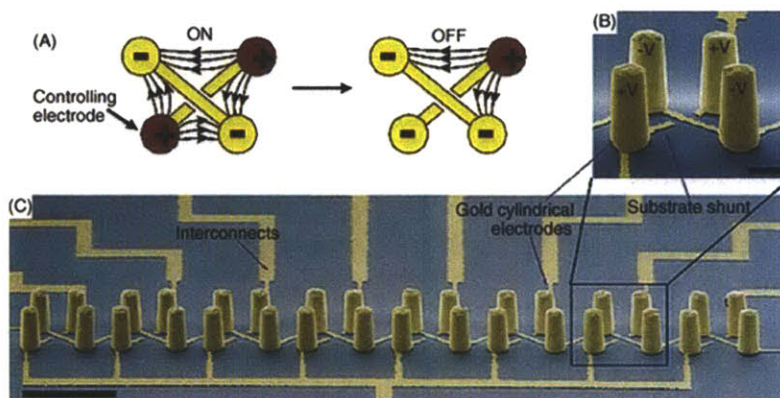
Fig 2-5: A microfluidic DEP cytometer (a) Schematic representation of operation. (b) Pseudocolored scanning electron micrograph (SEM) of a single trap consisting of four electroplated gold electrodes. (c) SEM of a completed 1×8 trap array. [49]

Acoustic trapping: Ultrasonic standing waves can generate stationary pressure gradients, which in a liquid medium will exert forces on particles. This has been used in microfluidics for non-contact trapping of cells or microparticles. A typical setup for creating acoustic standing waves is shown in Figure 2-6. Particles can be trapped in the nodal positions. Acoustic traps have been used for sample enrichment, enhancement of bead-based immunoassays, and 2-dimensional cell arrays [53-55].
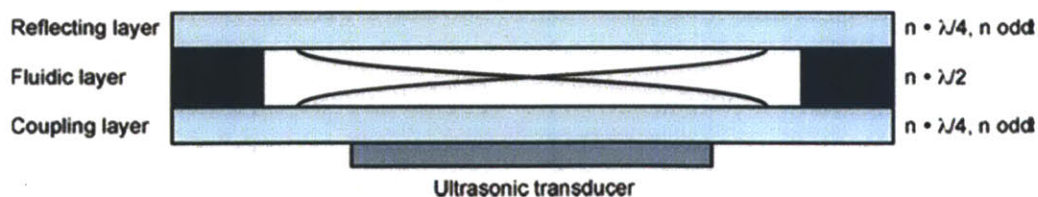
Fig. 2-6: Setup of a multilayer resonant structure. A standing wave is formed perpendicular to the flow and particles can be trapped at the nodal positions [4]

2.2.2 Microfluidic separation platforms using specific biomolecular recognition

The methods for specific bioparticle separation in microfluidics are closely derived from their macroscale counterparts. Liquid phase methods include microfluidic MACS and FACS, both of which require labeling of the sample. In contrast, microfluidic affinity chromatography is solid phase, and label free.

Functionalized magnetic beads: Many approaches have been described to adapt magnetic activated cell sorting (MACS) to microfluidics [56]. They can be broadly separated into passive or active traps based on the source of the magnetic field. In passive traps, the magnetic field is usually generated by a permanent magnet placed off chip, with on-chip nickel or iron elements to act as field gradient concentrators [5, 57]. For example, figure 2-7(a) shows patterned nickel strips under an external magnetic field that guide magnetic beads in one direction whilst non-magnetic beads travel in the direction of the flow [5]. In contrast, active traps use electrical power to generate magnetic fields through on-chip electromagnets. The most widely used design is that of a patterned planar coil at the base of the channel (Fig 2-7(b), [6]). On-chip micro-mixers can also be integrated to allow the functionalized beads to bind to the target bioparticle [57].
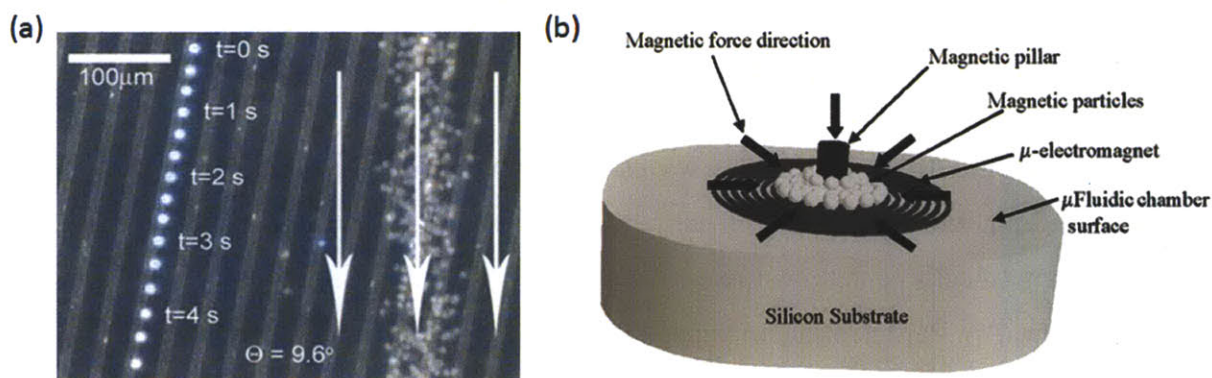
Fig. 2-7: (a) Passive magnetic separation with patterned nickel strips [5]. (b) Active magnetic separation with on-chip coiled electromagnet [6]

Microfluidic flow cytometry: The miniaturization of flow cytometry and fluorescent activated cell sorting has been an active area of investigation in microfluidics. For example, Wolff et al. [58] developed a pressure driven microfabricated high-throughput fluorescent activated micro cytometer which integrated a "smoking chimney" structure for hydrodynamic focusing of sample and cell sorting. Fluorescent activated cell sorting at a sample throughput as high as 12,000

26

cells/s at 100-fold enrichment can be achieved. Wang et al. [7] described a high-throughput microfluidic cell sorter with an all-optical control switch for live cells. A focused laser spot produces the optical force to deflect fluorescently identified cells to the target output channel (Fig. 2-8). Although the flow components can be successfully miniaturized, the need for bulky and expensive optics off-chip for fluorescent detection remains a major obstacle for widespread adoption of the technique.
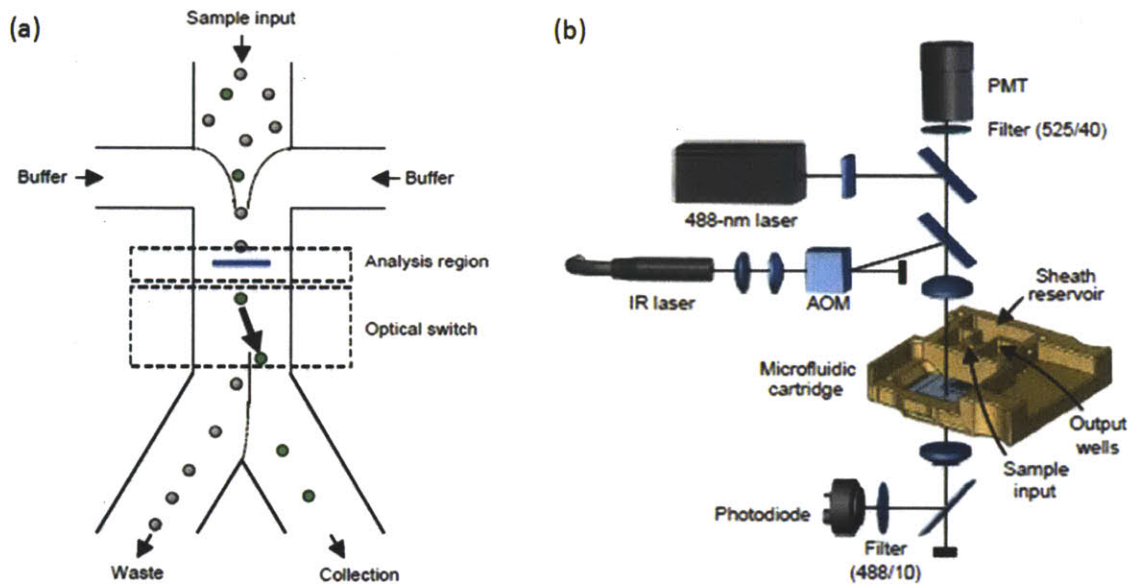
Fig. 2-8: an all optical cell sorter [7] (a) schematic (b) instrumental setup

Microfluidic affinity chromatography: The micron-range size scale of microfluidics and its predictable fluid dynamics has made it an attractive option for affinity chromatography of mammalian cells. There are several advantages of microfluidic affinity chromatography as a method for specific bioparticle separation compared to microscale FACS and MACS [14]: 1) It does not require pre-mixing the sample with labels such as fluorophores or magnetic beads. 2) It does not require bulky off-chip components such as lasers or permanent magnets. 3) The captured bioparticles are immobilized onto a solid matrix, allowing for simple addition of subsequent steps for detection, signal amplification, or cell lysis. 4) The predictable fluid dynamics allows for greater reliability of results, and additional degrees of control in the separation process. For example, Cheng et al. [8] developed a simple straight chamber microfluidic device for isolating CD4+ T-cells directly from whole blood for global health diagnostics (Fig. 2-9). They found that under certain flow regimes that result in specific shear

27

stresses at the channel surface, the capture of CD4+ T-cells is high, whereas the capture for CD4+ monocytes is low, which is desirable for their application.
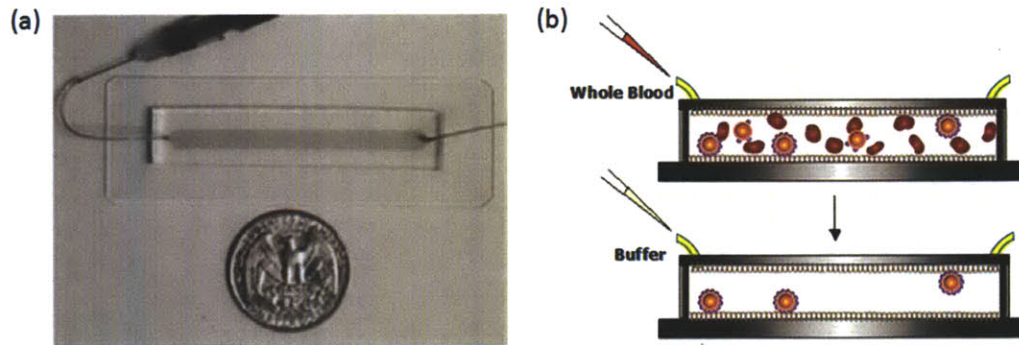
Fig. 2-9: Microfluidic chamber for separation of CD4+ T cells from blood [8] (a) device picture (b) schematic of CD4+ T cell capture from whole blood

Several groups have developed microfluidic devices for affinity capture of circulating tumor cells (CTCs) with high efficiency and purity [15, 59, 60]. The design by Nagrath et al. [59] consists of a silicon chip patterned with arrays of cylindrical posts through which whole blood from cancer patients are injected. The posts are functionalized with antibodies specific for epithelial cancer cells, which can be extracted from the patient samples and analysed for number and genotype. The design by Adams et al. consists of multiple parallel wavy channels, while Philips et al. used a simple rectangular channel with a height comparable to that of a tumor cell. All of these designs (Fig. 2-10) rely on large footprint areas, of many square centimeters, in order to ensure sufficient capture efficiency. This is due to the difficulty of ensuring sufficient interaction between particles in solution and the surfaces containing binding moieties (see section 2.5). Such large device areas are not only expensive to manufacture, but it is very difficult to scan and image the cells of interest after capture.
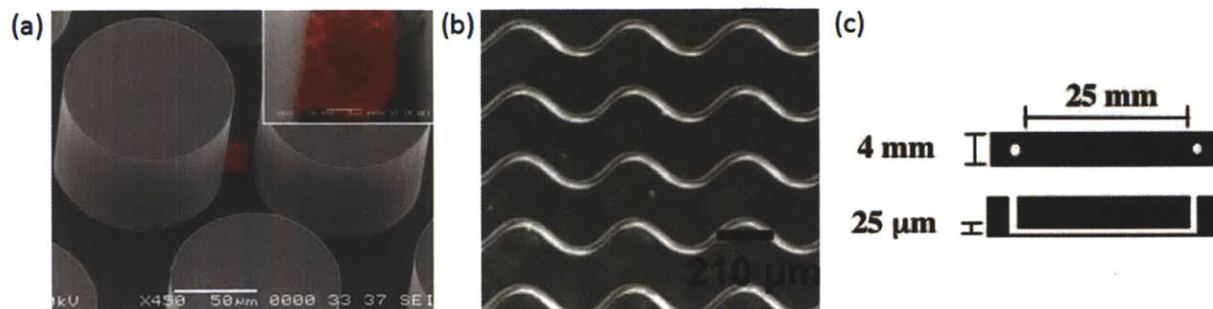
Fig. 2-10: Different microchip designs for CTC capture. (a) cylindrical silicon post array (b) parallel wavy channels in PDMS (c) rectangular PDMS channel

28

2.3 State-of-the-art in porous materials for microfluidics

Solid materials such as silicon, glass and polymers dominate as structural elements in microsystems including microfluidics. The inclusion of porous elements has thus far been limited to membranes sandwiched between microchannel layers [17] or monoliths that fill the inside of channels [18]. With membranes, geometrical control of the porous region is limited to two dimensions, and microscopic observation is usually only possible on the top side of the membrane. For porous monoliths, which can be fabricated from polymer or silicon, the porous region must be bounded on the sides by non-porous channel walls. Even with the limitations of these techniques, porous elements have found a wide range of biological applications including filtration, solid phase extraction, microdialysis, enzyme microreactors, micromixers, and cell culture [61].

Porous membranes: With the rapid growth of microfluidic tools for analytical systems, porous membranes have found their way into many of these systems as a method for particle separation, sample pretreatment, purification, or microdialysis [61]. In the majority of applications, commercially available porous membranes are directly incorporated into microfluidic devices by gluing or clamping (Fig. 2-11) [9, 20]. For example, Kim et al. [62] used multiple membranes on a single chip for removal of cells from blood, separation of HDL, and signal generation on a enzyme embedded membrane. Like other size based separation methods, the filtration achieved with porous membranes does not give specific particle selection. Furthermore, the 2-dimensional nature of porous membranes limit their geometrical definability.
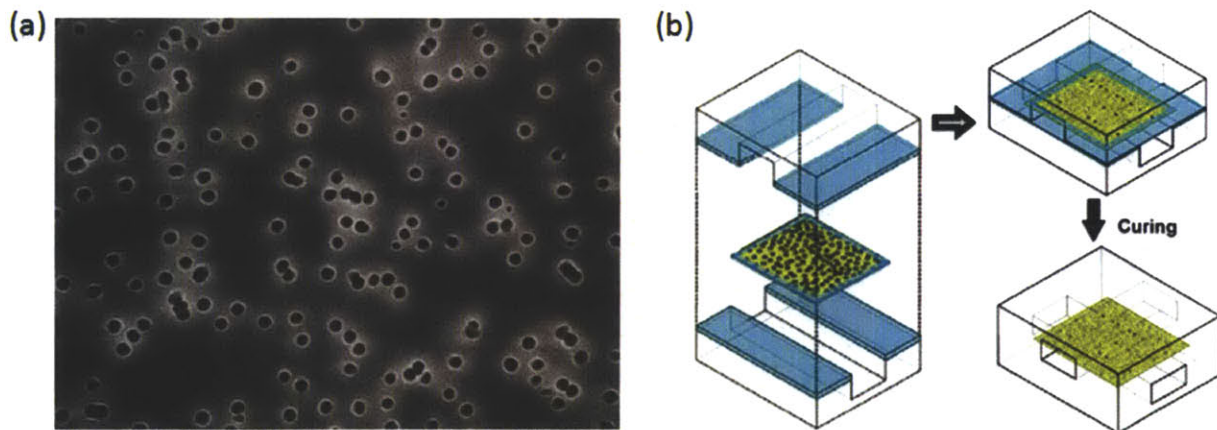
Fig. 2-11: (a) Structure of a track-etch membrane (Millipore). (b) Integration of a membrane into microfluidic channels by gluing [9]

Porous polymer monoliths: Porous polymer monoliths can be fabricated inside microfluidic channels as a porous plug, with boundaries defined by the solid channel walls (Figure 2-12). Free radical polymerization with UV initiation is the most commonly used method of fabrication. Monoliths with different porosity, surface area and flow resistance may be synthesized by tuning relative concentrations of monomers, organic solvents and free radical initiator [10]. Typically, the porosity achieved is between 40% and 70%, with pore sizes in the micron range. Due to their resemblance to the solid supports used in chromatography, their main areas of application have been along similar lines [63, 64]. They can also be functionalized to enable specific bioparticle targeting [65].
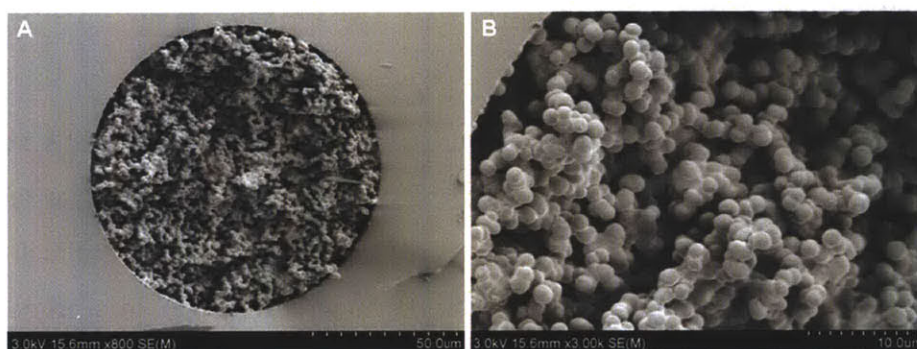
Fig. 2-12: Scanning electron micrographs of a porous monolith plug inside a channel [10]

Porous silicon: Originally discovered by A. Uhlir in 1956 [66], porous silicon is an alternative morphological form of single-crystal silicon, and is obtained by anodic attack in concentrated hydrofluoric acid solutions [67]. This process results in nanopores approximately ~6-10nm in size and porosity ranging between 50-70% [68]. To date, porous silicon has found application in a variety of fields, including silicon-on-insulator technologies [67], mass spectrometry [69], as well as in biological platforms for enzyme immobilization [70] and optical biosensing of protein binding [71]. However, it is similarly limited as polymer monoliths in terms of feature patternability, and it has lower permeability compared to other porous architectures.

2.4 Carbon nanotubes and bio-medicine

This thesis features the use of porous carbon nanotube (CNT) forests for bioparticle separation. Carbon nanotubes (CNTs) have been widely explored for biomedical applications due to their unique electrical, thermal and surface properties [72]. Most of these applications make use of

solubilized, randomly-aligned, functionalized CNTs. Chemical functionalization of CNTs with biomolecular binding moieties have been well investigated. Multiple strategies are available in the literature for both covalent [73] and non-covalent [74, 75] linkage of biomolecules to CNT sidewalls. Single CNT fibers as well as CNT networks exhibit semiconducting behavior, and proximity of charged or polarized biomolecules can create gating effects on CNT field effect transistors (FETs). This technique has been successfully utilized in a number of microfluidic biosensor applications for specific bioparticle detection [76-78]. Another interesting property of solubilized, functionalized CNTs is their ability to be internalized by mammalian cells [79]. This has led to investigations on using CNTs as vehicles for drug delivery [80-82], and as targeting agents for thermal destruction of cancer cells [83]. The latter application takes advantage of yet another unique property of CNTs, in which they efficiently convert absorbed microwave radiation into heat energy [84].
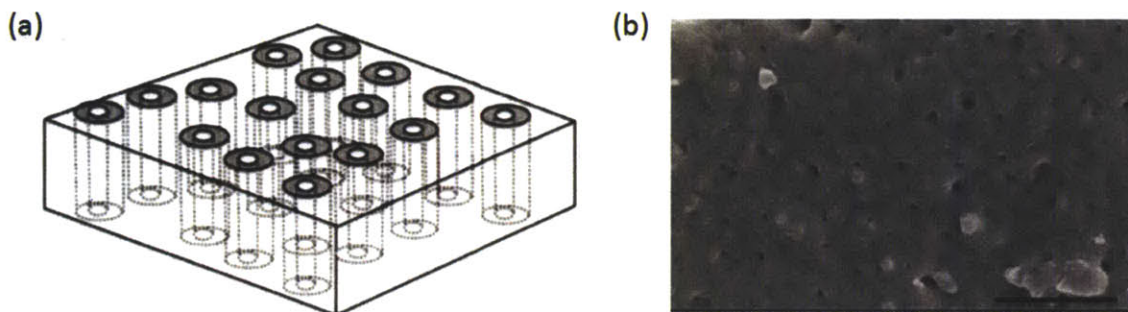
Fig. 2-13: Schematic and scanning electron micrograph of a CNT-polymer membrane with cylindrical pores comprised of the inner diameter of CNTs. Scale bar is 2.5μm. [11]

Despite this variety of applications, few groups have taken advantage of the physical properties of intact VACNT forests (e.g. high porosity, patternability, large aspect ratio) for bio-analytical applications, with the exception of several designs that make use of them as membrane filters for particle exclusion. For example Hinds incorporated aligned CNTs into a polymer film to form a porous membrane where molecular transport can take place through the hollow inner core of nanotubes (Fig. 2-13 and [11]), and Nednoor created a biomimetic membrane that mimics protein channels [85]. Both of these designs make use of pores comprised of the inside diameter of individual CNTs, which have very low porosity and molecular scale pore size. In contrast, the

work presented in this thesis utilizes the ultra-high porosity (99%), nanometer scale pores comprised of the gaps in between individual nanotubes of a vertically aligned forest.

2.5 Limitations of state-of-the-art methods in microfluidic bioseparation

Microfluidics has revolutionized the field of bioseparation to allow for assays using very low sample volume, with finer control of flow characteristics, and simpler approaches to automation and multiplexing than ever before. However, in the area of specific particle separation, it is hampered by some critical challenges: the low efficiency of particle-surface interactions in affinity based particle capture, the difficulty in accessing sub-micron particles, and design inflexibility between platforms for different particle types.

Particle-surface interactions: The major goal with device design in immunoaffinity capture is to achieve sufficient physical interactions between the bioparticles and the functional surfaces to promote binding. When the surfaces containing the affinity ligands are made of solid materials, these interactions are limited by flow stagnation effects at the fluid-solid interface. The detrimental effects of flow stagnation include both the lack of bulk fluid flow to the surface, and an increase in near-surface hydrodynamic resistance between a particle and the surface. These will be explored in detail in Chapter 5. Incorporation of geometrically controlled porous elements in affinity chromatography technologies to overcome the limitations of solid designs is a primary objective for this thesis.

Accessibility of sub-micron particles: The sizes of biological particles range over four orders of magnitude from tens of nanometers to tens of microns. There is a richly diverse range of particles in the sub-micron range both native (lipoproteins, exosomes, cell-free DNA) and pathological (viruses) that contain valuable biological information. However, the size realm of traditional 'micro'fluidics is ill equipped to handle particles in the 'nano' size range. Diffusion cannot be relied upon to bring particles to surfaces: a 50nm virus will take 5 minutes to diffuse across a distance of 50μm. Thus it is necessary to bring surfaces much closer to the particles to reduce diffusion distance and increase availability of interaction surface area. Traditional microelectriomechanical systems (MEMS) fabrication relies on photolithography, which is generally limited by the wavelength of light to feature sizes of around a micron. The use of nanoporous monoliths inside microfluidic channels or the fabrication of nanoscale channels

using nanoelectricomechanical systems (NEMS) techniques such as E-beam lithography will achieve the desired feature size. However, both methods suffer from very high flow resistance, which severely limits the throughput achievable. We show in Chapter 3 that the ultra-high porosity of our nanoporous VACNT forests results in very high fluid permeability, such that we can provide accessibility to nanometer size particles without significant loss of throughput.

Design inflexibility in particle isolation platforms: Due to the difficulties in creating particle-surface interactions even for a single particle type, microfluidic bioseparation devices are currently highly tailored in design. Platforms vary greatly depending on the size, concentration, and surface properties of the particular particle of interest, and no one technology is capable of multi-scale, multi-physics separation across different particle types. With the dual highly porous nanostructure and patternable microstructure properties of the VACNT microfluidic devices introduced in this thesis, we can begin to explore simultaneous isolation of multiple particle types in a single device platform across both micro and nano size ranges. Examples using model particles spanning four orders of magnitude in size are presented in Chapter 4. This unprecedented flexibility in device design will pave the way for new areas of application in fluid and particle manipulation at the micro and nano-scales.

Chapter 3

Fabrication and characterization of nanoporous VACNT microfluidic devices

This work represents one of the first efforts to combine VACNT forests into microfluidics. Section 3.1 illustrates the fabrication method used to create vertically aligned carbon nanotube forests. Section 3.2 describes two methods that we developed for integrating CNT forests inside of microfluidic channels, one of which allows for top sealing of the forest with the channel, and the other allows for both top and side sealing. The behavior of the VACNT elements in wetting and flow is characterized in 3.3, and its permeability to liquid flow measured in 3.4. When permeability measurements were conducted, it was discovered that the material permeability of the VACNT forest is significantly higher than those known for other nanoporous materials, and is in fact comparable to that of many microporous materials. Section 3.5 gives the analytical explanation as to why this is. In section 3.6, we show that we can make adjustments to the permeability by varying growth parameters of the VACNT forest. Finally, different known functionalization strategies for CNTs were investigated in section 3.6 to identify one most suited to the VACNT-microfluidic system, and this was compared to standard PDMS functionalization in section 3.8.

3.1 Fabrication of patterened VACNT forests

The method used for fabrication of patterned VACNT forests has been previously described by Garcia et. al [86]. CNT growth is performed in a 4" ID quartz tube chemical vapor deposition (CVD) furnace (G. Finkenbeiner, Inc.) at atmospheric pressure using reactant gases of C_2H_4, H_2 and He (Airgas, 400/1040/1900 sccm). Catalyst annealing is carried out in a reducing He/H_2 environment at 650°C, leading to the formation of catalyst nanoparticles about 10 nm in diameter. C_2H_4 is then introduced into the furnace to initiate CNT growth, occurring at a rate of approximately 100 μm/min until the flow of C_2H_4 is terminated. The nanotubes grown using this

method are multi-walled (2-3 concentric walls), with a diameter of around 8nm. Figure 3-2 shows the transmission electron micrograph (TEM) of a single multi-walled CNT.

(a)

(b) **Ebeam deposition of Al$_2$O$_3$ (10nm) and Fe (1nm)**

Si substrate

Fe

Al$_2$O$_3$

Si substrate

(c) **Annealing (650 C, He/H$_2$) and catalyst nanoparticle formation**

(d) **Nucleation and vertical growth**

$(D_{CNT} \approx D_{catalyst\ nanoparticle})$

Si substrate

Si substrate

Growth direction
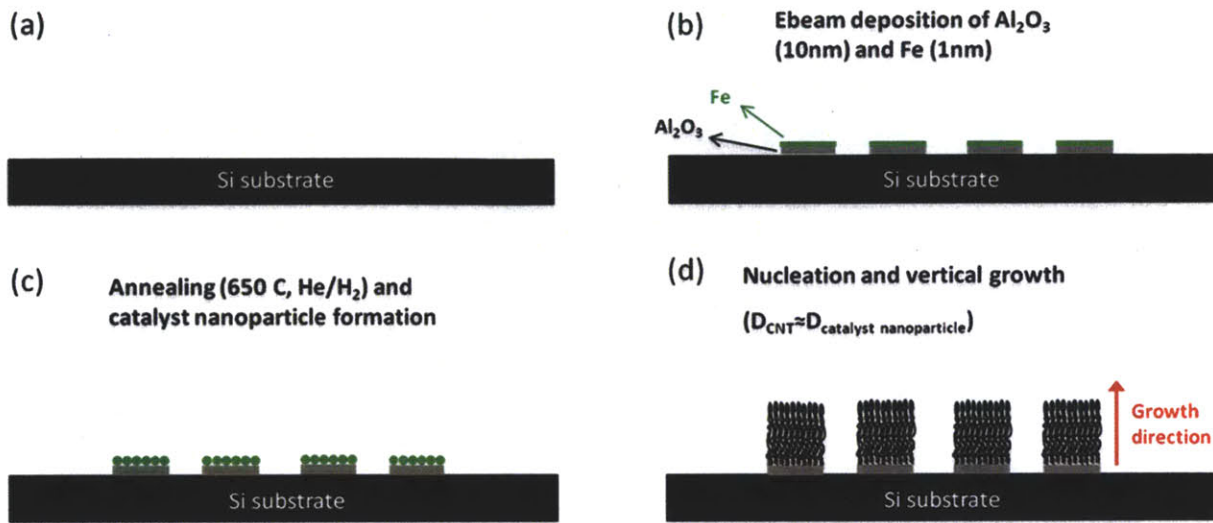
Fig. 3-1: Schematic for patterning and growth of VACNT elements

5nm
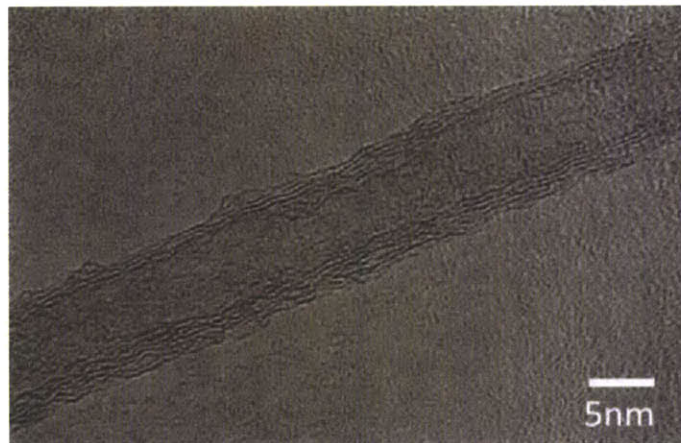
Fig. 3-2: Transmission electron microscopy (TEM) showing the multi-walled structure (3-4 concentric walls) for the vertically aligned carbon nanotubes (VACNTs) in this work. Image taken from [87]

The CNTs are spaced by approximately 80nm, thus yielding a 1% volume fraction of CNTs [88]. Examples of patterned cylindrical posts are shown in the electron micrograph (SEM) in Figure 3-3(a) and 3-3(b). The vertical-alignment of the nanotubes in the forest is noticeable in the high resolution SEM depicting the forest nanostructure in Figure 3-3(c). This fabrication method enables the creation of very high aspect ratio structures more efficiently than some state-

of-the-art MEMS processes. For example, whereas deep reactive ion etching (DRIE) can create elements up to hundreds of microns deep at a rate of approximately 2-4μm/min, this technique yields VACNT elements up to several millimeters in height at a rate of ~100μm/min.
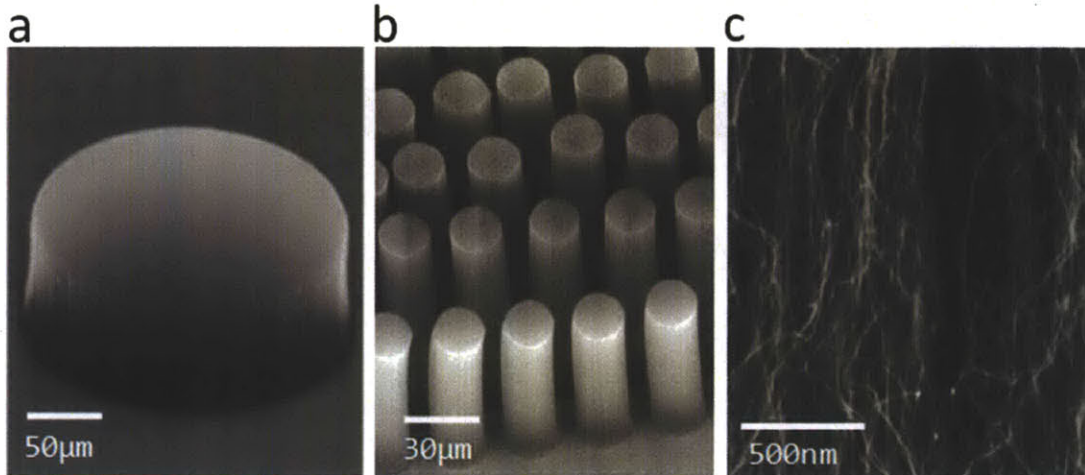
Fig. 3-3: Scanning electron micrographs (SEMs) of patterned VACNT elements. (a) A 200μm diameter single post. (b) An array of 20μm diameter posts. (3) Nanostructure of a VACNT forest

3.2 Integration of VACNT elements into microfluidic devices

The challenge with integrating VACNT elements into microfluidic channels is to create effective sealing so that there is no leakage of flow over the top of the elements (the bottom of the forest is already sealed to the silicon substrate). Section 3.2.1 explains the methodology we developed to achieve this. In the majority of our applications, it is desirable for flow to go around the VACNT features on either side. However, for certain applications, and for permeability measurements, we need to create nanoporous filters that are well sealed on all sides. A second strategy to device integration that achieves this is shown in section 3.2.2.

3.2.1 Nanoporous VACNT devices with patterned PDMS channels

The integration strategy depicted in Figure 3-4 is derived from standard polydimethylsiloxane (PDMS) channel fabrication and bonding techniques. Microfluidic channels were generated using soft lithography [89]. SU-8 photoresist (Microchem) was patterned on a silicon wafer by photolithography to form a negative mold. A 10:1 mixture of PDMS pre-polymer and curing agent (Sylgard 184, Dow Corning) was poured onto the mold and baked at 75°C until cured. The PDMS channels were then treated with oxygen plasma for 30 seconds, after which they are

36

aligned and placed on top of the silicon wafers containing the CNT structure. A further 10 minute heat treatment on a 70°C hotplate results in irreversible bonding. Channels are made several microns shorter than the height of the CNT structures so that the ceiling of the channel slightly compresses the top of the CNTs to produce a compression-fit seal.

(a) Pattern nanoporous features from VACNT forests

(b) O$_2$ Plasma treatment

(c) Bonding of PDMS channel (5-10μm shorter than the VACNTs) to Si substrate
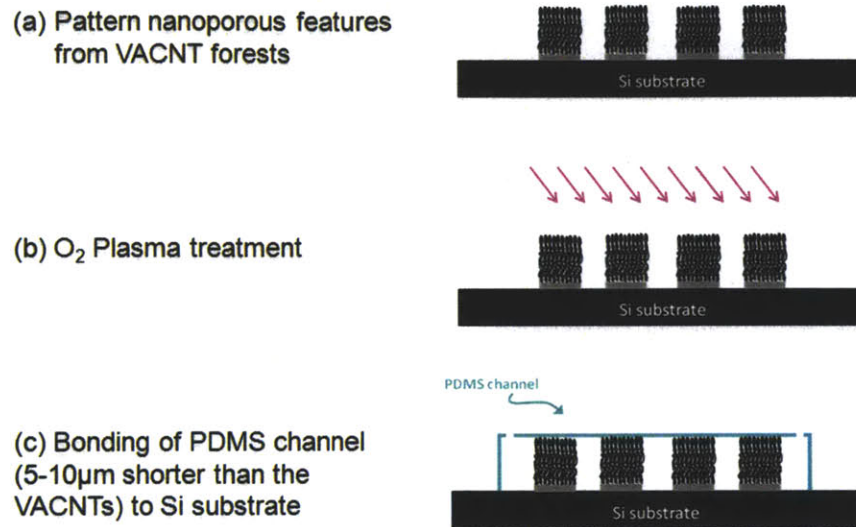
Fig. 3-4: Strategy for device integration with top sealing.

3.2.2 Nanoporous VACNT devices with polymer-filled CNT channels

The integration strategy depicted in Figure 3-5 ensures top and side sealing of the VACNT element against the channel walls. It achieves this by constructing both the features and the channel walls from patterned VACNT forests such that there is no gap between them. The permeability of the channel walls are then made significantly higher by selectively filling them with V3D3, a silicone based polymer very similar to PDMS. Infiltration is performed using chemical vapor deposition (CVD), at the Gleason group at MIT [90]. A physical shadow mask, laser cut from sheet acrylic is used to protect the VACNT features inside the channel from the infiltration process. Characterization results for the infiltration process are shown in figure 3-6. We see from the energy dispersive X-ray spectroscopy (EDS) analysis that the V3D3 polymer, which contains silicon and oxygen, has reached all the way into the bottom of the 80μm tall forest down to the silicon substrate. An advantage of this technique is that the channel walls are intrinsically the same height as the VACNT features, so no height matching is required.

37

| (a) | (b) |

Pattern and grow both channel and features out of CNT forests

CVD V3D3 polymer using a mask to selectively infiltrate channel walls with polymer (Gleason lab)

| (c) | (d) |

Spin coat a 5um layer of uncured PDMS onto a flat piece of cured PDMS

Cap channel with PDMS piece and bake to cure
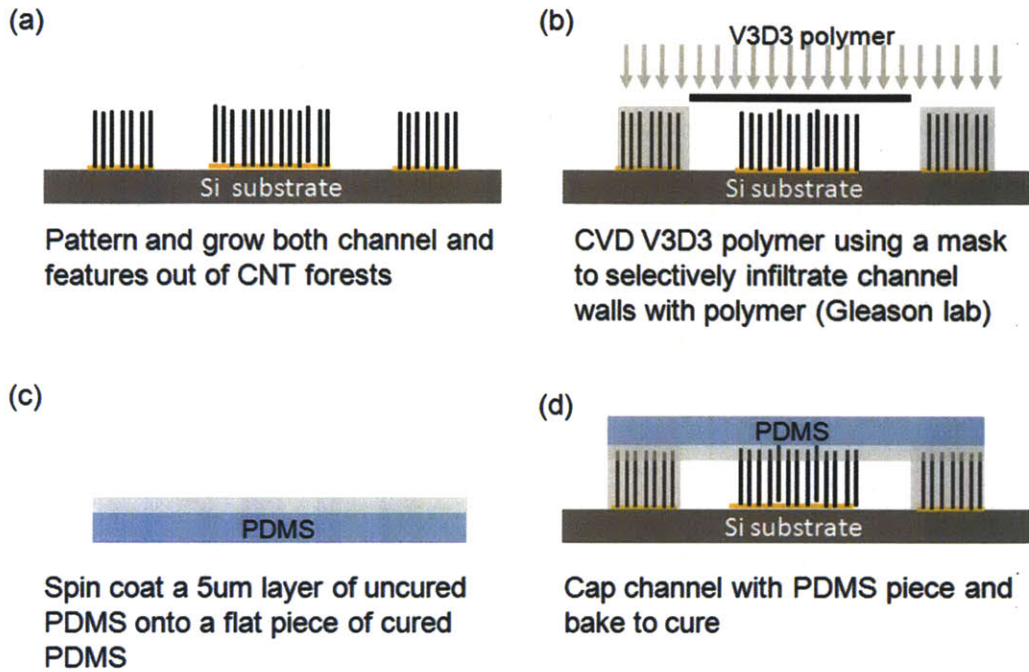
Fig. 3-5: Device integration using polymer infiltrated CNT as channel walls and a flat PDMS channel cap.
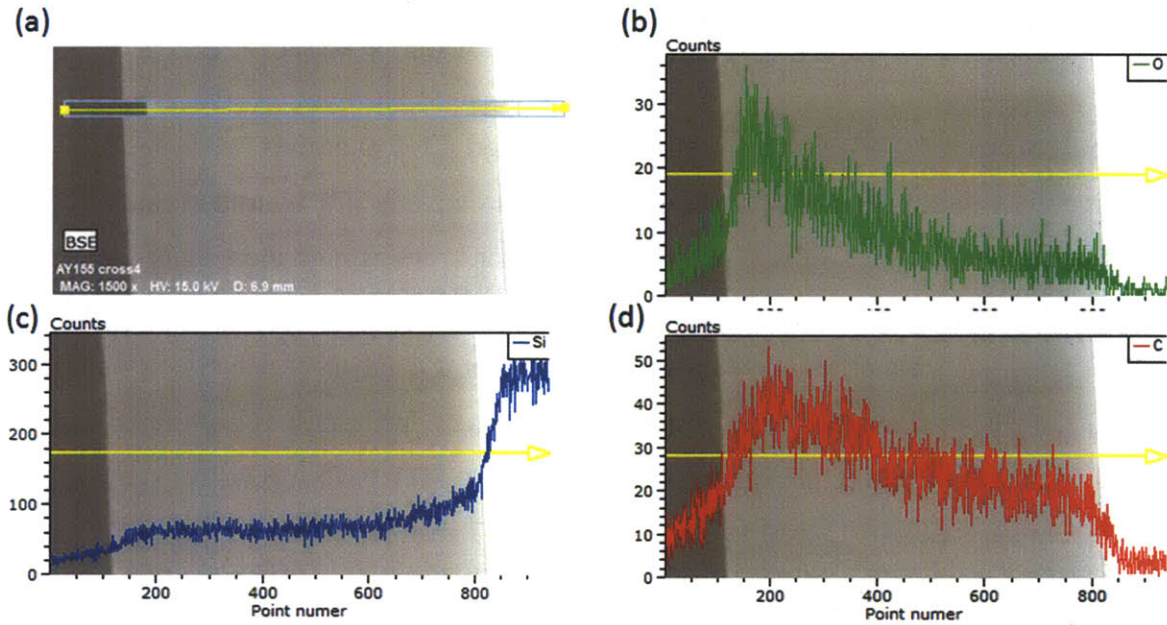
Fig. 3-6: Energy Dispersive X-ray Spectroscopy (EDS) results for polymer infiltration of a 80μm high VACNT forest. Every 100 points on the x-axis corresponds to 10μm, and counts on the y-axis corresponds to elemental concentration. Images taken by Dr. Ayse Asatekin from the Gleason lab. (a) SEM of the forest cross section. Substrate is on the right. (b) Oxygen variation across the forest. (c) Silicon variation. (d) Carbon variation

After infiltration, the device is completed by the attachment of a PDMS ceiling. First, a flat piece of cured PDMS 2-3mm thick is cut to the same size as the channel footprint, with the inlet and outlet punched out. Then uncured PDMS prepolymer and crosslinker are mixed at a 10:1 ratio and degassed inside a vacuum chamber. A drop of the mixture is placed on top of the cured PDMS piece, and spun at 3000rpm for 180 seconds, creating a 5μm thick 'glue' layer. The PDMS and glue are then placed on a 70°C hotplate for 6-7 minutes to increase the viscosity of the glue layer. Finally, the piece is placed onto the VACNT channel with the glue side down to complete the device, and cured inside a 70°C oven for another 4 hours to harden. This method attaches a flat ceiling to the open channel that had been formed by the polymer-filled CNT forests, whereas in the method described in section 3.2.1, the channel was formed by molded PDMS.

3.3 Characterization of VACNT devices in wetting and flow
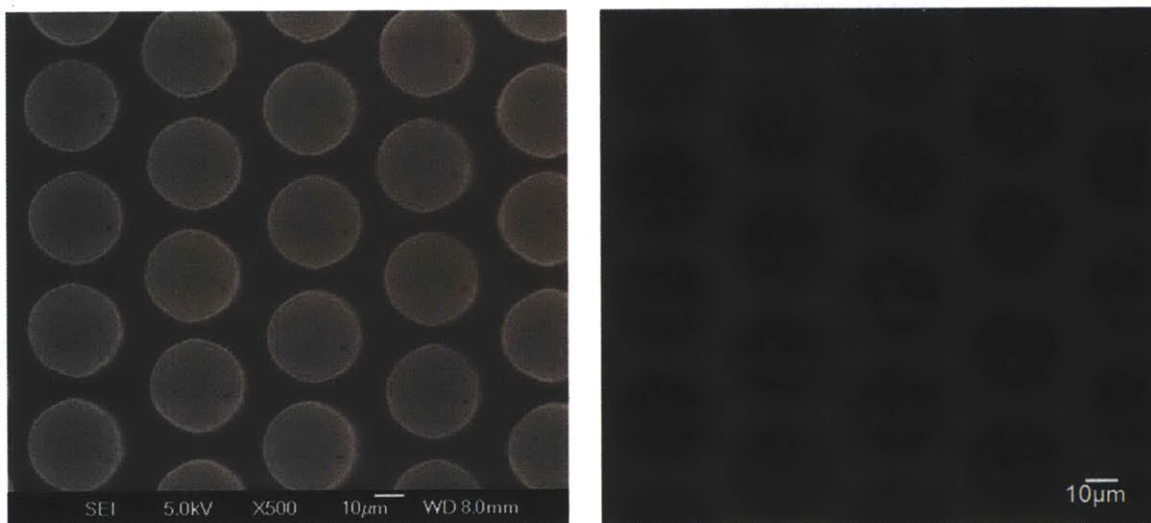
Fig. 3-7: Comparison between SEM of as grown VACNT post array (left) and optical micrograph of the same array post wetting and flow (right).

The ability for the VACNT elements to maintain their geometry through wetting and liquid flow is essential to their application in microfluidics. There were several potential challenges with this. First, as-grown CNTs are highly hydrophobic [91]. In order to achieve wetting inside the forest, we make use of Tween-20, an amphiphilic detergent that can form a monolayer coating on CNTs to make them hydrophilic. It is also a highly effective deterrent to non-specific binding

39

by biomolecules [74]. Second, previous attempts at wetting VACNT forests not confined inside microfluidic channels have reported catastrophic collapse of the forest morphology [92, 93]. This is largely due to the strong capillary forces that occur during partial wetting. We observed that for our confined forests where the top and bottom ends of the CNTs are sealed by the channel ceiling and the substrate, wetting by liquid flow perpendicular to the CNT axis results in preservation of the forest morphology (see Fig. 3-7). A third concern is that the shear stress created by fluid flow may physically dislodge the VACNT features from the substrate, or distort its morphology. We found that although higher flow rates >500μL/min does result in detachment of the patterned VACNT features, morphology is preserved at 200uL/min or below, which is the operating regime of the majority of microfluidic applications.
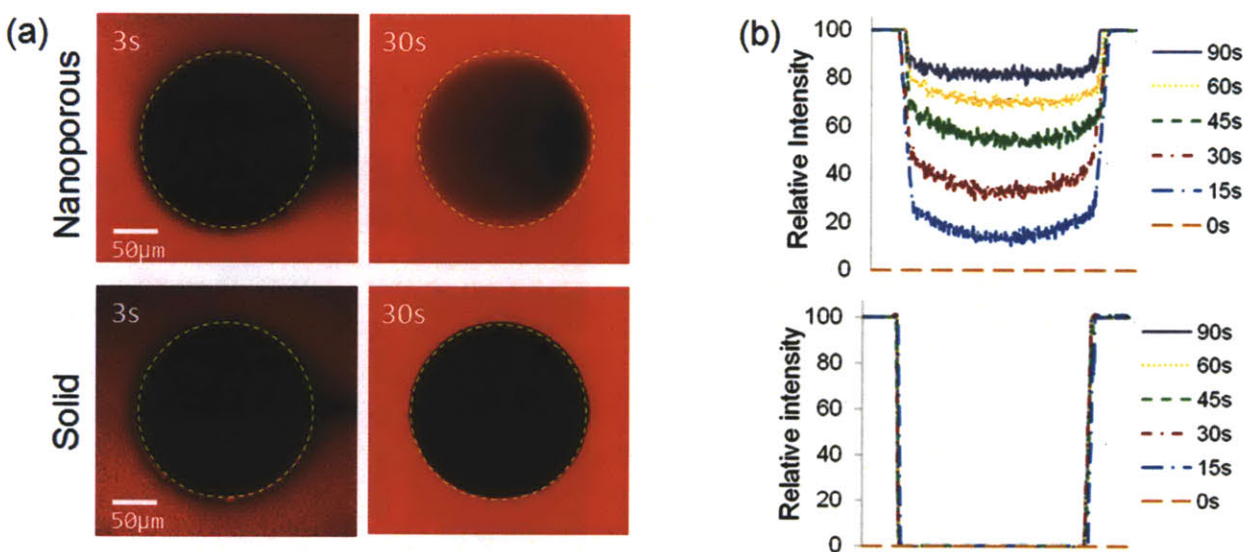
Fig. 3-8: Nanoporous micropatterned elements are permeable to fluid and small molecules. (a) Confocal micrographs of 200 μm diameter nanoporous and solid posts as a fluorescent dye solution flows through the micro-channel. Images are taken at a z-plane 5μm below the channel ceiling. (b) Relative intensity plots of dye infiltration with time inside nanoporous and solid posts. Intensity values evaluated along vertical center line across each post.

To study the penetration of fluid and particles inside the nanoporous VACNT elements, we conducted flow experiments using both small molecule dyes and nanoparticles. Figure 3-8(a) demonstrates the penetration of water and small molecule dyes (rhodamine, MW 479 Da) inside a nanoporous CNT post over 90 seconds; by comparison, and as expected, there is no dye penetration inside the solid PDMS post. Fluorescence intensity analysis of each type of post as

the dye penetrates over time is quantified in Figure 3-8(b). The devices used consist of single posts 200μm in diameter and 100μm in height, sealed inside a 3mm x 20mm x 100μm PDMS channel. 0.5% Tween-20 in DI water was used to treat the devices after fabrication to make surfaces hydrophilic, and to block non-specific binding. Rhodamine B (Sigma Aldrich) solution in DI water with 0.1% Tween-20 was injected into the channel using a syringe pump (Harvard Apparatus) set to 10uL/min flow rate. Imaging was performed using a confocal microscope (Zeiss), and intensity plots are made using ImageJ software.

To characterize flow of nanoparticles inside the nanoporous structures, a dilute suspension of fluorescent quantum dots (QDs) 10-20 nm in size was injected, and their flow paths inside and outside of a 200 μm diameter nanoporous post was imaged via confocal microscopy. Figure 3-9 follows the path of a single QD as it travels through a nanoporous post (shown with yellow arrows) and compares it with another QD (indicated by dashed red arrows) that passes around the outside of the same post. Due to increased fluid resistance inside the nanoporous structure, the QDs are observed to travel inside the CNT post at a significantly reduced velocity, only 8% of its counterpart traveling outside the post. The devices and flow conditions used for the particle experiments are the same as for the molecular dye experiments. These studies clearly demonstrate the ability of aligned CNT structures to allow pressure-driven flow of both molecular and particulate species inside the nanoporous elements.
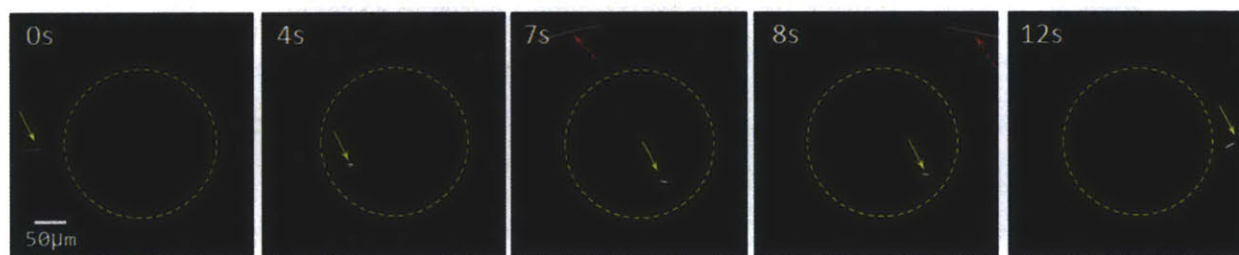
Fig. 3-9: Fluorescent quantum dots (10-20 nm) passing through a 200 μm diameter nanoporous post (outlined via dotted lines) having 80 nm CNT spacing. Yellow arrows follow the passage of one quantum dot through the post, red arrows follow another passing around the outside of the post. Images are taken at a z-plane 5μm below the channel ceiling.

3.4 Permeability measurement of VACNT elements

The fluid accessibility of a porous material is determined by its permeability, which is defined by Darcy's Law, the constitutive equation of porous media flow [94]:

$$Q = \frac{-\kappa A \Delta P}{\mu L} \qquad (3.1)$$

where Q [m^{3}s^{-1}] is the volumetric flow rate, ΔP [Pa] is the pressure drop along the channel, A [m^2] and L [m] are the cross-sectional area and length of the porous channel, μ [kg m^{-1}s^{-1}] is the dynamic viscosity of the fluid, and κ [m^2] is the permeability of the porous media. Highly permeable materials are attractive for microfluidic applications as they minimize back pressure (ΔP) for a specific flow rate, requiring less powerful injection systems and allowing for lower specification (and lower cost) interconnects.
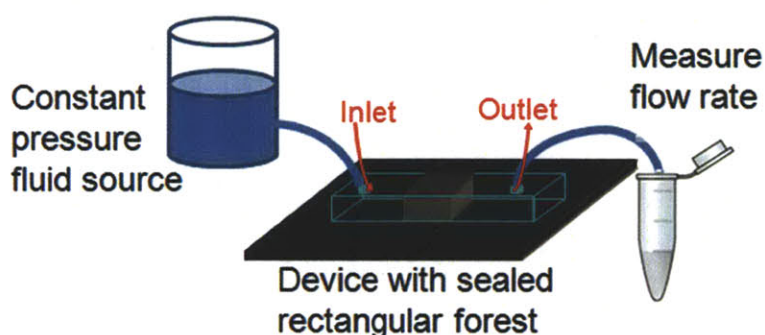
Fig. 3-10: Schematic for empirical measurement of VACNT forest permeability

Figure 3-10 illustrates our method for experimental determination of the permeability of the VACNT forests. The devices used for these experiments consist of rectangular forests surrounded by polymer infiltrated CNT channel walls, as described in 3.2.2. The devices are well sealed on all sides such that there is no low resistance leakage path around the forest. The rectangular VACNT elements (2mm wide, 200μm deep, 100μm tall) were first wetted using 0.5% Tween in DI water. A solution of 0.1% Tween in DI water was then injected for 2 minutes at a fixed inlet pressure of 2psi, and all the outlet flow collected into an Eppendorf tube. The volume of the collected outflow was measured and used to compute the flow rate, which was then input in (3.1) to extract the permeability value κ. Repeats are performed over 5 different devices to assess the variation across devices. Using this procedure, the fluidic permeability of the VACNT structures was quantified as $5.4*10^{-14} \pm 8.3*10^{-15}$ m^2. We compared this value with the permeability measured using similar devices where the channel walls are constructed of patterned VACNTs, but did not undergo polymer infiltration. Figure 3-11 shows that without infiltration, the permeability values obtained are much higher with a very large standard

deviation. This suggests significant fluid leakage through the channel walls to give unreliable measurements. Thus we conclude that polymer infiltration is required to ensure that the fluid only passes through the desired nanoporous elements, and not through the VACNT-based channel walls.
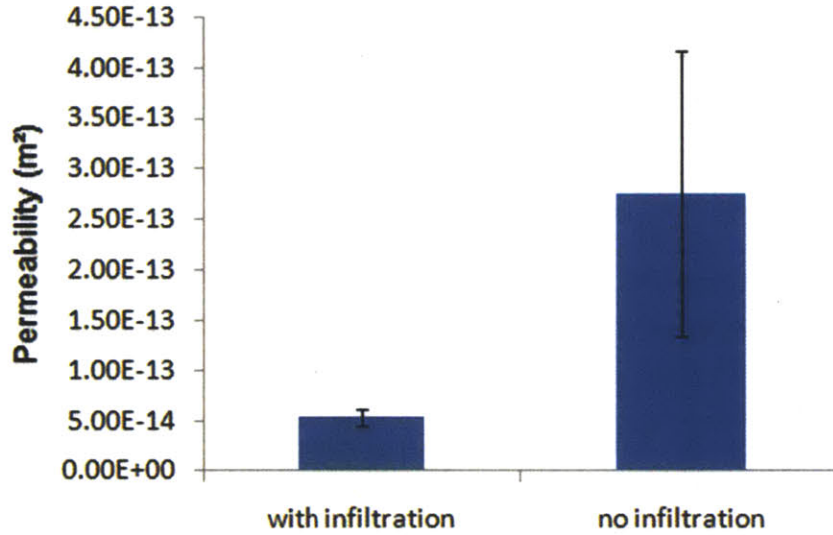
Fig. 3-11: Comparison between experimental measurements for permeability of of a VACNT rectangular barrier in devices with and without polymer infiltration in the VACNT channel walls

Table 3.1: Examples of porous technologies with their permeability and porosity values

Material	Source	Feature size D	Pore size p	Porosity φ (%)	Permeability κ [m^2]
Polymer capillary columns	Urban and Jandera [95]	4.3µm	4µm	57	8.9E-14
Polymeric membranes	Neeves and Diamond [96]	4µm	1µm	40	3.60E-15
Polymer monoliths	Du et al. [97]	3.5 µm	1-6µm	71	6E-14
Silica monoliths	Fletcher et al. [98]	1.25µm	4.16µm	70.1	7.65E-14
Porous silicon	Lysenko et al. [68]	16nm	7nm	60	6.4E-18
VACNT	This work	8nm	80nm	99	5E-14

In table 3.1, we compare the permeability of our VACNT forest with other micro and nanoporous materials from literature. Interestingly, this permeability value is comparable to or higher than that of other porous technologies with much larger pore sizes. This result is somewhat counterintuitive, as one would expect materials with larger pores to be more accessible to fluids. The large difference in permeability between VACNT elements and porous silicon is also not obvious, as these elements have similar pore dimensions. The high permeability of our VACNT forests can however be explained by classical analyses of the effect of porosity on permeability, as described in section 3.5 below.

3.5 Analytical discussion on the relationship between porosity and permeability of porous materials[†]

Macro- and meso-scale porous materials such as granites, millstones and fine powders were given particular attention during the second half of the last century [99], as they were starting to be considered for applications such as water distillation and temperature control in highly exothermic reactions. Between others, Sabri Ergun (1952) studied the flowthrough porous materials by modeling their internal structures, including regular beds of aligned pillars (equivalent diameter D; height $\gg$ D) that lay perpendicular to the flow direction and that are spaced apart by a distance S (see inset of Figure 3-18(a)). In his work [100], Ergun derived the following semi-empirical expression that relates feature size (D [m]), structural and fluid permeability (κ [m^2]):

$$\kappa_{Ergun} = \frac{1}{c} \frac{\phi^3}{(1-\phi)^2} D^2 \qquad (3.2)$$

where c is a constant dependent on both the pillars' geometry (e.g., squares vs. cylinders) and the feature's size scale (e.g., macroscopic vs. microscopic). In Ergun's meso-scale experiments (average pillar diameter between 0.5-0.8mm), the constant c was quantified as 150. Note that for the case of cylindrical pillars the porosity (ϕ) can be expressed as [99]:

$$\phi = 1 - \frac{\pi}{4} \frac{D^2}{(S+D)^2} \qquad (3.3)$$

44

where S is the distance between each pillar in the structure. Equation (3.2) allows one to distinguish between the effects of size and structural porosity on the permeability of porous materials. On one hand, given a certain porosity level ϕ, fluid permeability is proportional to the second power of the feature size (i.e., $\kappa \sim D^2$). Designs with larger features (e.g., unconsolidated rocks) are therefore generally more fluid accessible than smaller elements (e.g., sands), a result that matches intuition. On the other hand, less intuitive is the effect of structural porosity, which is plotted in Figure 3-12(a) for a porous material with $D = 1$m. Noticeably, the functional dependence of permeability on porosity changes significantly at different porosity levels: while permeability is linearly proportional to structural porosity at moderate porosity levels ($0.3 \sim< \phi \sim< 0.8$), its dependence on porosity is highly non-linear at both very small ($0 < \phi < 0.3$) and very large ($0.8 < \phi < 1$) porosities. The effect of porosity on permeability at different porosity regimes can be summarized as:

$$\kappa \simeq \begin{cases} \phi^3, & 0 < \phi < 0.3 \\ \phi, & 0.3 \leq \phi \leq 0.8 \\ \frac{1}{(1-\phi)^2}, & 0.8 < \phi < 1 \end{cases} \qquad (3.4)$$

The presence of two highly non-linear regions in the porosity-permeability relation of porous materials is extremely relevant from a designer's perspective, as it suggests decreases/increases in the permeability of porous devices by designing in the very small/ very large porosity regions. This possibility becomes apparent is Figure 3-12(a), where dramatic ($>10^3$ m^2) decreases/ increases in permeability can be noticed at both ends of the porosity spectrum. The possibility to enhance device permeability through porosity control is particularly attractive for miniaturized platforms where feature size is limited compared to larger technologies. The results above can be used to rationalize the findings of Section 3.4, where we showed that nanoscale VACNT elements yield permeability comparable to, or even higher than, that of larger micro-scale porous materials (see Table 3.1). Our VACNT forests are ultra-porous (99% porosity), and therefore fall within the large non-linear permeability-porosity region (i.e., $0.8 < \phi < 1$) of Equation (3.4) and Figure 3-12(a). As a consequence, VACNT elements yield permeability comparable to that of much larger macro-/micro-scale porous materials yet at a significantly smaller (i.e., nano) scale, thus favoring further miniaturization of MEMS devices.

(a)

$$\kappa_{Ergun} = D^2\phi^3/[150(1-\phi)^2]|_{D=1\ m^2}$$

$\kappa \approx \phi^3$

0~< κ ~< 0.3:
Large permeability decrease

$\kappa \approx \phi$

0.3~< κ ~< 0.8:
Linear dependence of permeability on porosity

$\kappa \approx (1-\phi)^{-2}$

0.8~< κ ~< 1:
Large permeability increase

(b)

The ultra-high porosity (99%) of our nanoporous VACNT features yields permeability comparable to that of larger micro-scale platforms

D↑

Polymer capillay columns
△ Urban and Jandera, 2008
Polymer monoliths
✳ Du et al., 2007
Silica monoliths
★ Fletcher et al., 2010
Porous silicon
□ Lysenko et al., 2004
VACNT forests
◇ Fachin et al., 2011

Fig. 3-12: Analytical and experimental results on the effect of feature size and porosity on the permeability of porous microfluidic materials. (a) The effect of porosity on permeability via Ergun's relationship [100]. (b) Ergun's curves for several state-of-the-art micro- and nanoporous materials used in microfluidics.

46

To further clarify the effect of porosity on the permeability of porous structures, in Figure 3-12(b) we plot Ergun's formula (Equation (3.2)) for each microfluidic technology of Table 3.1. Despite that the nature of these porous technologies deviates from Ergun's original structural model (i.e., regular beds of aligned pillars), good agreement between theoretical and experimental results is observed. Most importantly, Figure 3-12(b) allows one to visualize the effect of large porosity (99% porosity) on the permeability of VACNT structures. The nanoporous VACNT technology takes advantage of the large non-linear permeability increase at high porosity levels, while all other porous platforms fall within the linear permeability-porosity region. As a result, the nanoporous VACNT elements yield permeability significantly higher than that of similar nanoscale technologies, thus being as accessible to fluids as larger micro-/macro-scale materials. This is extremely important for microfluidics because higher permeability results in lower flow resistance inside the porous regions, and higher flow rates without the need for high pressure pumps. Thus the VACNT elements can provide nanoscale filtration and diffusion length scales for nano-bioparticle separation, without the low throughput that limits many other nanofluidic technologies.

3.6 Adjustment of material permeability of VACNT elements through manipulation of growth parameters

Section 3.5 showed that the permeability of porous materials is directly dependent on their porosity, and that very high porosity levels (>80%) are associated with large non-linear increases in permeability as per Ergun's formula (Equation (3.2)). Here, tailoring of the permeability of VACNT forests through manipulation of both material (e.g., catalyst thickness) and CNT growth process parameters (e.g., temperature ramp-up time, growth temperature) are investigated. In particular, equation (3.3) defined the porosity of porous materials as a function of both feature size D and the average distance S between each feature in the material (see inset of Figure 3-12(a)). Material and CNT growth process parameters could therefore be controlled to manipulate both D and S, thus also modifying the structure's porosity and permeability. The growth parameter adjustment was performed by Dr. Fabio Fachin.

In this work, two different approaches were taken to forest manipulation, both of which aimed at increasing intra-CNT spacing (i.e., the average distance between single nanotubes in the

forest). The first approach is based on fine tuning the growth process conditions to increase the size and spacing between catalyst islands prior to CNT growth initiation. This method was presented by Hart [101] and others, e.g. [102], and it consists of varying the H_2 pre-treatment time (PTT) to modify the Fe catalyst nanoparticle size. In this work, the H_2 pre-treatment time was increased by 8 minutes compared to baseline growth, yielding the VACNT forest morphology shown in the center column of Figure 3-13. Compared to baseline forests, the +8PTT structures yield larger intra-CNT spacing (~93nm vs. 80nm for baseline structures) and a 70% increase in fluid permeability ($\kappa = 9.3 * 10^{-14}\,m^2$ vs. $\kappa = 5.4 * 10^{-14}\,m^2$), thus demonstrating the possibility to tailor forest permeability using this method.
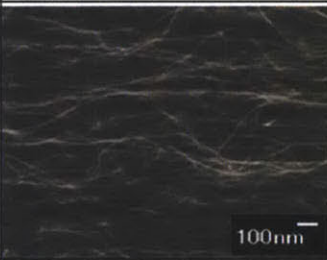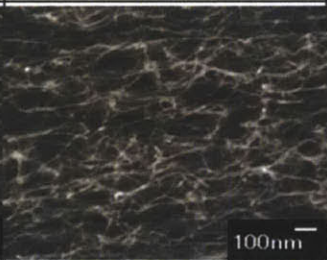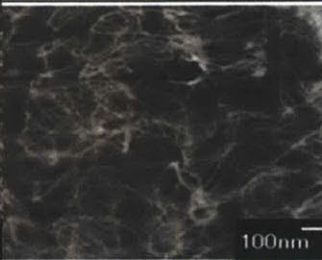
Sample type	Baseline	+8min PTT	Thicker catalyst (3nm)
High-res SEM			
Permeability (m^2)	$5.4*10^{-14}\,(\pm8*10^{-15})$	$9.3*10^{-14}\,(\pm1.9*10^{-14})$	$1.1*10^{-13}\,(\pm1.8*10^{-14})$

Fig. 3-13: The permeability of VACNT forests can be manipulated by controlling both growth process (pre-treatment time - PTT) and material parameters

A second approach to permeability control was undertaken that uses control of catalyst thickness to yield forests with larger intra-CNT spacing. Between others, this approach to forest morphology control was presented by Wei et al. [103], who demonstrated a strong correlation between catalyst film thickness and the average CNT diameter and spacing. In this work, the catalyst thickness was doubled (from 1nm to 2nm) resulting in forests shown in the right column of Figure 3-13. These structures are characterized by an average of 98nm intra-CNT spacing, and yield a 103% increase in forest permeability ($\kappa = 1.1*10^{-13}m^2$) compared to baseline devices. These results are a demonstration of manipulation of forest permeability through control of material and growth process parameters. However, further optimization of these approaches is

required to improve the CNT vertical-alignment, and therefore minimize the tortuosity [99] by focusing on forest morphology changes in addition to porosity.

3.7 Functionalization of VACNT microdevices for specific biorecognition

Bio-functionalization of carbon nanotubes has been widely investigated due to their applications in cellular targeting and biosensing (see section 2.4). Many different methods have been reported for both covalent and non-covalent addition of functional groups to the walls and ends of CNTs [73, 104, 105]. Our goal was to select an effective functionalization protocol from existing literature that is compatible with on-chip processing, that does not disturb the vertically aligned morphology of our CNT forests, and that yields good specific biomolecule binding while blocking non-specific binding.
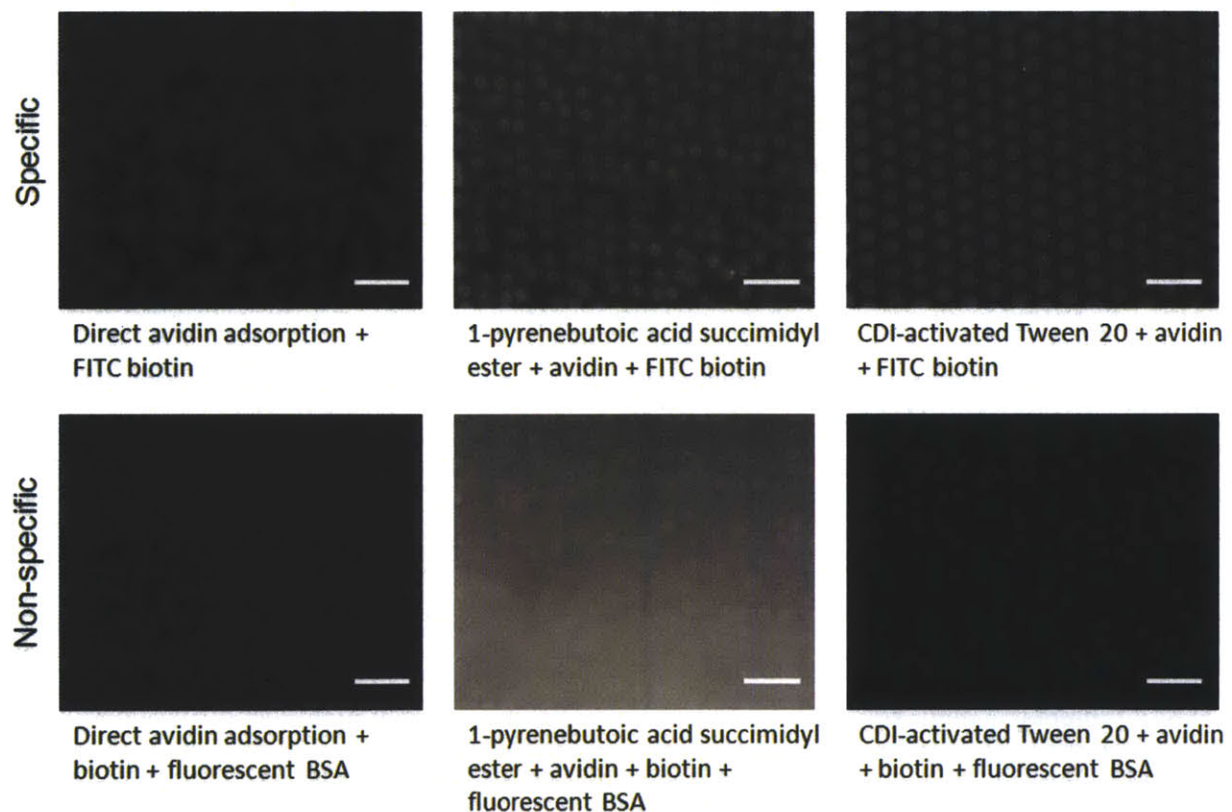
Fig. 3-14: Specific and non-specific binding results for three different non-covalent surface functionalization strategies. In each case, specific binding is qualitatively measured by fluorescence intensity of FITC biotin molecules, which selectively attaches to avidin molecules functionalized onto the CNT surface. Non-specific binding is measured by fluorescent BSA molecules, which should not specifically attach to the aviddin-functionalized surface. Devices are a mixture of 10μm, 20μm and 30μm post arrays. Scale bar is 100μm.

For any covalent attachment of biomolecules to CNTs, functional groups must first be formed on the CNT surface. The carboxylic acid group is the most popular choice because it can undergo a variety of reactions and is easily formed on CNTs via oxidizing treatment. However, the nature of these treatments, most of which involve ultrasonicating a dispersion of CNTs in acid mixtures [106], is not feasible for our patterned VACNTs integrated with microfluidics. In addition, the majority of the carboxyl groups created using these techniques are at the ends of the nanotubes, whereas we require functionalization of the CNT sidewalls. Because of these disadvantages of covalent functionalization strategies, we decided to focus on non-covalent methods, which involve much less harsh processing environments, preserves the geometry of aligned CNTs, and results in more sidewall binding sites [104].

Three different non-covalent functionalization strategies were identified as satisfying the requirements for microfluidics-compatible processing steps and sidewall binding sites. First, it is well known that proteins strongly and individually adsorb to the external walls of CNTs through hydrophobic interactions [107]. These nanotube-protein conjugates have been characterized at the molecular level by atomic force microscopy [108, 109]. The second strategy uses a bifunctional molecule, 1-pyrenebutanoic acid succinimidyl ester, as a linker. The pyrenyl group of the linker, being highly aromatic in nature, reacts strongly with the sidewalls of the CNTs by π-π stacking. The anchored molecules of the linker on SWNTs are highly stable against desorption in aqueous solutions. At the same time, the succinimidyl ester groups of the linker are highly reactive to nucleophilic substitution by primary and secondary amines that exist in abundance on the surface of most proteins. Thus protein immobilization on CNTs involves the nucleophilic substitution of N-hydroxysuccinimide by an amine group on the protein, resulting in the formation of an amide bond [75, 110]. The third functionalization strategy also uses a linker molecule that non-covalently binds to the CNT sidewalls but covalently attaches to the binding moiety of interest. The linker in this case is Tween-20, an amphiphilic molecule known to form a monolayer on CNT sidewalls and is highly effective in blocking non-specific binding. R.J. Chen et. al. developed an approach using 1,1-Carbonyldiimidazole (CDI) to activate the hydroxyl termini of Tween toward nucleophilic addition [74].

Using avidin functionalization and fluorescent biotin capture as the model protein-ligand system, and fluorescent bovine serum albumin (BSA) as the model non-specific binding protein,

50

we tested all three methods using fluorescence levels as readout. Figure 3-14 and Table 3.2 compares the test results. It was found that the CDI-activated Tween resulted in the highest levels of avidin binding and lowest levels of binding to fluorescent BSA post functionalization. The latter result is important in order to minimize non-specific binding in our capture systems. Thus CDI-activiated Tween was selected as the functionalization modality for antibody attachment to CNTs. The complete antibody functionalization process involves: addition of excess 1,1-carbonyldiimidazole to Tween-20 in dried DMSO; react under room temperature for 1 hour; precipitate using ethyl ether and dry under vacuum; inject 1% of the activated Tween in deionized water into the device; incubate for 1 hour at room temperature; rinse with water; incubate with NeutrAvidin in phosphate buffered saline (PBS) for 30 minutes; rinse with PBS; incubate with biotinylated antibody for 30 minutes. This process is adoped for all the functionalized CNT studies subsequently presented in this work.

Table 3.2: Summary of protocol, and specific and non-specific binding results for three different non-covalent CNT sidewall functionalization strategies.

Method	Steps	Specific binding	Non-specific binding
Direct Avidin adsorption	- Directly incubate avidin in PBS to as grown CNT devices	Low	Low
1-pyrenebutoic acid succimidyl ester	- Incubate as-grown CNTs with 5mM 1-pyrenebutanoic acid succimidyl ester in DMF - Incubate with avidin in PBS - Block with ethanolamine	High	High
CDI-activated Tween	- React CDI with Tween 20 in DMSO, precipitate with ether, wash and dry - Incubate as-grown CNTs with 1% activated tween in water for 30 mins - Incubate with avidin in PBS	High	Low

3.8 PDMS devices fabrication and functionalization

In order to compare the performance of our nanoporous microfluidic elements with that of traditional solid elements, we chose PDMS as the solid matrix. It is one of the most widely used materials in microfluidics laboratories and has highly standardized fabrication and functionalization protocols. PDMS features as well as channels were generated using standard soft lithography. SU-8 photoresist (Microchem) was patterned on a silicon wafer by

photolithography to form a negative mold. A 10:1 mixture of polydimethylsiloxane (PDMS) pre-polymer and curing agent (Sylgard 184, Dow Corning) was poured onto the mold and baked at 75°C until cured. The PDMS devices were then bonded to 1"x3" glass microscope slides after oxygen plasma treatment.

PDMS devices were functionalized using previously described methods [8]. Freshly bonded devices were pretreated with 4%(v/v) solution of 3-mercaptopropyltrimethoxysilane in ethanol for 30 min at room temperature, followed with incubating with 0.01 μmol/mL GMBS in ethanol for 15 min at room temperature. NeutrAvidin and biotinylated antibodies are then added in the same way as for the CNT devices.
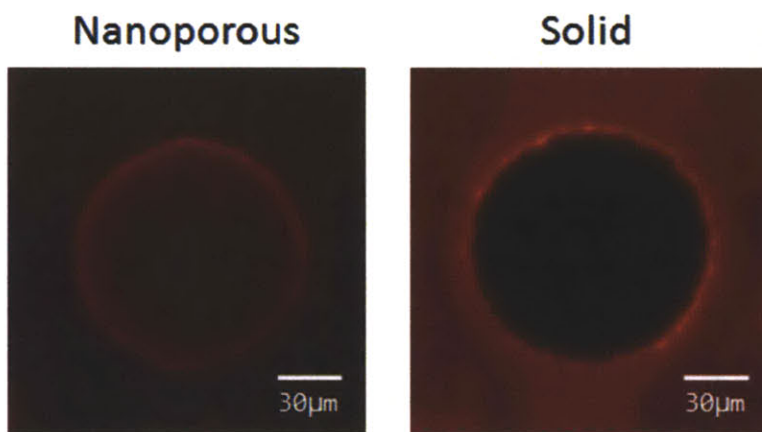
Nanoporous   Solid

Fig. 3-15: Functionalization comparison using fluorescent NeutrAvidin. A 100 μm diameter nanoporous CNT post is compared with a 100 μm diameter solid PDMS post. The solid post is dark inside since fluorescent NeutrAvidin cannot penetrate.

Two different surface functionalization methods were used for the CNT nanoporous structures and the PDMS solid structures. To ensure that the improvement in capture found with the nanoporous structures (see Chapters 4 and 5) is not a result of the difference in functionalization efficiency, the density of avidin binding sites on each type of structure was qualitatively compared using the two functionalization strategies. The functionalization steps were performed for CNT devices using the CDI-activated Tween method in section 3.7, and for PDMS devices as described above, up to the NeutrAvidin incubation stage. Here fluorescent NeutrAvidin was used instead. After 30 minutes incubation at room temperature, unbound NeutrAvidin was rinsed off with PBS, and the fluorescence compared under a microscope. Figure 3-15 shows the results for

a nanoporous CNT post compared with a solid PDMS post. 500 ms exposure was used for all images. The comparison shows that there appears to be more NeutrAvidin binding on the PDMS surface than on the CNT surface, thus the increased capture for the nanoporous CNT structures is not attributable to an advantage in surface functionalization.

This chapter introduced the inclusion of VACNT forests as new structural elements in the microfluidics toolbox, with unprecedented ability for geometric control. Two techniques were developed for incorporating VACNT elements inside of microfluidic channels. Devices created by these techniques were characterized for wetting, permeability, particle accessibility, and functionalization. The high permeability of the VACNT forest compared to other nanoporous materials was explained by its ultra-high (99%) porosity, taking advantage of the non-linearity of the porosity-permeability relationship. The work performed in this chapter sets the foundation for subsequent experiments using VACNT elements in microfluidic devices for bioparticle separation.

Chapter 4

Mechanical and chemical particle separation using nanoporous VACNT microdevices

This chapter explores various examples of particle separation, taking advantage of both the nanoscale porosity and the microscale patternability of the VACNT elements for mechanical separation, as well as the chemically functionalized elements for specific particle capture. Section 4.1 starts with a simple mechanical filter that uses the nanoporosity of the VACNT forest as the filtration cut-off size. In section 4.2, the forest is functionalized to allow specific capture of nanoparticles inside a rectangular filter whilst mechanically trapping microparticles in front of the filter. Then, instead of rectangular filters, a circular post was used to specifically isolate nanoparticles and microparticles on the inside and outside of the post respectively (4.3). Section 4.4 demonstrates simultaneous mechanical and chemical separation of three different particle types across four orders of magnitude in size, using an array of nanoporous microposts. Finally, we show isolation examples of real biological particles (bacteria and cells) in section 4.5, and observe that capture efficiency is 5-7 folds higher with nanoporous capture elements compared to solid elements of the same external geometry.

4.1 A mechanical filter layout for continuous particle separation and concentration

A straight-forward yet powerful application that takes advantage of the high porosity and ease of patterning of the nanoporous CNT structures is mechanical filtration. In Figure 4-1 we demonstrate continuous filtration and concentration by micro-patterning a Y-shaped nanoporous filter. The filter sidewalls are made from 100 μm wide CNT forests. It narrows from a 3mm wide section, bounded by the PDMS channel walls, to a 100 μm wide section, bounded by nanoporous CNT filter walls. A schematic of the chip design is shown in Figure 4-1(a), and an SEM of the CNT filter structure in Figure 4-1(b).

The CNT features are fabricated as described in section 3.1 and integrated into PDMS channels using the method in 3.2.1. To ensure that there are no gaps between the CNT filter edge and the channel sides, we made the CNT filter 20μm wider than the channel and carefully aligned the two during bonding. The bonded devices were pre-wetted and blocked against non-specific binding with 0.5% Tween-20 in DI water. 10 μm green fluorescent polymer beads suspended in DI water with 0.1% Tween (Duke Scientific) were injected at 10 μL/min using a syringe pump. A longer piece of outlet tubing was used for the particle outlet than the waste outlet. This increases the resistance of the sample outlet compared to the waste outlet, which in turn increases the level of sample concentration. Flow from both outlets were collected and imaged under a fluorescent microscope.

In this device configuration, large particles (10 μm fluorescent green beads), which cannot pass through the 80 nm-spaces between CNTs in the nanoporous forest, are guided by the barrier into the narrow neck of the Y-filter (Fig. 4-1(d) and (e)), whereas fluid and particles smaller than 80 nm efficiently pass through the barrier (red BSA molecules, ~10nm, Fig. 4-1(c)), resulting in an 11-fold concentration of the larger particles in the sample (inlet and outlet circles, Figure 4-1(a)). The degree of concentration is controlled by the relative flow resistances of the particle flow path and the waste flow path. Factors that control the respective path resistances include the ratio of the overall PDMS channel width versus the width of the narrow particle flow channel outlined by VACNT walls, the permeability and width of the VACNT filter walls (both factors contribute to the flow resistance across the filter), and the resistance of the outlet tubings. Higher concentration factors could be achieved by increasing the ratio of the overall PDMS channel width to the nanoporous passage width, by increasing permeability of the VACNT forest, by using thinner VACNT filter walls, or by adjusting the outlet tubing resistances. Although this device performs simple size-exclusion filtration, it is more powerful than traditional membrane filters in that its continuous-flow design ensures that clogging of the filter does not occur. Its practical application could include cell concentration from dilute bodily fluids (such as peritoneal lavage and urine), or bacteria isolation from environmental samples.
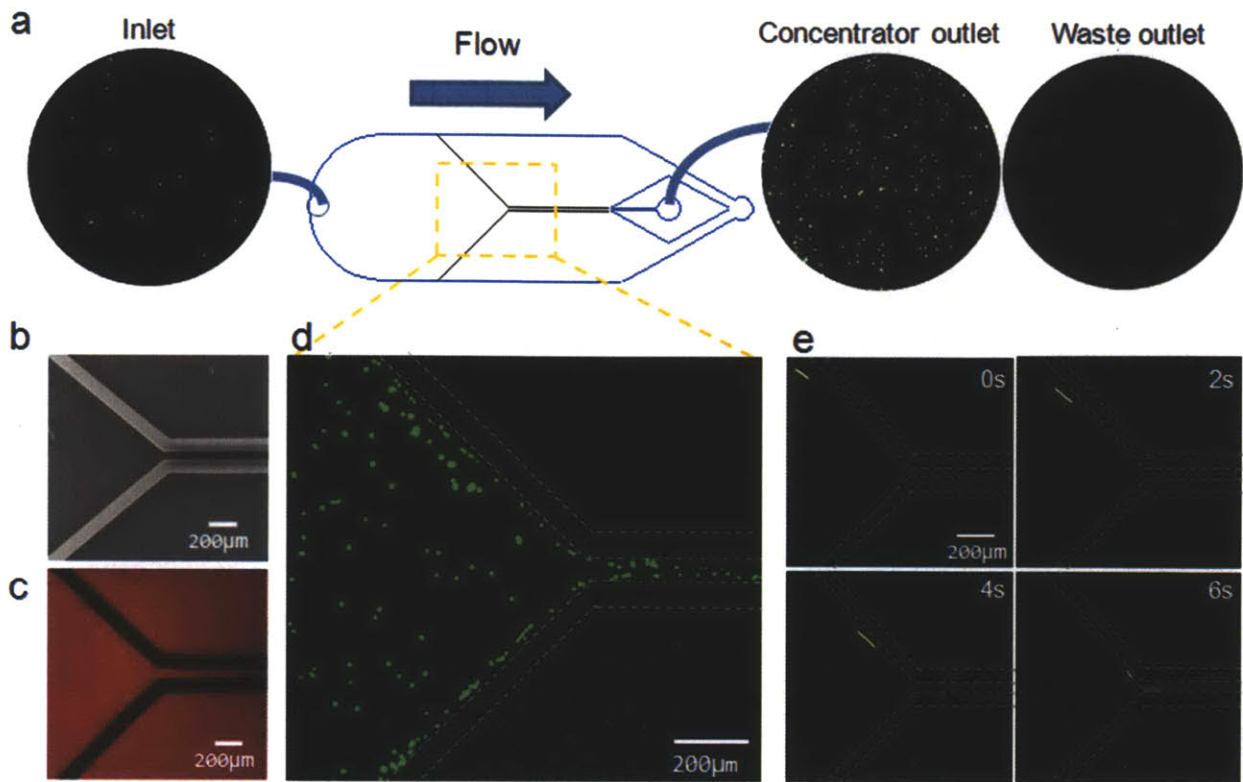
Fig. 4-1: Nanoporous Y-Filter. (a) Device schematic. Overall dimensions 3 mm(W) x 20 mm(L) x 100 μm(H). Inside width of nanoporous central channel is 100 μm. Blue lines are PDMS channel boundaries, black lines show filter structure. Circular insets show micrographs of the inlet, concentrator outlet and waste outlet, showing selective concentration of 10μm fluorescent beads. (b) SEM image of the nanoporous filter. (c) Fluorescent micrograph showing red fluorescent BSA molecules have passed through the nanoporous barriers. (d) 10μm polymer beads cannot pass through the nanoporous filter sides, and are directed to the central channel. (e) Streak images of a single 10μm bead as it enters the constricted section of the filter.

4.2 Simultaneous mechanical and chemical separation using a simple filter

In this example, the mechanical filtration capabilities of the VACNT forest is combined with surface chemistry to design a device that can specifically capture virus-sized particles whilst mechanically excluding bacteria sized particles. Figure 4-2 (a) illustrates the simple rectangular block filter design, along with device dimensions. The CNT filter was fabricated as in 3.1 and integrated into PDMS channels using the method in 3.2.1. To ensure that there are no gaps between the CNT filter edge and the channel sides, the CNT filter was made 20μm wider than

the channel and carefully aligned the two during bonding. The non-functionalized filter was pre-wetted and blocked against non-specific binding with 0.5% Tween-20 in DI water. The functionalized filter was attached with NeutrAvidin using steps described in 3.7. Particles used were 40 nm Strepavidin-coated red fluorescent beads (Invitrogen), and 1μm uncoated green fluorescent beads (Duke Scientific), suspended in DI water, with 0.1% Tween-20.
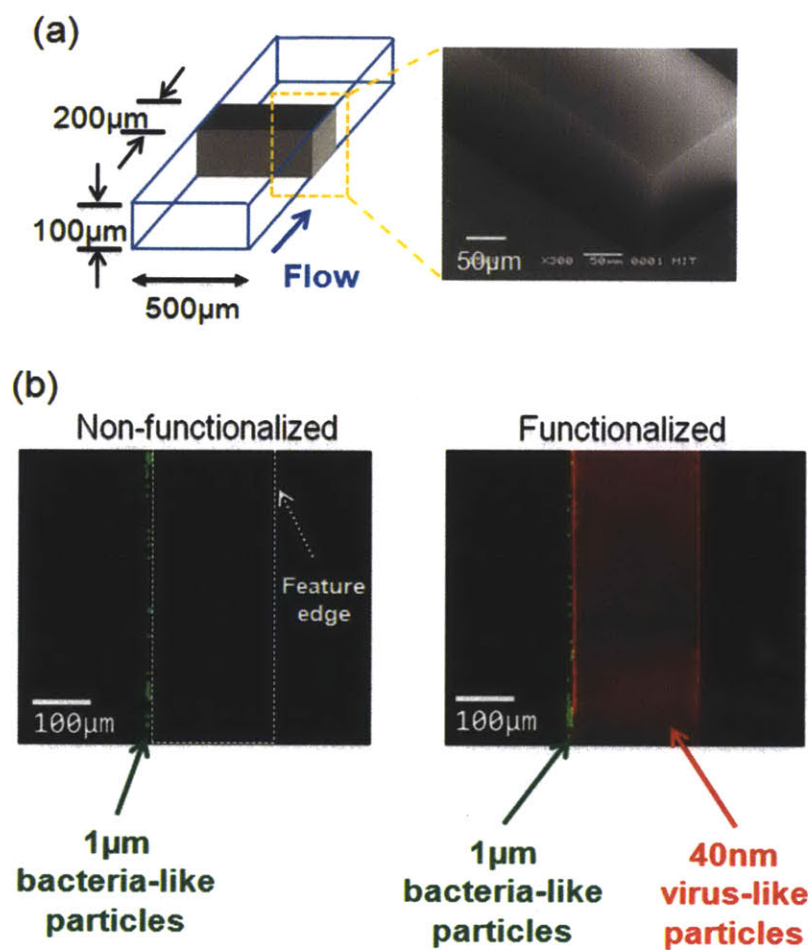
Fig. 4-2: Rectangular VACNT forest filter (a) Device geometry and SEM (b) Comparison between non-functionalized and avidin-functionalized filters when a mixture of 1μm bacteria-like particles and 40nm virus-like particles are injected into the device.

Fig. 4-2(b) shows that the filter mechanically excludes 1 μm size particles, which are larger than the 80 nm spacing between individual nanotubes in the forest, whilst chemically trapping the 40 nm beads, which can flow through the nanoporous structure. Since there are ~10^8 individual CNTs per mm^2 of forest, a 400x increase in surface area inside a 100 μm height

channel is achieved, and particles traveling through the forest will encounter a high degree of contact with the functionalized CNT sidewalls. Figure 4-2(b) further illustrates that without avidin functionalization, the biotin-coated nanoparticles are not captured inside the forest, whereas with functionalization, the particles are trapped inside the VACNT filter.

4.3 Specific separation of two different particle sizes using a nanoporous cylindrical post

Here we use a cylindrical post design fabricated from VACNTs for specifically isolating two different particle sizes, and compare capture results with a solid PDMS post of the same geometry. Both posts are 1000μm in diameter, 100μm high, and centered inside a 2mm x8mm x100μm PDMS channel. They are functionalized with NeutrAvidin using procedures described in sections 3.7 (for VACNT) and 3.8 (for PDMS) respectively. A mixed suspension of 2μm red fluorescent biotin-coated beads (Invitrogen) and 40nm green fluorescent biotin-coated beads (Invitrogen) are injected through the device by a syringe pump, at 20μL/min. This is followed by flushing of the device using DI water at 20μL/min for 2 minutes. Illustration of the device and fluorescent images of the bead capture is shown in Figure 4-3(a). We first observe that the green 40nm particles are captured both on the inside and the outside of the nanoporous post, but only on the outer surface of the solid post. Thus there is much greater capture of the nanoparticles. We also see increased capture of the 2μm beads on the outside of the nanoporous post compared to the solid post. Figure 4-5(b) quantifies this difference in capture across several time points during the particle injection. We see on average a 5x improvement in capture for the nanoporous post. Thus we find that transitioning from a solid to a nanoporous design greatly improves the capture efficiency for both nanoparticles that can penetrate inside the pores, and for microparticles that are captured on the outer surface of the element. The improvement in nanoparicle capture is due to an increase in available surface area and a decrease in diffusion distance inside the nanoporous matrix of the VACNT forest. The improvement in microparticle capture is due to an improvement in interception efficiency in a nanoporous post compared to a solid post. This will be discussed in detail in Chapter 5, including multi-element organizations of VACNT posts.
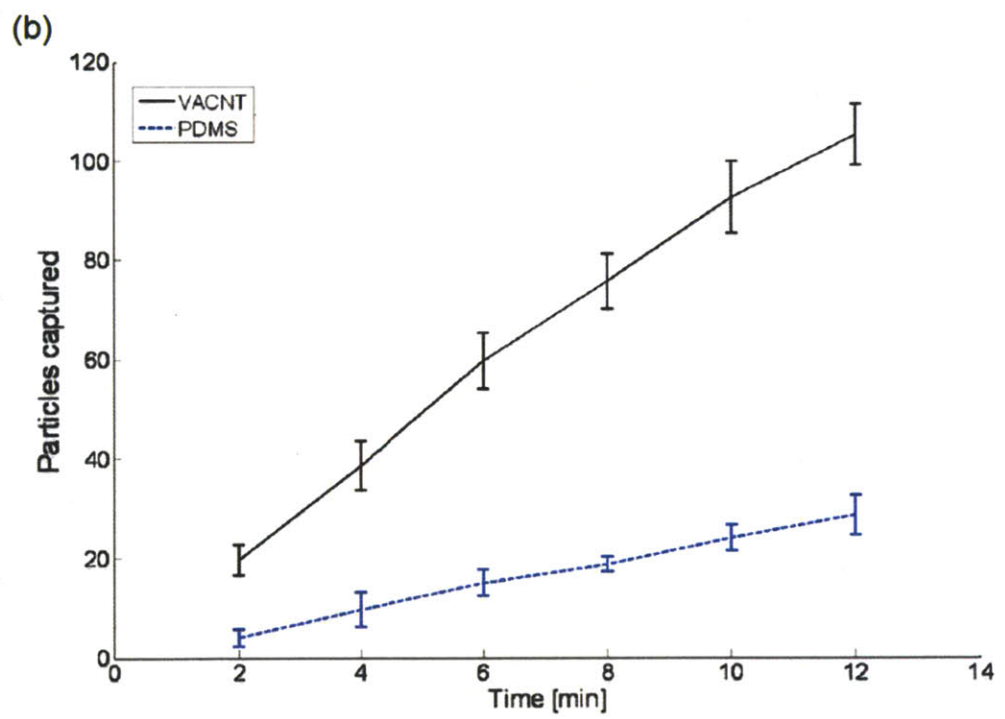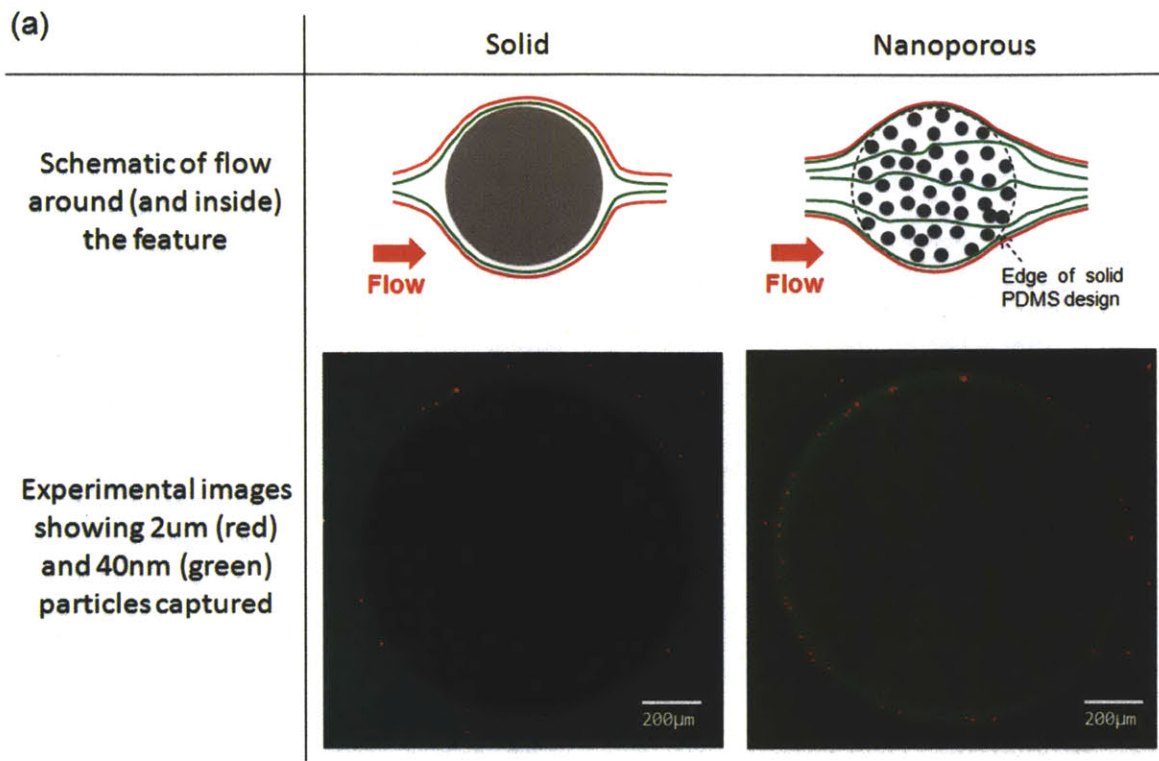
Fig. 4-3: (a) Isolation of 2μm (red) and 40nm (green) biotin-coated beads using avidin-functionalized, cylindrical PDMS and VACNT posts. (b) Particle capture with time for the specific isolation of 2μm beads using solid (PDMS) and nanoporous (VACNT) elements.

4.4 Simultaneous mechanical and chemical separation of three different particle sizes using an array of nanoporous posts
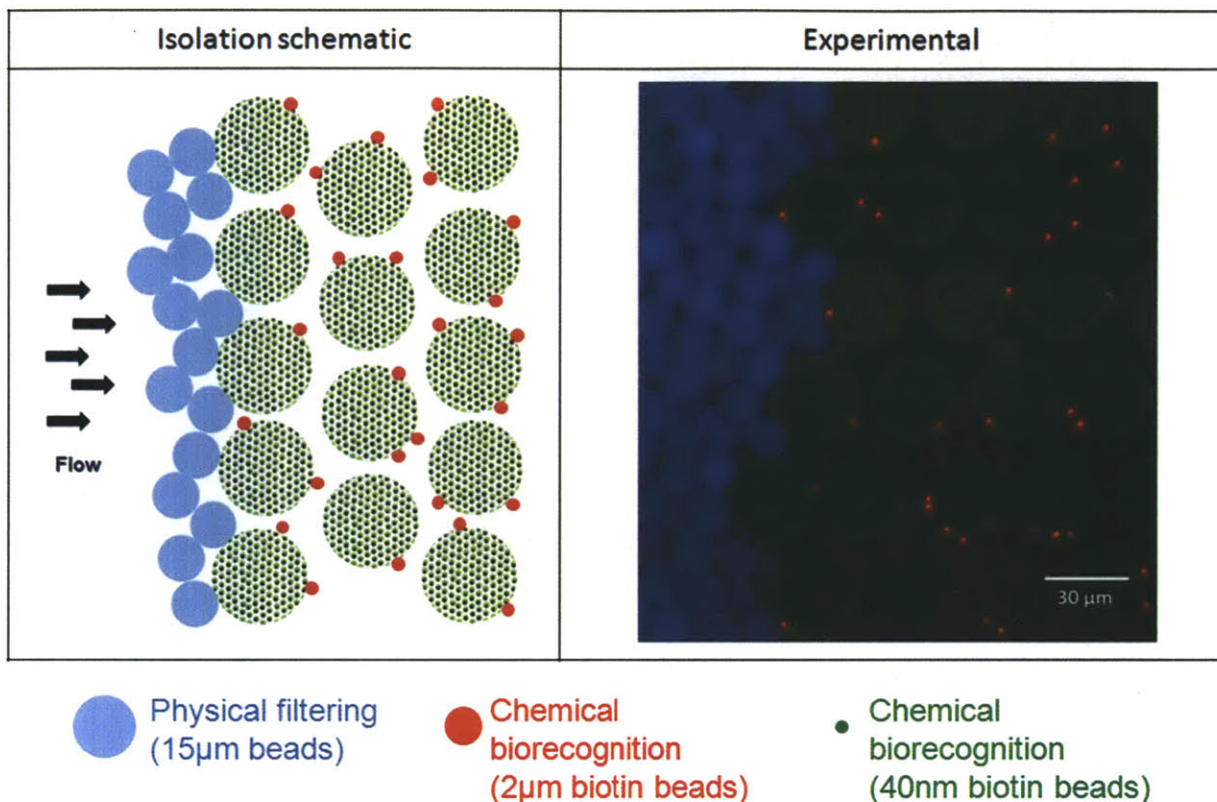
Fig. 4-4: Isolation of bioparticles over 3 orders of magnitude in size using a nanoporous VACNT post array. Posts are 30μm in diameter with 5μm spacing.

To further demonstrate the flexibility of the VACNT technology, in Figure 4-4 we present an additional device configuration that enables simultaneous isolation of three different particle types ranging over 3 orders of magnitude in size: blue 15μm polystyrene beads, red 2μm biotin-coated particles, and green 40nm biotin-coated beads. The device consists of an array of cylindrical micropillars (30μm diameter, 100μm tall) that are spaced 5μm apart from each other and that were wet functionalized with avidin (see Section 3.7). The VACNT platform combines micro- and nano-porosity to achieve simultaneous mechanical filtration and chemical bioparticle capture: the intra-pillar distance (5μm) defines the microscale pores, while the intra-CNT spacing (~80nm) defines the nanoscale porosity. Particles larger than the micro-scale pores cannot penetrate the array of functional elements and are mechanically filtrated at the front edge of the device, as is the case for the blue 15μm polystyrene beads. On the other hand, particles that are

smaller than the micro-pores yet larger than the average intra-CNT spacing can enter the functional array of elements (but not the nanoporous micropillars) and are captured on the micropillars' surfaces using chemical affinity (red 2μm beads). Finally, particles whose size is below the nano-pore threshold can flow through the VACNT micropillars and are isolated inside the functional elements using chemical biorecognition (green 40nm beads). This example demonstrates the ability of VACNT-enhanced microfluidic devices to enable simultaneous multiphysics, multiscale bioparticle isolation on a single chip.

4.5 Specific separation of biological particles using VACNT elements

In this section, we present examples with specific isolation of real biological particles of diagnostic interest, comparing capture using nanoporous VACNT elements with those using solid PDMS elements of identical geometry. We chose one example of mammalian cell capture and two examples of bacterial cell capture with relevant diagnostic applications. The mammalian cell we used was human CD4+ T-cells, which are 7-9μm in size. CD4+ T cells, also known as helper T cells, are a subtype of lymphocytes that play an important role in adaptive immunity. It is also the cell type specifically invaded by the human immunodeficiency virus (HIV). The concentration of CD4+ T cells (known as the CD4 count) is an important diagnostic measure of disease progression in HIV patients [8]. The two bacterial cell types we used were *Escherichia Coli* and *Streptococcus Pneumoniae*. *E. coli* is an enteric organism commonly used as a model bacteria. It is a rod-shaped cell around 2μm in length and 0.8μm in diameter. *S. Pneumoniae* is a common cause of pulmonary infections. It has a spherical geometry, and is around 1μm in diameter. Because clinical *S. Pneumoniae* samples are found in sputum, processed sputum was used as the suspension medium for the experiments.

Figure 4-5 shows capture of CD4+ T cells on a single 500μm VACNT post versus a PDMS post. The channel is 3mm(W) x 20mm(L) x 100μm(H), and the post is separated from the channel wall and any neighboring posts by 200μm (Chapter 5 will discuss why this is important). The posts are functionalized with biotinylated anti-CD4 antibody (clone 13B8.2 Beckman Coulter) using the protocols in 3.7 (CNT) and 3.8 (PDMS). Control devices were treated with 0.5% Tween-20. Peripheral Blood Mononueclear Cells (PBMCs) were obtained from healthy volunteer blood and fluorescently stained with Calcein dye. The cells are injected into the

devices at a flow rate of 10 µL/min for 5 minutes, and then flushed with PBS buffer for 2 minutes at 20uL/min. Fluorescent microscopy was used to image the capture. Cell capture counts were conducted manually. We see from Figure 4-5(b) that the capture on the nanoporous post is much greater than on the solid post. Across several devices, we found that on average there is a 5x improvement in capture on nanoporous posts compared to solid posts. The insets in 4-5(b) show no capture on the non-functionalized control devices, showing that non-specific binding was low for both VACNT and PDMS posts.
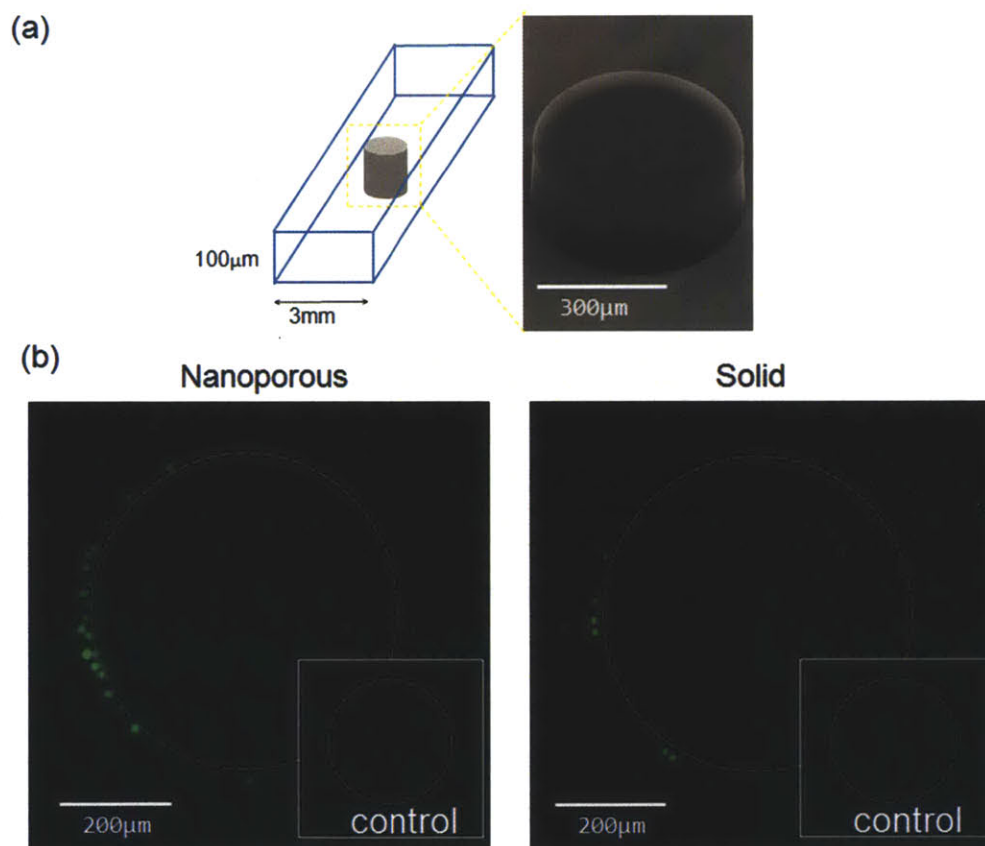
Fig. 4-5: Specific isolation of CD4+ T-cells on nanoporous and solid posts (a) Schematic of channel and post geometry. (b) (a) 10 µm size fluorescently labeled CD4+ T-cells are captured on 500 µm diameter posts. Comparison in capture between nanoporous and solid posts of identical geometry shown. Control boxes show capture on non-functionalized devices.

(a)

(b)
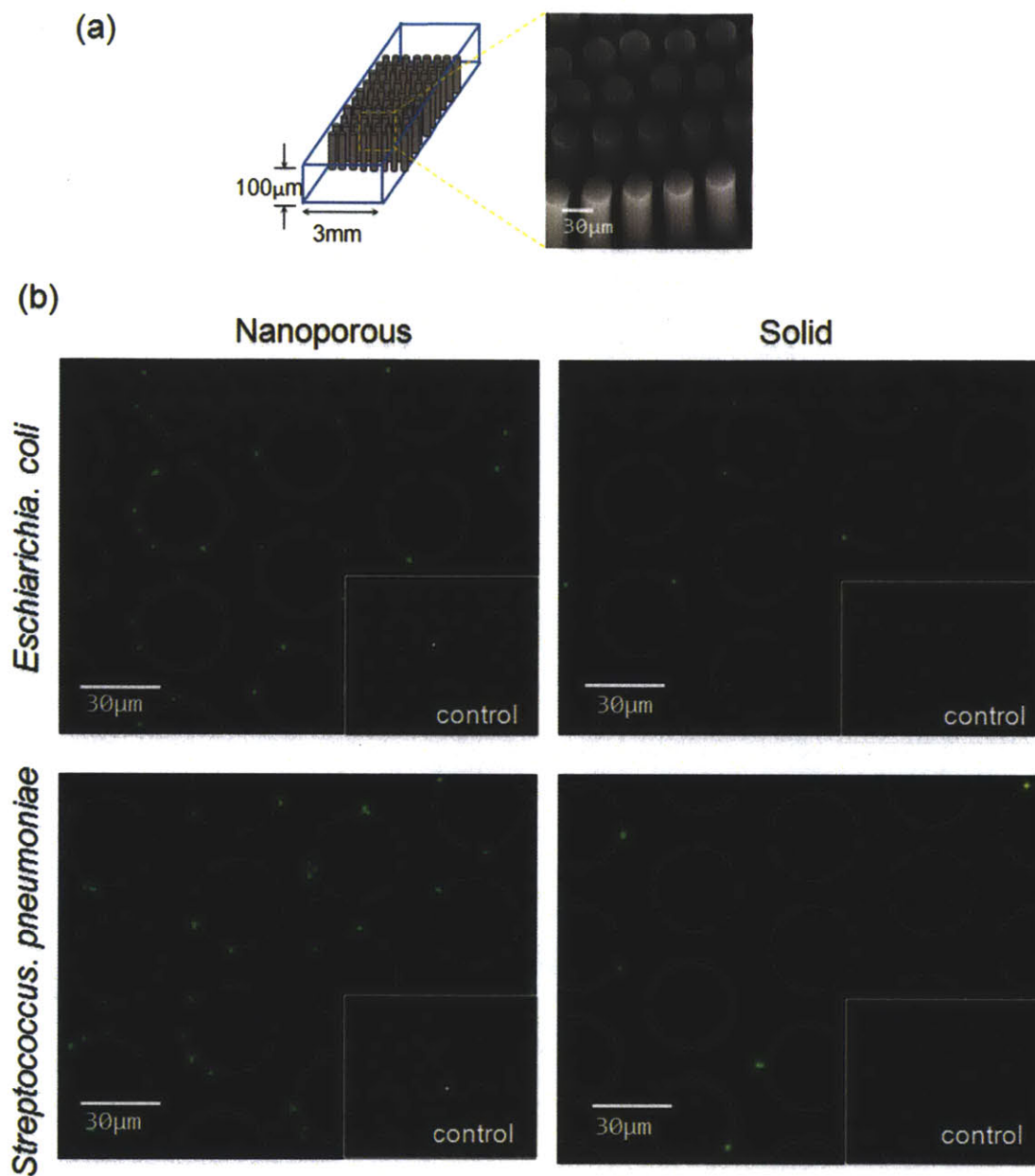
Fig. 4-6: Specific isolation of *Eschiarichia coli* and *Streptococcus pneumonia* bacteria on nanoporous and solid post arrays (a) Device schematic of 30μm post arrays. (b) Capture of ~1μm-size *e. coli* and *s. pneumoniae* bacteria cells. Nanoporous and solid post arrays with identical geometries are functionalized with anti bacterial antibody, and fluorescently labeled bacteria samples are flowed through the device. Control boxes show capture on non-functionalized devices.

Figure 4-6 shows specific capture of two different bacteria types using an array of 30μm posts spaced 5μm apart, inside a channel with dimensions 3mm(W) x 20mm(L) x 100μm(H). The posts are functionalized with biotinylated anti-*e. coli* antibody (rabbit polyclonal, Abcam) and anti-*s. pneumoniae* antibody (rabbit polyclonal, Abcam) respectively. using the protocols in 3.7 (CNT) and 3.8 (PDMS). Control devices were treated with 0.5% Tween-20 to block non-specific binding. Heat killed, fluorescent *e. coli* cells (Invitrogen) were suspended in PBS. Live *s. pneumonia* cells were obtained from the Fortune lab at the Harvard School of Public Health, and fluorescently stained with Alexa Fluor 488 carboxylic acid, 2,3,5,6-tetrafluorophenyl ester (Invitrogen). These are suspended in processed sputum from healthy volunteers, and diluted 2x with PBS. The cells are injected into the devices at a flow rate of 10μL/min for 2 minutes, and then flushed with PBS buffer for 2 minutes at 20μL/min. Fluorescent microscopy was used to image the capture. Cell capture counts were conducted using ImageJ. It can be seen from Figure 4-6(b) that the capture on the nanoporous post is much greater than on the solid post for both bacteria types. Across several devices, it was found that on average there is a 6-7x improvement in capture on nanoporous posts compared to solid posts. The insets in 4-5(b) show very little capture on the non-functionalized control devices, showing that non-specific binding was low for both VACNT and PDMS posts.

This chapter introduced several device concepts for mechanical and chemical separation of a range of model and biological particles. These ranged from simple size-based mechanical filtration, to simultaneous multi-scale, multi-physics separation of three different particle types ranging nearly four orders of magnitude in size. In the case of simple filtration, the high permeability of the VACNT forests help to achieve high sample throughput. On the other hand, the micro-patternability of the VACNT features make more complex designs possible to fabricate. With both model and biological particles, it was found that even for the particles that are too large to fit inside the VACNT forest, the capture efficiencies of nanoporous elements are much higher than that of solid elements. This observation will be more rigorously explored in the next chapter.

Chapter 5

Particle interception in solid and porous flow systems

In the previous chapter, there was some indication that particle isolation, even for particle sizes greater than the VACNT forest spacing, is more efficient using porous rather than solid microfluidic elements. Isolation efficiency is a function of the interception efficiency (the fraction of particles in flow that is intercepted by the collector) and the binding efficiency (the probability that a particle will bind to the collector if it is intercepted). Since there is no evidence to suggest that binding efficiency is any higher on our VACNT elements for particles larger than the forest spacing (section 3.8 suggests the opposite), we believe the major advantage of porous elements lies in the enhancement in interception efficiency. The widely used definition of interception efficiency is given by $\eta = b/d_c$, where b is the span of particles upstream that are ultimately intercepted by the collector, and d_c is the collector diameter (Fig. 5.1). To understand interception through theory and experiment, the popularly used, and simple to model geometry of a cylindrical post was selected. Section 5.1 begins with some qualitative observations on interception improvement. Sections 5.2 and 5.3 examine the different factors that affect interception efficiency in the flow regime of a typical microfluidic system, and understand the mechanisms that limit interception in solid elements. Section 5.4 lays down the theoretical foundation for modeling mixed porous and free media flow, and 5.5 describes a model for particle interception for solid and porous cylindrical posts. This model was put to the test against experimental results for particle interception using both isolated posts (section 5.6) and post arrays (section 5.7). In each case, there is good agreement of theory and experiment to demonstrate that interception efficiency can be greatly improved by using nanoporous posts instead of solid posts of the same geometry. Finally, section 5.8 returns to capture of real biological particles to show that the interception efficiency increase also translates to isolation efficiency enhancement.

$$\eta = b/d_c$$
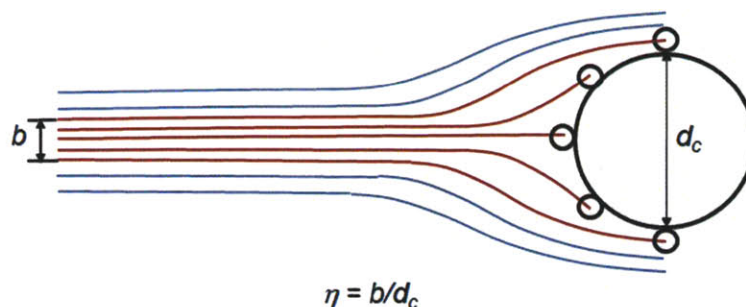
Fig. 5-1: Schematic defining interception efficiency

5.1 Qualitative observations on improvement in particle interception by porous elements compared to solid elements

It was expected that fluid flow through a porous structure could alter the flow characteristics of the fluid path in the vicinity of the structure, including altering the flow streamlines. This phenomenon was investigated by flowing suspensions of 10 μm diameter beads through a microchannel containing nanoporous post elements, and tracking the beads' flow trajectories around a single post. The posts were 500 μm in diameter and 100 μm in height, sealed inside a 3 mm x 20 mm x 100 μm PDMS channel. The channel walls and neighboring posts were 200μm away from the post examined. 0.5% Tween-20 in DI water was used to block non-specific binding. Particles used were 10μm diameter green fluorescent polymer particles (Duke Scientific) suspended in water with 0.1% Tween-20. Flow injection was via a syringe pump set to 20 μL/min. Video images were recorded using NIS elements software. Particle paths were traced using the manual tracking plug-in on ImageJ.

Figure 5-2(a) (left) shows superimposed particle tracks from multiple beads flowing around the nanoporous post. For comparison, flow trajectories around a 500μm diameter solid PDMS post are also shown (Fig. 5-2(a), right). It was observed that the tracks around the nanoporous post are concentrated in an area that is closer to the post surface than the tracks around the solid post. A comparison of several snapshots of two single particles approaching each type of post from the same start position demonstrates that some particle trajectories can only be captured with the nanoporous post (Fig. 5-2(b)). Collecting the trajectories of multiple beads shows that, when solid posts are used, only particles approaching at less than 2.5 μm away from the centerline

contact the post, whereas nanoporous posts ensure 100% interception of bioparticles approaching from as far as 15 µm away from the post centerline (Fig. 5-2(c)).
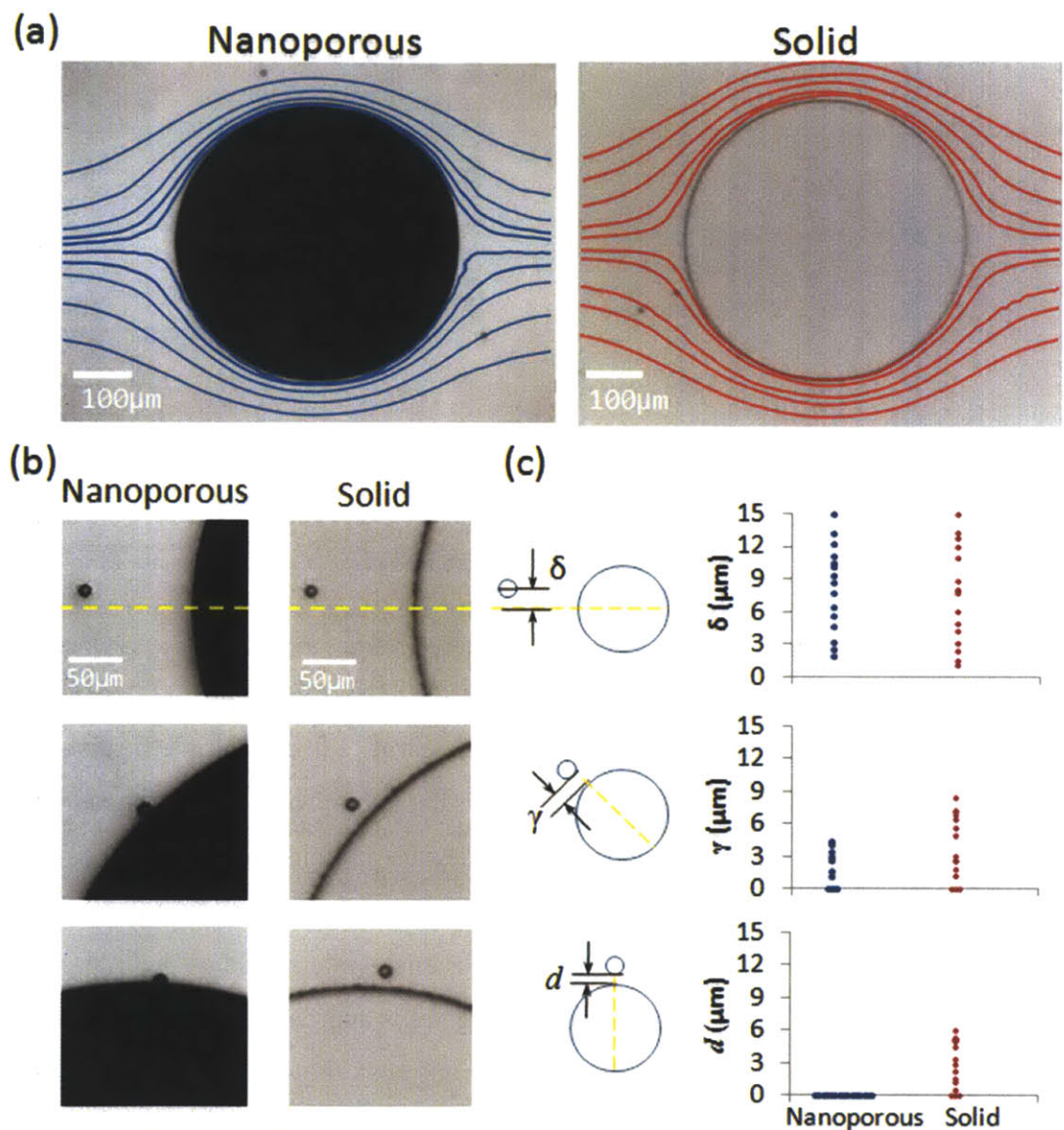
Fig. 5-2: Nanoporous elements alter particle flow paths. (a) Particle streamline tracks of 10 µm beads around a nanoporous post and a solid post, showing tightening of the particle tracks towards the element surfaces due to the nanoporous post altering the flow. (b) Snapshots of single particles approaching a nanoporous circular post element and a solid post from the same start position. The particle approaching the nanoporous post eventually touches the post, and the one approaching the solid post never does. (c) Positional data of multiple beads as they approach both posts. All beads approaching the nanoporous post from 15 µm or less away from the centerline contact the post (γ or d = 0), with most never reaching the solid post.
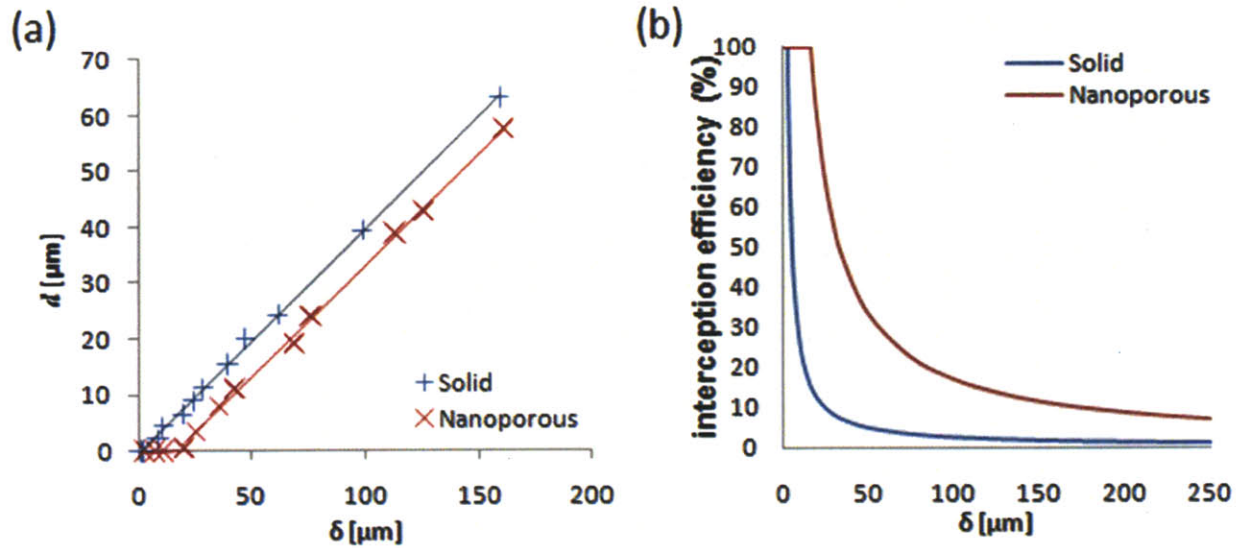
Fig. 5-3: Analysis from following multiple bead tracks around nanoporous and solid posts. d and δ are defined as in Fig. 5-2. (a) Minimum distance between a particle and the post, given the particle's initial distance away from the centerline as it approaches the post. (b) The percentage of beads that will touch the post if multiple incoming beads are randomly distributed within a distance δ about the center line.

Figure 5-3 presents more detailed analysis of the particle tracks from multiple beads approaching the same 500μm post system. 5-3(a) shows data points of individual bead positions when they are 200 μm in front of the posts and when they are at their closest to the posts. Beads approaching the nanoporous post pass several microns closer to the post surface than their counterparts approaching the solid post. In Figure 5-3(b) this is interpreted as the interception efficiency. To achieve 100% interception, the incoming beads approaching the solid post must fall within 2.5 μm of the centerline, but for the nanoporous post, they can be within 15 μm of the centerline.

5.2 Theoretical background on mechanisms of particle interception

A number of theoretical and experimental studies exist on particle interception across scientific disciplines ranging from aerosol science [111, 112] to marine ecology [113, 114]. There are four classical mechanisms for interception: direct interception, diffusion, inertial compaction, and gravitational sedimentation. The basic concepts of these are illustrated in figure 5-4 below.
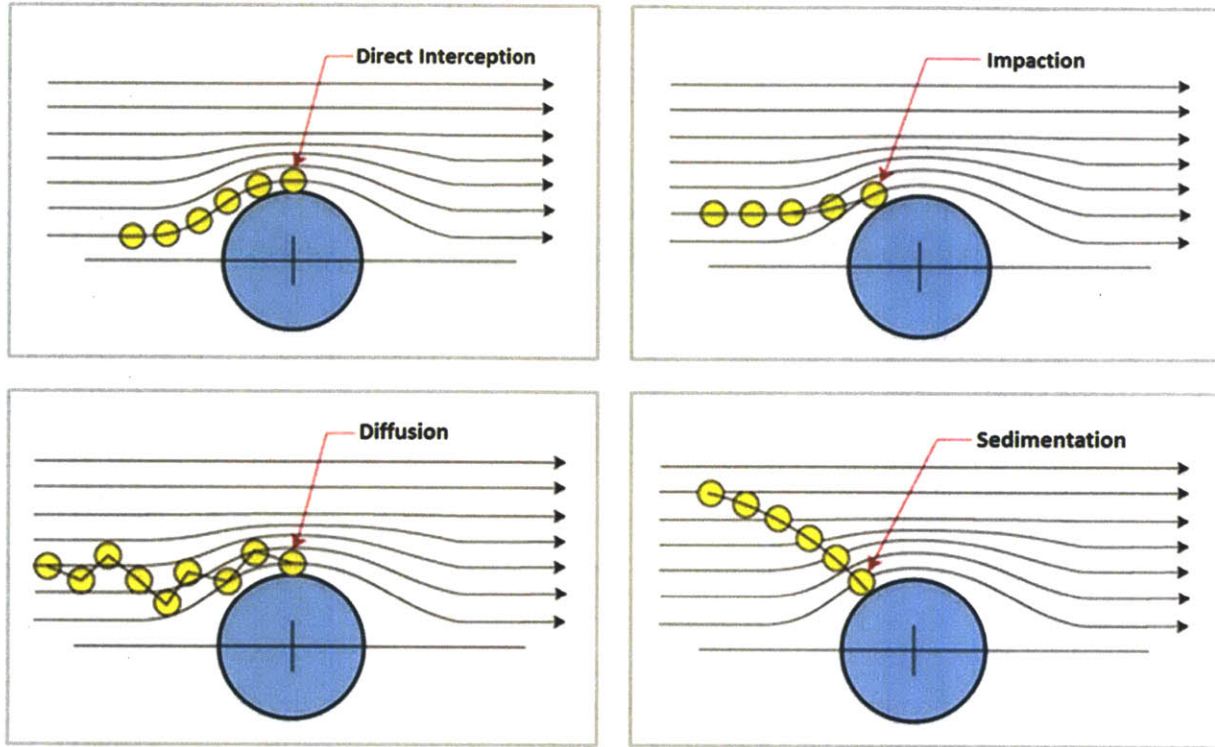
Fig. 5-4: Illustrations of the four classical mechanisms of interception [12]

The mechanism of direct interception occurs due to streamline kinematics. When a particle of a finite size travels along a streamline that approaches a collector by a distance less than the particle radius, the particle is brought directly into contact with the collector by simply following the fluid streamline. For low Reynolds number flows found in our experimental systems, the interception efficiency due to direct interception has been analytically solved as [115]:

$$\eta = A_F \left(\frac{d_p}{d_c}\right)^2 \tag{5.1}$$

where

$$A_F = \left[2 - \ln\left(\frac{2aU}{v}\right)\right]^{-1} \tag{5.2}$$

for isolated solid cylinders, and

$$A_F = \left[-\ln\alpha - \frac{3}{2} + 2\alpha - \frac{\alpha^2}{2}\right]^{-1} \tag{5.3}$$

for cylinder arrays with volume fraction α. Since a porous collector will alter the streamline distribution around it compared to a solid collector, we expect direct interception to be altered as a result of using a nanoporous instead of a solid post.

Brownian diffusion of small particles in a fluid can cause them to randomly cross streamlines, increasing their probability of getting intercepted by the collector. This probability is greatly enhanced as their diffusive activity increases, due to increases in temperature, small particle size, or long residence time in proximity to the collector. The contribution of Brownian diffusion as a mechanism of interception is additive with the effect due to direct interception, and is derived for a cylindrical collector as [116]:

$$\eta_{diff} = \frac{3.64 A_F}{Pe^{2/3}}$$

(5.4)

Where Pe is the Peclet number (convection/diffusion), LU/D, where L is the characteristic length, U is the average velocity in the channel, and $D = kT/6\pi\mu a_p$ is the diffusion coefficient (k is the Boltzmann constant, T is temperature in Kelvin, μ is viscosity, and a_p is the particle radius)

In our experimental system, where particle sizes are between 1 and 100μm, diffusion is generally not an important contributor. In our system, Pe ranges from 2 x 10^4 (1um particle, 50um collector) to 1 x 10^7 (10μm particle, 500um collector) and η_{diff} ranges from 0.0009 to 0.00003. We will later show that direct interception ranges from 0.001 to 0.2 in our experiments. Thus diffusion does play a significant role for the very smallest particles we use (1μm and 2μm diameter), and for the bacteria experiments, but not for the larger particle sizes. Diffusion affects both nanoporous and solid posts equally.

Inertial compaction occurs when a particle's inertia causes it to deviate from the fluid streamlines and collide with the collector. This is the dominant mechanism for aerosol particles in air. The relative importance of inertial compaction is given by the Stoke's number, defined as the ratio of the stopping distance to the cylinder radius:

$$Stk = \frac{1}{9} Re\left(\frac{d_p}{d_c}\right)^2 (s-1)$$

(5.5)

where Re is the Reynolds number, d_p is the particle diameter, d_c is the collector diameter, s is the specific gravity. Aerosol theory states that inertial impaction is negligible for $Stk < 0.125$ [112]. For our experimental conditions, $Stk < 5 \times 10^{-4}$, well below the critical value.

Gravitational sedimentation can give rise to particle interception when the cylindrical axis of the collector is oriented horizontally, such that particles traveling along streamlines above the collector can settle on top of it [117]. To eliminate the effects of this mechanism, all or our posts are oriented with their cylindrical axis in a vertical direction. The effect of gravitational sedimentation can also be minimized by using particles that are neutrally buoyant with the fluid medium.

Of the four classical mechanisms of interception described, direct interception is the dominant effect in our system of concern, that is, low Reynolds number flows with particle sizes >1μm. Diffusion will also play a role for the smallest particle sizes. However, the previous analysis of interception using classical mechanisms neglects some important physical effects that come into play when the particle is in the immediate proximity of a solid surface. These near-surface effects include hydrodynamic resistance between the particle and collector, and London forces of molecular attraction. Hydrodynamic resistance (sometimes referred to as a 'lubrication' force) arises as a particle approaching a solid surface 'squeezes out' fluid from the gap in between them. According to the no-slip condition, this would result in infinitesimally slow fluid drainage as the gap size reduces, and the particle would never contact the surface. The particle is saved from this fate by the opposing attractive London (or van de Waals) force that dominates when the gap length approaches molecular dimensions [115]. Goren [13] and Spielman [118] analyzed the effects of these forces and summarized their combined effect on direct interception using the parameter N_{Ad}, known as the adhesion coefficient:

$$N_{Ad} = \frac{H d_c^2}{9\pi\mu d_p^2 U A_F}$$

(5.6)

where H is the Hamaker constant. At large values of N_{Ad}, the London force dominates, resulting in a higher interception efficiency than that predicted by streamlines from direct interception; at small values of N_{Ad}, hydrodynamic resistance has the largest effect, resulting in a lower interception efficiency than that predicted by direct interception. In general, for larger particle

sizes (>1μm), which is our operating regime, N_{Ad} is small, and hydrodynamic resistance dominates. The relationship between N_{Ad} and the adjustment factor for interception efficiency (adjusted efficiency/efficiency predicted by direct interception), as calculated by Goren [13], is shown in figure 5-5 below.
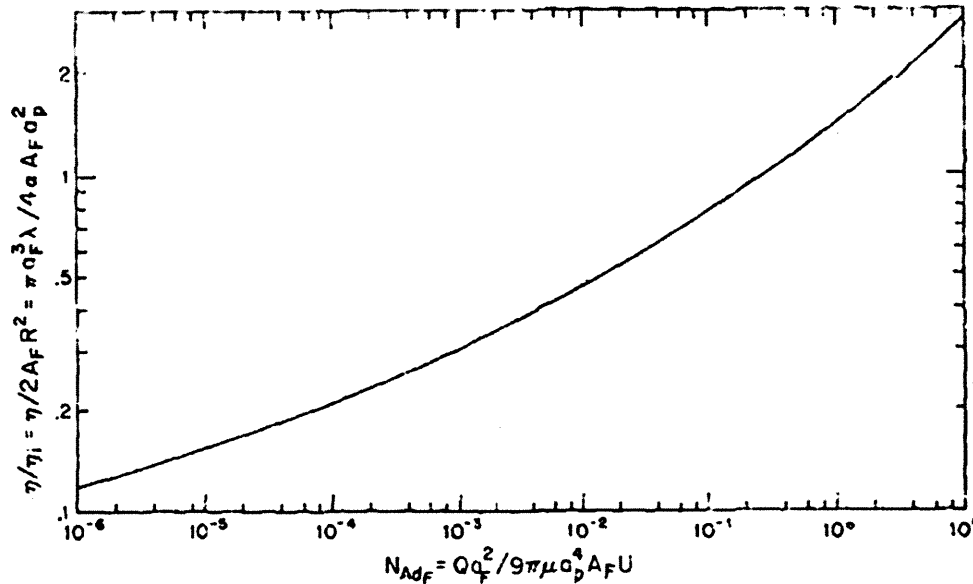
Fig. 5-5: Relationship between the modification factor for interception efficiency (η/η_i) and the adhesion coefficient (N_{Ad}) [13].

Several experimental studies have validated predictions from Goren's near surface model for solid cylindrical collectors [117, 119]. Schrijver [117] studied the deposition of latex particles onto a glass fiber collector 250μm in diameter. He found that the interception efficiency (which he assumed to be approximated by the deposition efficiency) is ill-predicted by the classical mechanisms alone. The addition of Goren's near surface model through the use of the adhesion coefficient resulted in very good agreement with experimental data. Chang's experiments [119] had similar findings. Chang also measured the effect on interception efficiency of using a nanoporous hollow fiber as a collector. He found that there is a far more dramatic increase in interception efficiency than can be explained by fluid displacement into the hollow fiber alone. He attributed this effect to the reduction in hydrodynamic resistance near the surface of the porous hollow fiber.

72

Based on an understanding of particle interception, we propose that there are two mechanisms in which a porous collector can improve interception efficiency compared to a solid collector. The first mechanism, shown in Figure 5-6(a), is the flow field modification that occurs as a result of fluid passage through the porous collector. This allows more fluid streamlines to come into contact with the collector, and increases the efficiency by direct interception. The second mechanism, shown in Figure 5-6(b), is the reduction of hydrodynamic resistance near the surface of the collector. We demonstrate these effects through a combination of numerical modeling and experimental validation in the following sections.
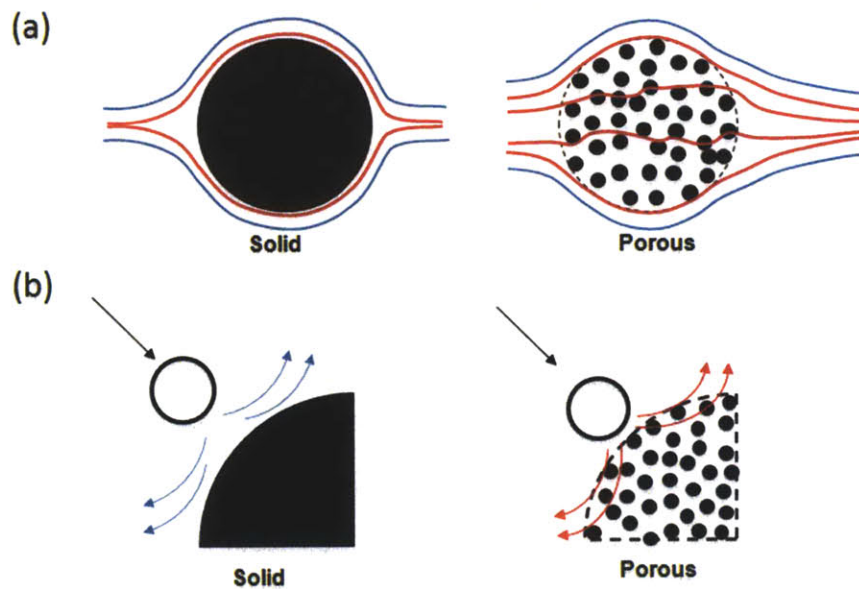
Fig. 5-6: Mechanisms for interception improvement with nanoporous elements (a) Schematic illustrating modifications to bulk flow streamlines by fluid passage through a porous element (b) Schematic illustrating the reduction of near-surface hydrodynamic resistance for a porous post compared to a solid post

5.3 Theoretical background on flow through porous media

The theoretical basis for porous media flow, including mixed porous and free media flow, has been well established in the last century. Several authors have also specifically addressed the scenario of low Reynolds number flow past a porous cylinder, both analytically [120, 121] and using numerical simulations [122, 123].

The constitutive equation for flow inside a porous material is given by Darcy's law, the general form of which is:

$$\nabla P = -\frac{\mu}{\kappa}\mathbf{v}$$ (5.7)

Where P is the pressure (Pa), μ is the dynamic viscosity (Pa.s), κ is the permeability (m^2), and $\mathbf{v}$ is the volume-averaged velocity vector (ms^{-1}). An alternative form of Darcy's equation is given by equation (3.1).

The dimensionless form of Darcy's law is given by:

$$\mathbf{v'} = -\frac{\kappa}{a^2}\nabla P'$$ (5.8)

Where $\mathbf{v'} = \mathbf{v}/U$ is the non-dimensional filter velocity, U is the far field uniform stream velocity, a is the characteristic length, and $P' = aP/\mu U$ is the non-dimensional mean pressure. The characteristic length is dependent on the geometry. In the case of a cylinder, it is the diameter. For other more complex geometries it can be more difficult to define.

From this form of Darcy's law we can define a dimensionless number known as the Darcy number, Da:

$$Da = \frac{\kappa}{a^2}$$ (5.9)

The Darcy number describes the fluid accessibility of a porous structure, relating this to its permeability κ and its characteristic length a. The higher the Darcy number, the more accessible a porous element is to fluid flow.

Darcy's law is derived from, and applicable for, flow regimes that are entirely inside of a porous media. In order to analyze problems containing a mixture of free media and porous media flow, Brinkman [124] proposed the addition of a second order viscous term to Darcy's original equation:

$$\nabla p = \mu_e \nabla^2 \mathbf{v} - \frac{\mu}{\kappa}\mathbf{v}$$ (5.10)

Where μ_e is known as the effective viscosity, given by:

74

$$\frac{\mu_e}{\mu} = \frac{1}{\varepsilon_{\mathrm{p}}} \qquad (5.11)$$

Where ε_p is the porosity of the porous medium. Brinkman's equation allows for matching of boundary conditions at the interface between porous and free media flow. In addition, both Darcy's and Brinkman's equations assume that the pores are isotropic, that the porous matrix is incompressible, and that the fluid flowing through them is incompressible.

When considering fluid flow in a mix of porous and free media, the assumptions made for conditions at the boundary of these regions are extremely important. First, the pressure at the boundary must be continuous. Second, conservation of mass dictates that the mass flux across the boundary must be continuous. In addition, the normal component of stress is also continuous. [120, 122, 125]. However, the no-slip condition that is valid for interfaces between a liquid and a solid surface does not apply for the interface between a liquid and a porous surface. In 1967, Beavers and Joseph proposed an empirical boundary condition for a flat planar boundary [126]:

$$\left(\frac{\partial u}{\partial y}\right)_{boundary} = \frac{\alpha}{\sqrt{\kappa}\left(u_b - Q\right)} \qquad (5.12)$$

Where u_b is the velocity at the boundary, and Q is the velocity inside the porous region. α is the empirically derived constant which ranged from 0.1 to 4 in the materials they tested. In 1973, Jones gave a generalization of this condition that is applicable to curved surfaces [127], stating that the difference of tangential components of fluid velocities and filter velocities is proportional to the shear stress at the surface.

More recently, Ochoa-Tapia and Whitaker [128] have suggested that the momentum transfer condition which applies at the boundary between a porous medium and homogenous fluid can be developed as a jump condition based on the nonlocal form of the volume averaged momentum equation. Outside the porous liquid interface, this nonlocal form reduces to Darcy law and Stokes equations. The jump condition is constructed to join Brinkman's equation to the Stokes equation, and results in producing a jump in the stress but not in the velocity. This stress jump condition proposed by Ocho-Tapia is given as:

$$\frac{1}{\varepsilon_p} \frac{\partial u^p}{\partial y} - \frac{\partial u^l}{\partial y} = \frac{\beta}{\sqrt{\kappa}} u^p \qquad (5.13)$$

Where u^p and u^l are the tangential velocities in the porous and liquid regions respectively, and β is a constant of order 1 and can be positive or negative.

The effect of the stress jump constant has been investigated by Partha [129] and Kuznetsov [130]. Both found a significant effect of varying the constant on the velocity field around a porous object, when the Darcy number is high (Da > 10^{-2}). However, Kuznetsov found that as Darcy number decreases to 10^{-2} or less, the effect of the stress jump coefficient became less significant.

The particular geometry of a porous cylindrical post inside a liquid flow field has been well investigated by several authors. All of them approached the problem by applying the Navier-Stokes equations for the free media region, and Darcy-Brinkman equations in the porous region. Although there were differences in how they approached shear stress boundary condition, all the analyses reached similar conclusions. In the 1970s, Verma [131] and Yamamoto [120] mathematically solved the equations to find the drag force on the post. Unsurprisingly, they found a decrease in drag with increasing permeability of the post. Armed with modern computing, Noymer [132], Bhattacharyya [123] and Yu [122] solved for the equations using numerical simulation. They were able to visualize the streamlines flowing inside and around the porous posts, and observed much greater streamline penetration inside the posts with increasing Darcy number. They also investigated turbulent conditions at higher Reynolds number, and found that contrary to the low Reynolds number scenario, drag of a porous cylinder increases beyond that of a solid cylinder in turbulent regimes. Despite not accounting for the stress jump coefficient, Noymer found good agreement between model predictions and experimental measurements.

5.4 Particle interception models for solid and porous posts

Based on the theoretical and experimental prior art in both particle interception and porous media flow described in 5.2 and 5.3, a model was developed in this work to analyze particle interception by solid and porous posts. This model is limited to incompressible flow at low Reynolds numbers (creeping flow, negligible inertial effects). The approach is to obtain streamline data from a 2D numerical model of the flow field using the commercial package COMSOL Multiphysics (v3.5a), and use this to calculate the direct interception efficiency. To this value near surface effects is adjusted for by using the adhesion coefficient (equation 5.6),

76

and then account for diffusion by adding on its contribution to interception efficiency (equation 5.4). For all models, water is used as the liquid medium, with a density of 1000kg/m^3, and a dynamic viscosity of 0.001Pa.s.

5.4.1 Model parameters for solid post interception

Streamlines for flow around a solid post is obtained by modeling incompressible flow using the 2-D Navier Stokes equations. Device geometries are replicated for the isolated post devices, and symmetrical boundary conditions are used for post arrays. The no-slip boundary condition is imposed at the surface of the post. Fluid velocity is set at 0.5mm/s, corresponding to that of experimental conditions. Direct interception efficiency is calculated by measuring the upstream distance between the streamlines that eventually pass exactly one particle radius away from the surface of the post on either side, and dividing by the post diameter (see Fig. 5.1).

For solid posts, it is assumed that the near-surface hydrodynamic resistance is significant, and adjust for this by calculating the adhesion coefficient N_{ad} and adjusting the direct interception efficiency according to figure 5-5. Actual values for flow parameters are used to calculate $N_{ad,}$ together with a Hamaker constant of $0.6 \times 10^{-20} \text{J}$, which is the value found by Visser [133] for a polystyrene particle-water-glass collector system. For small particles 2μm and below, we additionally account for diffusion using equation 5.4. The contribution from diffusion is added to the overall interception efficiency.

5.4.2 Model parameters for nanoporous post interception

The incompressible flow 2-D Navier-Stokes equations are used to model the free media flow region. The porous region is modeled using the Brinkman equation (built into COMSOL multiphysics' porous media flow module). A permeability of 10^{-13} m^2 and a porosity of 99% is used to define the porous subdomain, identical to the VACNT forest properties. For boundary conditions, we assume continuity in pressure, velocity, normal stress, and shear stress (i.e. a stress jump coefficient of zero). We assign a value of zero to the stress jump coefficient because we cannot measure its true value. However, since the effect of the stress jump coefficient is insignificant for lower Darcy numbers ($<10^{-2}$), which is our operating regime, we do not anticipate that this assumption will affect our model results. Direct interception efficiency is calculated as above.

For nanoporous posts, we assume that the near-surface hydrodynamic resistance is greatly reduced, such as to have insignificant effects on the interception efficiency. Thus no adjustment for this effect is made. The effect of diffusion is accounted for with particles 2μm and below in size, by applying equation 5.4 and adding its contribution to the overall interception efficiency.

5.4.3 Initial insights from model results

Comparison between porous and solid post streamlines: Figure 5-7 shows the model streamlines for a 200μm diameter solid post compared to those for a 200μm nanoporous post with permeability $1\text{x}10^{-13}$ m^2. We observe that, just like our experimental results shown in section 5.1, there is a tightening of the streamlines around the nanoporous posts, and that some streamlines pass through the inside of the post.
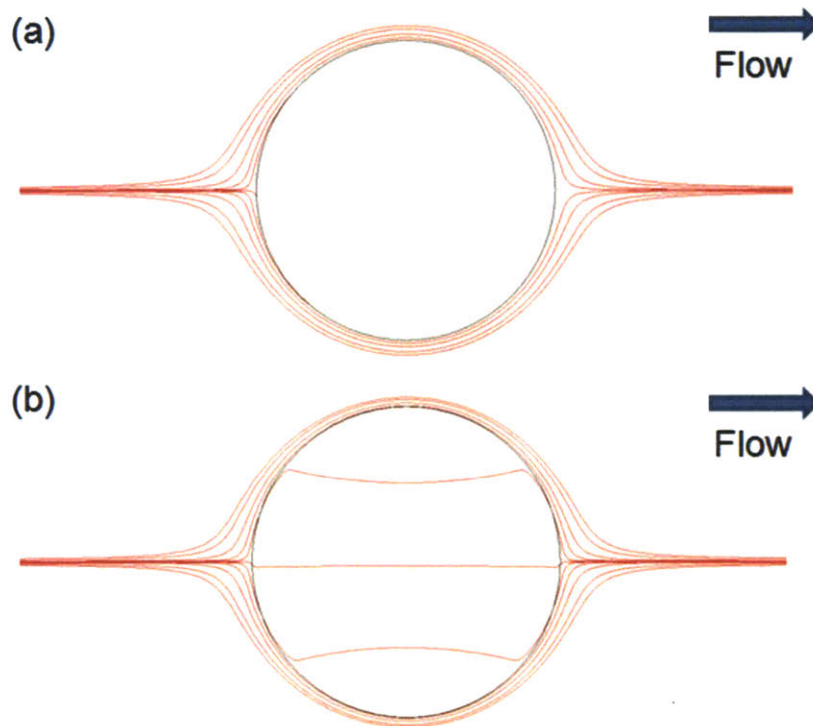
Fig. 5-7: Streamline comparison between solid and porous posts. (a) streamlines for a solid 200μm diameter post. (b) streamlines for a porous 200μm diameter post with permeability $1\text{x}10^{-13}$ m^2.

Darcy number equivalence: Previous models have shown that the degree of fluid accessibility inside a porous post is related to its Darcy number, defined as κ/d_c^2, where κ is the permeability of the porous material, and d_c is the characteristic length, or the post diameter. Since in our

experimental system the material permeability is constant, we must experimentally vary the Darcy number by changing the post dimensions. Figure 5-8 confirms that the same Darcy number obtained by changing the characteristic length does indeed equate to the same degree of fluid accessibility as that obtained by changing the material permeability.

1mm post, $\kappa=10^{-9}$m^2
Da = 0.004

100µm post, $\kappa=10^{-11}$m^2
Da = 0.004

10 µm post, $\kappa=10^{-13}$m^2
Da = 0.004
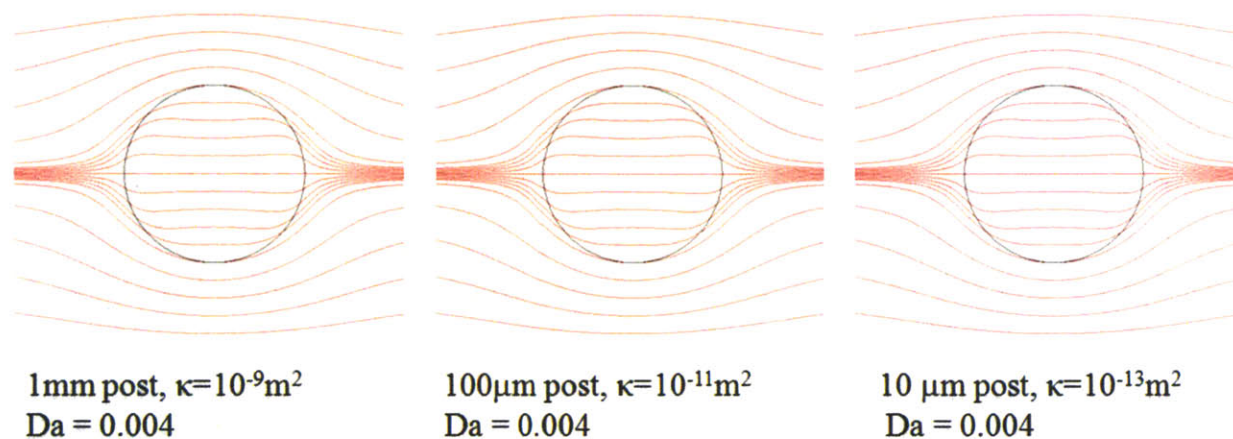
Fig. 5-8: The same Darcy number obtained by different combinations of permeability and characteristic lengths results in the same level of fluid accessibility (streamlines through porous post)

Darcy number vs. interception efficiency for porous posts: Figure 5-9 shows the streamline plots around and through porous posts with Darcy numbers of 10^{-7}, 10^{-5}, 10^{-3}, and 10^{-1} respectively. Figure 5-10 shows the computed interception efficiencies for Darcy numbers ranging from 10^{-7} to 10^0, and for different particle to post size ratios. For this model we did not include diffusion since the result is generalizable to different post sizes. We can see that the increase in interception efficiency with Darcy number is not linear. The curves can be divided into three regions: between Da = 10^{-7} and 10^{-4}, increases in Darcy number result in a small increase in interception; between Da = 10^{-4} and 10^{-2}, the incremental gain in interception efficiency becomes much greater; for Da > 10^{-2}, the interception efficiency asymptotically approaches 100%. In this range, the permeability is so high that there is very little deviation of streamlines from when there is no obstacle at all. As we will see in section 5.5, our experimental system has a Darcy number range that falls in the first region.

(a) Da = 10^{-7}

(b) Da = 10^{-5}

(c) Da = 10^{-3}

(d) Da = 10^{-1}
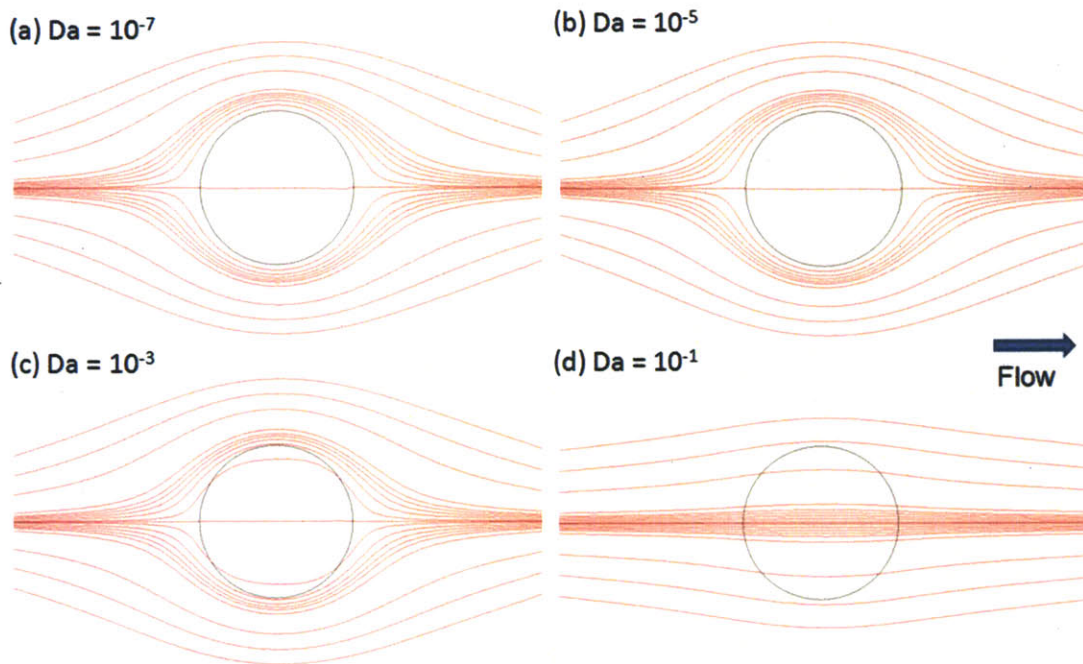
Flow

Fig. 5-9: Streamline plots for flow through and around porous posts of varying Darcy numbers.

$d_p/d_c = 0.1$
$d_p/d_c = 0.01$
$d_p/d_c = 0.001$
$d_p/d_c = 0$
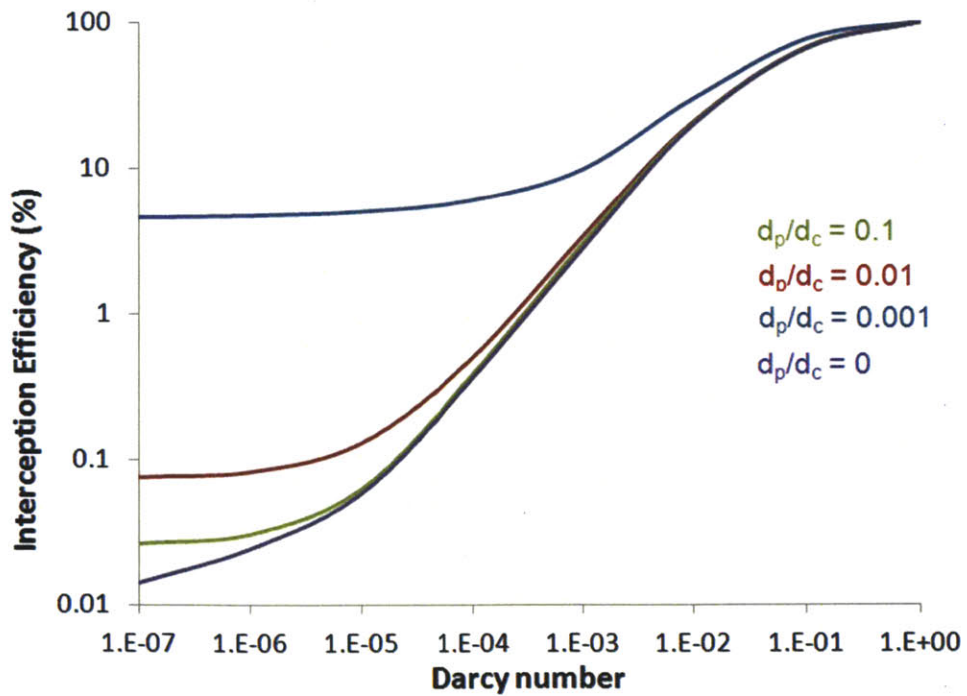
Fig. 5-10: Computed Darcy number vs. interception efficiency for nanoporous cylindrical posts.

80

5.5 Comparison of model and experimental results for particle interception by isolated posts

We investigate the interception efficiencies of single isolated nanoporous posts of varying Darcy numbers and compare them with the efficiency solid posts. We use the particle tracking from videos to experimentally determine interception efficiency by calculating $\eta = b/d_c$, as shown in figure 5-11. The isolated post devices are integrated into PDMS channels as described in section 3.7, and are treated with 0.5% Tween-20 in deionized (DI) water to block non-specific binding. The Darcy number is adjusted by changing the post diameter. Table 5.1 shows the experimental conditions used to vary Darcy number and particle-to-post diameter (d_p/d_c) ratios across different values. For solid post measurements, a post size of 200μm and bead sizes of 4μm, 10μm, and 20μm are used for d_p/d_c =0.02, 0.05 and 0.1 respectively. Channel side walls are positioned a minimum of 5 post diameters away to approximate a truly isolated post. Polystyrene particles (Duke Scientific) of the appropriate sizes are used to create the desired particle to post diameter ratio. The particles are suspended in a neutral density solution of DI water, Optiprep Density Gradient medium (Sigma Aldrich), and 0.1% Tween-20. Flow is introduced using a syringe pump (Harvard instruments) at 0.5 mm/s for all experiments. Videos of the flow around the posts are captured using an optical microscope and NIS Elements software. The videos are then analyzed using ImageJ particle tracking to determine the interception efficiency. A minimum of 20 intercepting particles are analyzed per device, and the results from 4 devices are averaged per data point.
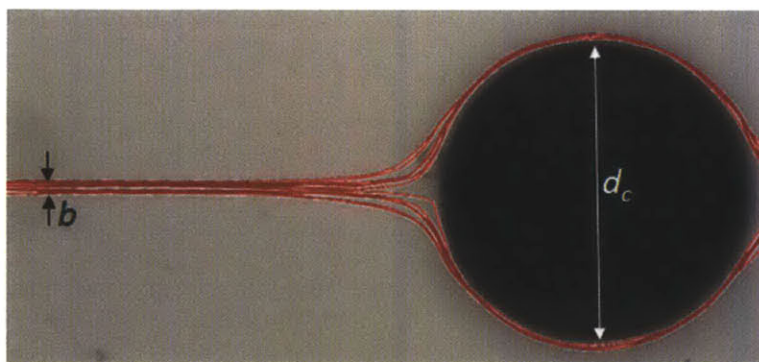
Fig. 5-11: Particle tracks from videos of particle flow around a nanoporous VACNT post. Interception efficiency is calculated by $\eta = b/d_c$.

Table 5.1: Darcy number, post size and particle size of nanoporous posts tested in experiment.

Da	d_c (µm)	d_p (µm) ($d_p/d_c = 0.02$)	d_p (µm) ($d_p/d_c = 0.05$)	d_p (µm) ($d_p/d_c = 0.1$)
1×10^{-7}	1000	20	50	100
4×10^{-7}	500	10	25	50
2.5×10^{-6}	200	4	10	20
1×10^{-5}	100	2	5	10
4×10^{-5}	50	1	2.5	5

Figure 5-12 compares the measured values of interception efficiencies for solid and nanoporous posts with our model predictions. Looking at the results for the nanoporous posts, we see that the experimental measurements match very closely with the theoretical predictions for all three d_p/d_c ratios. Recall that the predictions for the porous posts are based only on direct interception and diffusion (predictions without contribution from diffusion are shown in Fig. 5-13b). The results seem to support our initial hypothesis that the effects of near-surface hydrodynamic resistance is greatly reduced by the porous element surfaces. The second observation we make is that as we increase the Darcy number, interception efficiency increases non-linearly. The highest Darcy number tested in our experiments is 4×10^{-4}, corresponding to a post size of 50µm at our material permeability of 1×10^{-13} m^2. This was the smallest post size at which our method can reliably measure interception efficiencies. However, our theory predicts that if we can increase the Darcy number further, we can greatly improve the interception efficiency through the mechanism of direct interception. Since $Da = \kappa/d_c^2$, we can increase Da by either increasing the material permeability or decreasing the post dimensions. We have previously explored methods to vary material permeability by changing growth parameters for the CNTs (section 3.6). For post dimensions, we are able to reliably grow high aspect ratio (up to 100) nanoporous posts down to 10µm in diameter. Smaller post sizes are possible at lower aspect ratios.
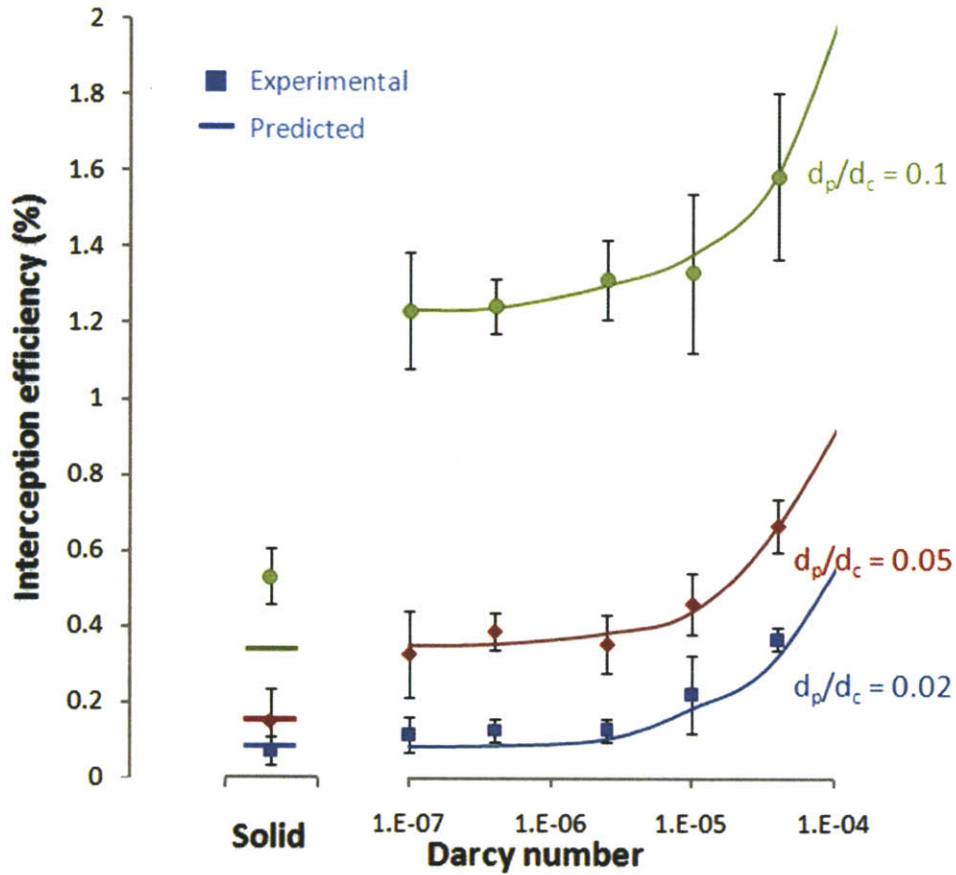
Fig. 5-12: Experimental and predicted interception efficiencies for isolated solid posts and nanoporous posts of varying Darcy number, at three different particle to post size ratios, accounting for direct interception, near-surface effects, and diffusion. Error bars represent one standard deviation.

Turning to the results for isolated solid posts, we see again that experiment matches predictions relatively closely. The theoretical predictions for solid posts include the effects of near-surface hydrodynamic resistance as well as direct interception and diffusion. If hydrodynamic resistance had not been accounted for, the predictions from streamlines alone would show little difference in interception between the solid posts and the lowest Darcy number porous posts (Fig. 5-13a). Instead, we see both from theory and experiments that hydrodynamic resistance greatly reduces interception efficiencies for solid posts compared to even the low Darcy number porous posts. In addition, the effect is more significant for larger d_p/d_c ratios. This is because at small d_p/d_c ratios, the London force begins to have influence on the interception efficiency and cancels out some of the effects of hydrodynamic resistance. We also see that the prediction for $d_p/d_c = 0.1$ does not

match the experimental result as well as the other data points. This may be because the near-surface model developed by Spielman and Goren makes the assumption that $d_p \ll d_c$, which begins to break down at higher d_p/d_c ratios.
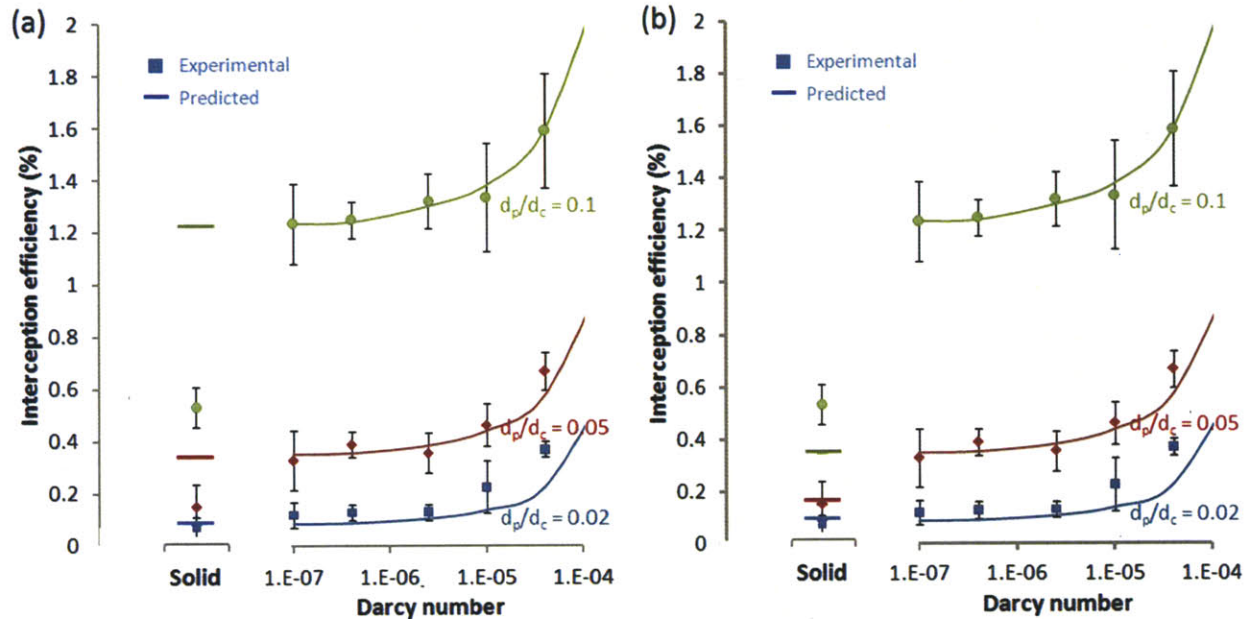
Fig. 5-13: (a) Model with direct interception only compared with experimental results. Without taking into account of near-surface effects, the model gives poor predictions for solid posts but relatively accurate predictions for porous posts. (b) Model with direct interception and near-surface effects only (no diffusion) compared with experimental results. The model under-predicts interception efficiencies for the high Darcy number, low d_p/d_c results, which uses 1 μm and 2 μm particles.

5.6 Comparison of model and experimental results for particle interception by post arrays

In real world device applications, posts are rarely used in isolation, far away from walls and neighboring elements. Post arrays are far more commonly used in bioparticle separation devices. We investigate the effect of the proximity of neighboring posts on the interception efficiencies of individual posts within the array, and compare experimental results with model predictions.
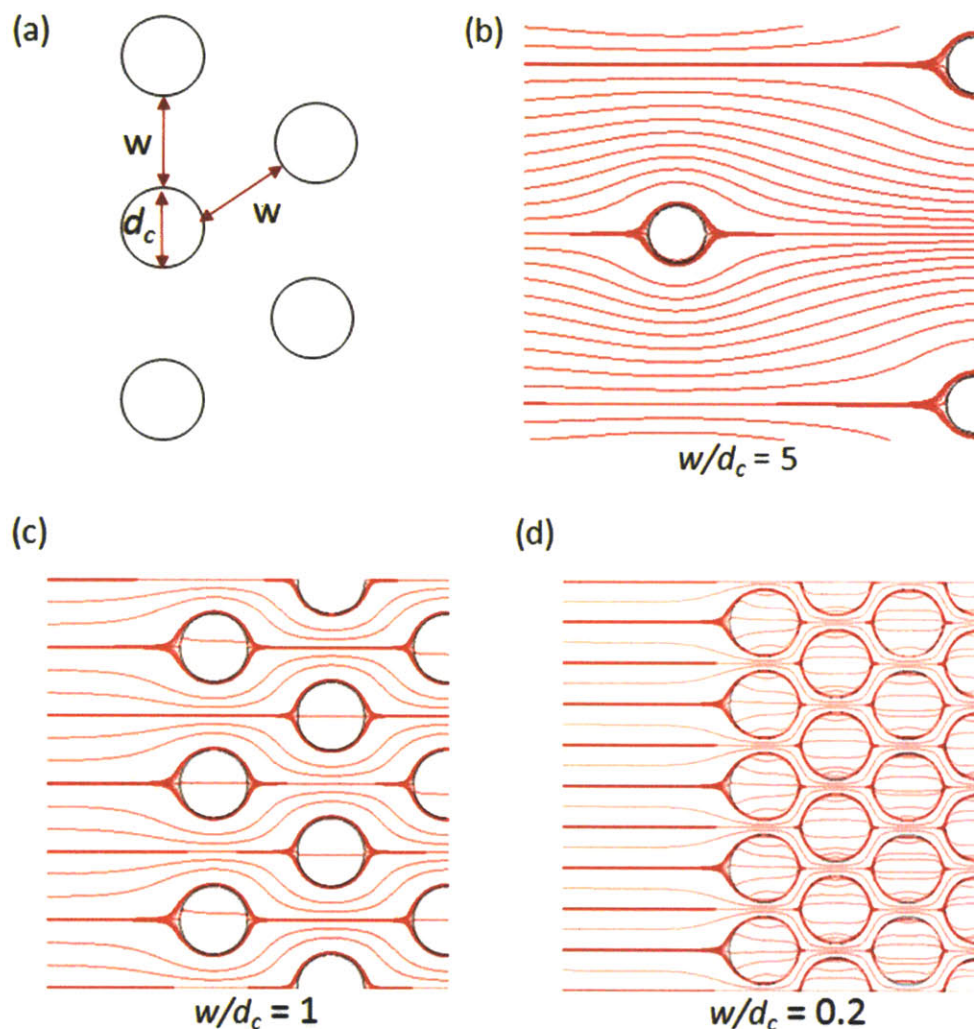
Fig. 5-14: Model streamlines for nanoporous post arrays of different spacings. (a) Schematic of array configuration. w = gap between posts, d_c = post diameter. (b) Model streamlines for w/d_c = 5, showing very little flow penetration inside the nanoporous posts. (c) Model streamlines for w/d_c = 1. Some flow penetration inside the posts. (d) Model streamlines for w/d_c = 0.2. Significantly more flow penetration inside posts than for the sparser spacings.

The nanoporous post arrays are integrated into PDMS channels as described in section 3.7, and are treated with 0.5% Tween-20 in deionized (DI) water to block non-specific binding. PDMS post array devices are fabricated as in section 3.8 for comparison. All posts are 100µm in diameter, 80µm in height, and are arranged in a hexagonal packing configuration (Fig. 5-14a). The distance between neighboring posts are varied from 20µm (w/d_c = 0.2) to 500µm (w/d_c = 5). 2µm and 10µm polystyrene particles (Duke Scientific) are used to create particle to post diameter ratios of 0.02 and 0.1 respectively. The particles are suspended in a neutral density solution of DI

water, Optiprep Density Gradient medium (Sigma Aldrich), and 0.1% Tween-20. Flow is introduced using a syringe pump (Harvard instruments) at 0.5 mm/s for all experiments. Video capture and particle trajectory analyses are performed as in section 5.5. Interception efficiency is determined in each device for a post positioned in the center of the front row in the array.
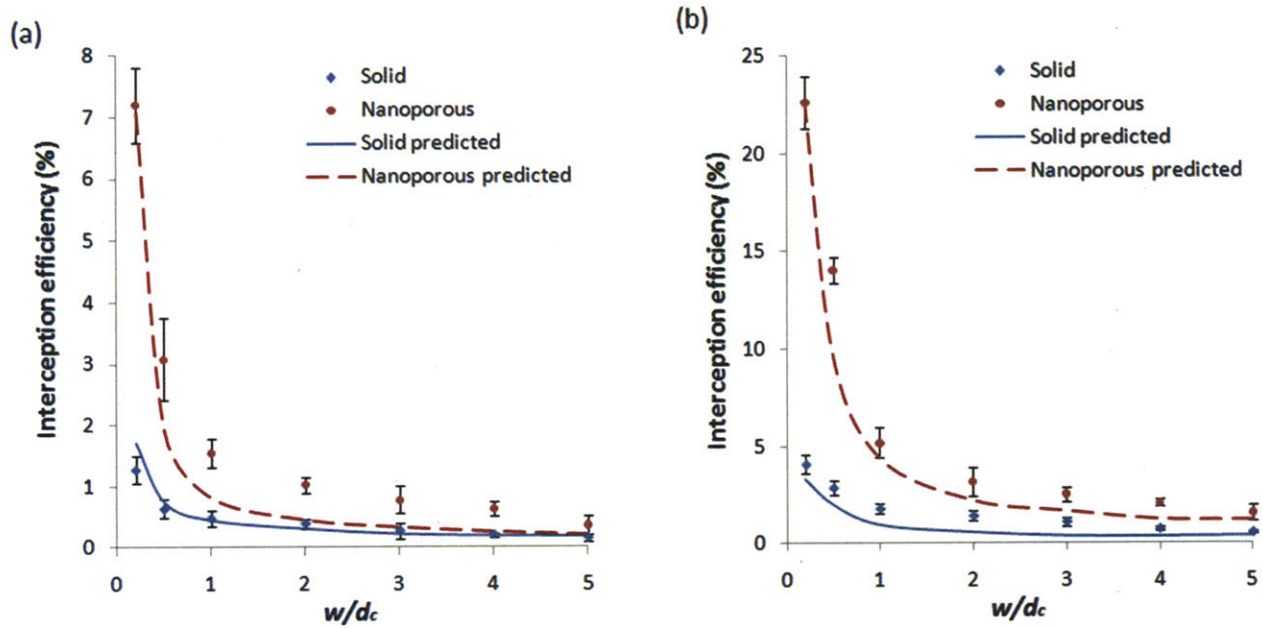
Fig. 5-15: Predicted and measured results for interception efficiencies of post arrays (a) Predicted and measured interception efficiencies for different array spacings, with $d_p/d_c = 0.02$. (b) Predicted and measured interception efficiencies for different array spacings, with $d_p/d_c = 0.1$

The modeling shown in figure 5-14 investigates the effect of arraying on the interception efficiencies of individual posts. To isolate the effect of array density, all arrays are configured to a hexagonal packing geometry, and all post sizes are kept at 100μm, corresponding to a Darcy number of 10^{-5}. Array density is defined by the parameter w/d_c, where w is the distance between the edges of neighboring posts, and d_c is the post diameter. The model shows that as w/d_c decreases, the neighboring posts act to squeeze more streamlines inside the nanoporous posts, and this effect increases the interception efficiency of individual posts in the array. For solid posts, although streamlines are also squeezed tighter together, they cannot penetrate inside the posts.

Figures 5-15(a) and 5-15(b) compare experimental and theoretical results for interception efficiency as w/d_c varies for both solid and nanoporous posts. We see that although closer array

spacing improves interception for both solid and nanoporous posts, the efficiency increase for nanoporous posts is much more dramatic. For both d_p/d_c values, the ratio of interception efficiencies of nanoporous posts to solid posts increase from ~2 fold at $w/d_c = 5$ to ~6 fold at $w/d_c = 0.2$. We see that the experimental results match model values relatively well, although there is a trend for under-prediction.

5.7 Capture of biological particles by post arrays

We are interested to see if the improvements in interception efficiency for nanoporous post arrays compared to solid post arrays translate to similar improvements in capture efficiency. The same post configurations (100μm diameter, hexagonal packing) of both VACNT and PDMS devices are used as in the experiments for section 5.6. This time, instead of blocking the devices with Tween-20, they are functionalized with the appropriate antibodies for specific cell capture. In the experiments shown in figure 5-16, fluorescent heat killed Escherichia coli bacteria (Invitrogen) at 5×10^6 particles per milliliter in PBS are used as the model sample, and the devices are functionalized with biotinylated anti-*e. coli* (rabbit polyclonal, Abcam). In the experiments shown in figure 5-17, Calcein-stained PC3 cancer cells (ATCC) at 2×10^5 in PBS are used as the model sample, and the devices are functionalized with biotinylated anti-EPCAM (goat polyclonal). The samples are injected into the devices using a syringe pump, at 0.5 mm/s, for 4 minutes. After the capture stage, the devices are rinsed in PBS at 0.5 mm/s for 2 minutes. The devices are scanned under fluorescent microscopy and the capture analyzed using ImageJ. The capture of the first row in the array is used to calculate the per row capture efficiency.

Figure 5-16(a) shows capture of *Escherichia. Coli* particles in buffer, comparing capture values between solid and nanoporous post arrays at two different array spacings. *Escherichia. Coli* are rod shaped bacteria with a length of ~2μm, corresponding to a $d_p/d_c = 0.02$. We see a ~6 fold capture improvement at $w/d_c = 0.2$ and a ~2 fold capture improvement at w/dc=2, very close to the observed improvement in interception for the same d_p/d_c ratio. Figure 5-17(a) shows capture of PC3 cancer cell line in buffer, again comparing between solid and nanoporous post arrays at two different array spacings. PC3 cells are between 10 and 20μm in size, roughly corresponding to a $d_p/d_c =0.1$ with our posts. We see a ~4 fold capture improvement at $w/d_c = 0.5$ (we did not use w/dc =0.2 because the largest cells could bridge the gap and be physically trapped) and a
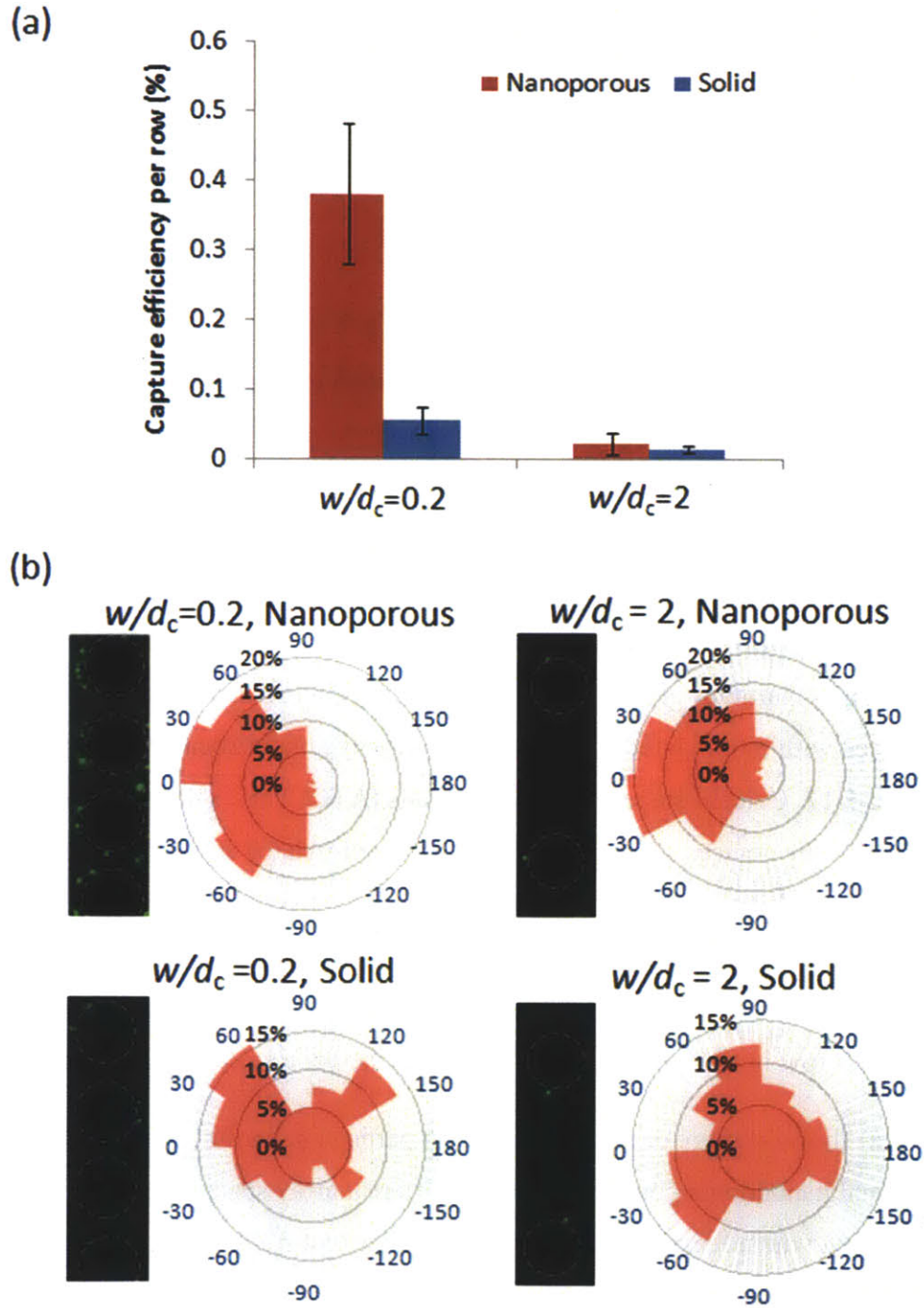
Fig. 5-16: Capture of *E. coli* cells on post arrays at different spacings. (a) Capture efficiency per row of each array of nanoporous and solid posts. (b) Fluorescent images and angular capture locations of e. coli cells on nanoporous and solid post arrays with 20µm and 200µm gap. Post outlines are traced in dotted lines. Flow direction from left to right. Angular capture locations are plotted as percentage of cells captured in 30° segments.
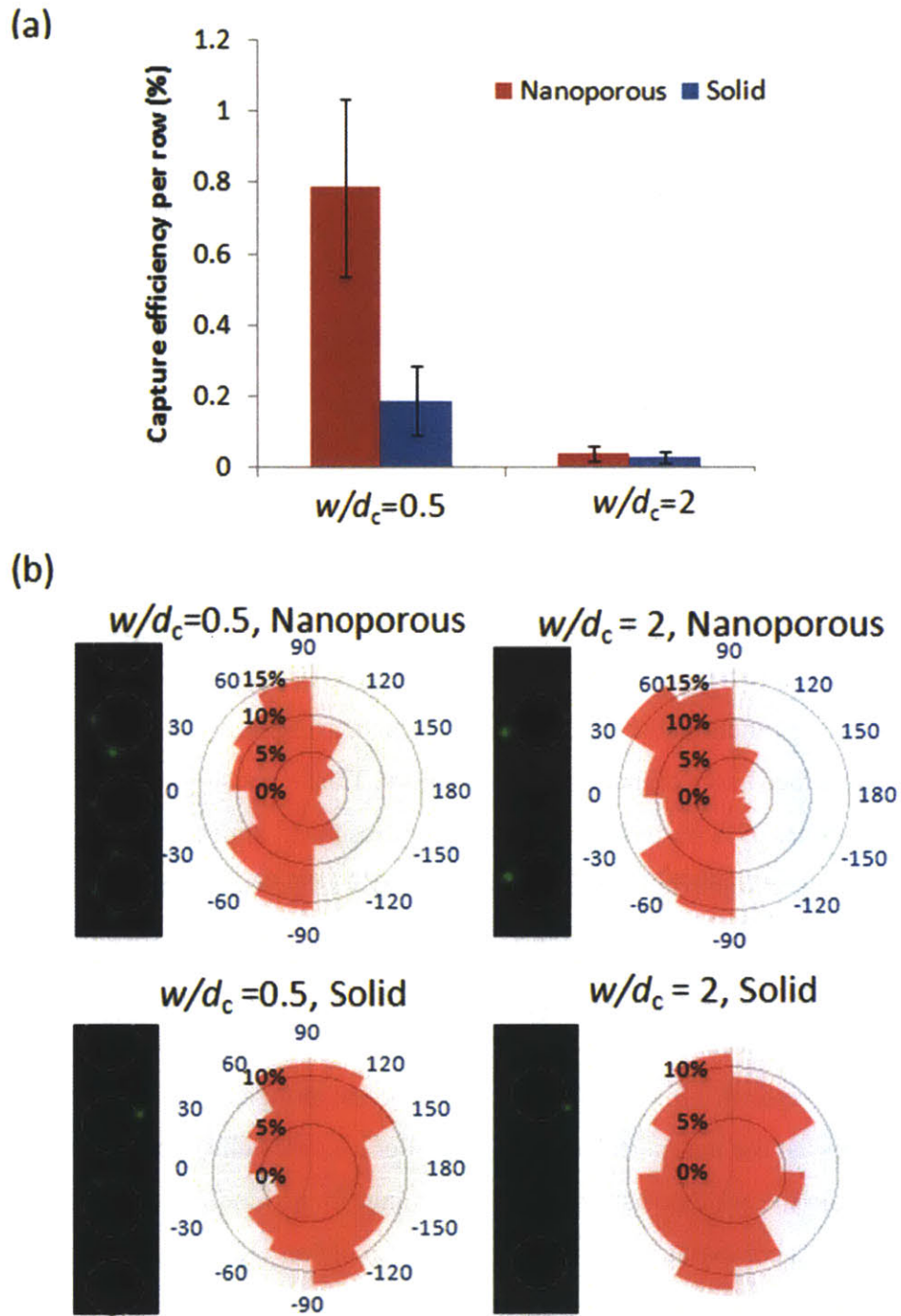
Fig. 5-17: Capture of PC3 cancer cells on post arrays at different spacings. (a) Capture efficiency per row of each array of nanoporous and solid posts. (b) Fluorescent images and angular capture locations of PC3 cancer cells on nanoporous and solid post arrays with 50μm and 200μm gap. Post outlines are traced in dotted lines. Flow direction from left to right. Angular capture locations are plotted as percentage of cells captured in 30° segments.

~1.5 fold capture improvement at $w/d_c = 2$. These values are slightly lower than the 5 fold and 2 fold interception improvements seen at these spacings for $w/d_c = 0.1$.

The rose plots in Figure 5-16(b) and 5-17(b) show that for nanoporous posts, the majority of the capture occur on the front surface of the posts, whilst for solid posts capture occur on both front and back surfaces. This is because fluid flow enters porous posts on the front surface and exits through the back, such that particles at the back surface are likely to by pushed off. With solid posts, particles are able to roll along the post surface and be captured at any location. This data suggests that it may be possible to create geometries for nanoporous post arrays using non-circular posts such that the non-capturing back surface is eliminated to give higher capture efficiency per footprint area.

As already noted, capture efficiency is a function of both the interception efficiency and the binding efficiency between the particle and the functionalized surface. Section 3.7 qualitatively compared the level of receptor density on the surface of VACNT posts versus PDMS posts, based on our current functionalization methods for each, using fluorescent proteins, and showed that the PDMS surface had a higher level of receptors. This is not surprising as the surfaces of the VACNT posts are 99% porous. From our capture results, it appears that for bacteria cells, this difference in functionalization does not significantly affect capture results when comparing nanoporous with solid posts, and that the same order of improvement is seen in capture as in interception. However, for large mammalian cancer cells, the relative size of the capture improvement of nanoporous posts over solid posts is slightly reduced compared to the interception improvement. This is most likely because the larger cancer cells experience a much greater shear stress at the post surface than the smaller bacteria cells, such that the higher receptor density on the solid posts provide an advantage in the binding efficiency, which somewhat offsets its comparative disadvantage in interception efficiency. Despite this effect, there is still a dramatic improvement in capture observed for both cell types. It can also be noted from the rose plots that the locations of cancer cell capture is more clustered around the top and bottom surfaces of the posts (close to $\pm 90°$) compared to locations of bacteria cell capture, which are more concentrated at the very front edge of the post (between $\pm 30°$). This suggests that more rolling is needed for capture of the larger cancer cells.

This chapter studied the interception efficiencies of particles in solution by cylindrical posts in microfluidic channels, through both theoretical analysis and experimental studies. Solid posts fabricated using standard soft lithography was compared with nanoporous posts fabricated using ultra-high porosity carbon nanotube forests. It was shown that nanoporous posts significantly improve particle interception through two mechanisms: first, fluid streamlines passing through the porous post bring particles that traverse along them directly to the post surface; second, the highly porous post surface reduces hydrodynamic resistance that prevents particles from contacting solid surfaces. The interception efficiency can be further enhanced by increasing the Darcy number of individual nanoporous posts or increasing the packing density of post arrays. Furthermore, it was shown that although arraying helps to increase interception with both solid and nanoporous posts, it gives a much bigger advantage to the nanoporous posts. Experimental studies using both bacteria and cancer cells demonstrated that the increase in interception efficiency also results in improved capture efficiency under idealized conditions.

Chapter 6

Conclusions and outlook

This thesis introduced vertically aligned carbon nanotubes (VACNTs) as a novel porous material for microfluidics, and applied it to the separation of bioparticles. Microfluidic integration of patterned VACNT forests was achieved using two different methods, and the forests were shown to maintain their structure after wetting, functionalization, and flow. It was shown both experimentally and analytically that the ultra-high (99%) porosity of the VACNT forests led to a much higher permeability than other porous materials of comparable pore size. There was demonstration of both mechanical and chemical capture of particles ranging over three orders of magnitude in size. Nanoparticles below the inter-nanotube spacing (80 nm) of the forest can penetrate inside the forest and interact with the large surface area created by individual nanotubes. For larger particles (>80 nm), the ultra-high porosity of the nanotube elements enhances particle-structure interactions on the outer surface of the patterned nanoporous elements. Specific biomolecular recognition using cells (~10 μm), bacteria (~1 μm), and viral-sized particles (~40 nm) using both effects was demonstrated. In addition, this work showcased the possibility of simultaneous multi-scale, multiphysics separation of three particles ranging from 40nm to 15μm in size on a single porous array device.

It was shown using both modelling and experiment that nanoporous posts improve particle interception compared to solid posts through two mechanisms: the increase of direct interception and the reduction of near-surface hydrodynamic resistance. Using both bacteria and cells as model systems, it was verified that the improvement of interception efficiency also results in an increase in capture efficiency when comparing nanoporous VACNT post arrays with solid PDMS post arrays of the same geometry. The technology developed in this thesis can provide unprecedented control of bioseparation processes to access any bioparticle of interest, opening new pathways for both research and point-of-care diagnostics.

6.1 Summary of Contributions

Two techniques for the microfluidic integration of nanoporous VACNT elements were developed. Both methods use standard photolithography of an iron catalyst layer and chemical vapor deposition (CVD) to grow 99% porous VACNT forests. The first method combines this with standard soft lithography of PDMS channels and O_2 plasma bonding to create the nanoporous microdevices. This results in nanoporous elements that are well sealed with the top of the channel, but good side sealing is difficult. A second method we developed patterns both the nanoporous features and the microchannel walls from VACNTs. The channel walls are subsequently made less permeable by polymer infiltration. The channel is then sealed on top using a flat PDMS slab, using uncured PDMS as an adhesive. This method provides both top and side sealing, and is more suitable for filtering applications. Both methods enable precise patterning of the nanoporous microfluidic elements independent of channel boundaries, with the elements' in-plane layout defined using lithography while the out-of-plane geometry (height) is tailored through control of the CNT growth conditions. This allows for a flexibility of design that is not possible using current porous materials.

The fluidic properties of VACNT forests were investigated and compared to state-of-theart porous microfluidic platforms. Permeability levels comparable to or higher than that of other micro-/nano-scale materials were experimentally demonstrated for the VACNT forests ($\kappa = 5.4*10^{-14}$ m^2). An analytical discussion on the effect of porosity on the permeability of porous materials was used to explain the significant decrease/increase of permeability of microfluidic elements when designing in the very small and very large structural porosity regions. The ability to manipulate the permeability of VACNT forests through control of both material and CNT growth parameters was experimentally demonstrated as well, yielding ~100% enhancement in permeability for the nanoporous elements demonstrated here.

Both mechanical filtration and chemical isolation of particles over 3 orders of magnitude in size was experimentally demonstrated, from mammalian cells ~10-20μm in diameter, to viral sized particles 40nm in diameter. For microparticles larger than the inter-nanotube spacing (80nm) of the forest, we observe an enhancement in interception efficiency due to the flow field modification by fluid flow through the forest. For nanoparticles smaller than the inter-nanotube spacing, VACNT designs result in a significant enhancement in the active surface area for

capture (~200-400x for some geometrical layouts considered in this work). Simultaneous isolation of three distinct particle types (15μm non-functionalized, 2μm avidin coated, and 40nm avidin coated polystyrene particles) using a single device was also demonstrated, combining mechanical filtration and chemical biomolecular recognition to enable bioparticle capture both on the external and on the internal surfaces of the nanoporous VACNT elements.

The popularly used, and simple to model geometry of a cylindrical post was chosen to gain a deeper understanding of particle interception through theory and experiment. Different factors that affect interception efficiency in the flow regime of a typical microfluidic system (low Reynolds number) were examined, along with mechanisms that limit interception in solid elements. Theoretical understanding of interception was combined with a numerical model of mixed porous and free media flow to form a model for particle interception for solid and porous cylindrical posts. This model was put to the test against experimental results for particle interception using both isolated posts and post arrays. In each case, there was good agreement of theory and experiment to prove that we can greatly improve interception efficiency by using nanoporous posts instead of solid posts of the same geometry. It was shown that this improvement is due to two mechanisms: first, fluid streamlines passing through the porous post bring particles that traverse along them directly to the post surface; second, the highly porous post surface greatly reduces hydrodynamic resistance that prevents particles from contacting solid surfaces. The interception efficiency can be further enhanced by increasing the Darcy number of individual nanoporous posts or increasing the packing density of post arrays. Using both bacteria and cancer cells as model systems, it was verified that the improvement of interception efficiency also resulted in an increase in capture efficiency when comparing nanoporous VACNT post arrays with solid PDMS post arrays of the same geometry. The combined model and experimental platform presents the toolset for a new generation of porous microfluidic devices for high efficiency, low footprint area bioparticle capture for research and biomedical diagnostics.

6.2 Recommendations for future work

Although the model created in this work produced good correlation with experimental results for the isolated post experiments, and reasonable agreement for the post array experiments, it

could be further refined. Currently the numerical model only calculates fluid streamlines, and the effects of diffusion and near surface forces are added on. To allow more flexibility of the model for arbitrary geometries, the considerations for deviations of particles from streamlines should be built in to the numerical model. In addition, cells can be highly deformable, which could play a significant role to their flow trajectory near surfaces. This should be accounted for in the model.

As previously discussed, particle isolation efficiency is a function of both the interception efficiency and the binding efficiency. So far our model only takes into account interception efficiency. For a complete model of particle isolation in porous and solid microfluidic systems, the binding efficiency must also be included. Parameters would include the density of binding sites on the microfluidic elements, the density of ligands on the bioparticle, and the binding kinetics between them.

With a refined model we will be able to make designs to optimize both interception and binding efficiencies. An important goal would be to select a real world application (e.g. bacteria capture from processed sputum) to optimize for. Using the model, it will be possible to quickly test out multiple designs *in silico*, before selecting several of the most efficient designs to build and test in experiment. There will be a need to optimize for high efficiency, high throughput, and low footprint area. The experimental testing will begin with spiked particles in buffer, and proceed to real clinical samples.

It can be seen from figure 5-11 that currently, it is possible to achieve Darcy numbers in the range between 10^{-7} and 10^{-4}. However, figure 5-9 shows that at this low range of Darcy numbers, large changes in Da produce relatively small changes in interception efficiency. If the Darcy numbers achievable by the VACNT elements can be shifted to the 10^{-5} to 10^{-2} range, it will not only be possible to have much higher interception efficiencies, but interception efficiency can be more easily manipulated through changes in device geometry (see also Appendix A). To create this shift in Darcy number range, the material permeability of the VACNT forest must be increased. Since the porosity of the current VACNT forest is already very high, the main method for increasing permeability would be to increase the inter-nanotube spacing (corresponding to the pore size). Having larger pore size forests would also allow the internal capture of a greater range of bio-nanoparticles including viruses and exosomes. For example, the HIV-1 virus is between 90nm and 150nm in diameter, which is larger than our current forest spacing. If the

spacing can be increased to 200nm or more, it will be possible to capture the viruses inside the forest for applications in HIV viral load monitoring.

The possibility to tailor the permeability of VACNT elements by controlling both material (catalyst thickness) and CNT growth process (pre-treatment time) parameters was demonstrated in Section 3.6. However, the methods presented in this work allow control solely over the average properties of VACNT elements, and they do not enable large modifications in forest morphology (e.g., modification of intra-element spacing using our approach is limited to approximately ±10 μm) or the resulting permeability. Using innovations in nanolithography, for example interference lithography [134], it should be possible to create larger inter-nanotube spacings, and with much more consistent pore sizes. This would improve the utility of the VACNT forests for filtration applications, allow for the internal capture of larger viruses, as well as greatly increasing the permeability of the forests.

For many applications, it is desirable to be able to release the desired bioparticles from the capture surface after isolation, either for downstream culturing or for further counting and sorting. Carbon nanotubes are known to be highly efficient at absorbing radiation in the microwave range and releasing the energy as heat [84]. Several groups have used this property together with the ability to functionalize CNTs to perform tumor targeting and heat-mediated destruction [83]. This property can be taken advantage of to enable thermal release of captured bioparticles by making use of a thermoresponsive linker molecule, such as DNA strands. The linker would be bound to the CNT surface at one end, and functionalized with antibodies (or other binding moieties for the bioparticle of interest) at the other end. It would be designed to break at a desired release temperature, above room temperature and below a temperature that would cause damage to the bioparticles. The dose and optimal frequency of the microwave source would need to be carefully calibrated to the system.

As discussed in section 2.5, carbon nanotubes have unique electrical and other properties that have enabled their application in biosensing. A goal of future research would be to integrate these sensing techniques with our high efficiency capture methods. This would eliminate the need for optical readout of capture results and enable new families of low cost, lab-on-a-chip devices for point-of-care diagnostics applications.

This thesis introduced nanoporous CNT elements as a new structural element within microfluidics and demonstrated some key advantages that this technology enables for bioparticle separation. In contrast to previously described microfluidic platforms for particle isolation, which are highly tailored to perform optimally for particles of a single size, the nanoporous elements provide a more universal platform, capable of high efficiency separation of bioparticles across multiple size scales, ranging from viruses to bacteria and cells. Furthermore, the fabrication process is simple with a fast turnaround for prototyping. For separation of nanoscale particles that can enter inside the porous VACNT forest , the ultra-high porosity and permeability of the forest allows for high throughput sample flow, and large surface area for interaction. For separation of microscale particles that cannot enter inside the porous forest, there is also an advantage in capture, compared to solid counterparts, through mechanisms of increased interception efficiency. With further refinement of the technology and testing using clinical samples, this platform has the potential to create new families of devices for a very broad range of applications, including lab-on-a-chip devices for blood analysis to monitor patients at the point-of-care, ultra-rapid cell sorters to detect rare cells in circulation for diagnostics (e.g. cancer, prenatal, infections), high-throughput filters for pathogen depletion, and isolation of bacteria and viruses for diagnosing infectious diseases.

Appendix A

Effect of porous filter on channel flow profile

It is important to understand how the flow profile across a microfluidic channel changes between free media flow in an open channel and porous media flow through a nanoporous filter. This was simulated using COMSOL multiphysics, using parameters as described in section 5.4.2, except that the geometry used was of a porous barrier spanning across the whole channel instead of porous posts. Input velocity was set to 1mm/s. It is interesting to observe that in the free media region of an open channel, the fluid flow follows the classic Poisseuille flow profile. However, the flow inside the porous region is much more uniform across the width of the channel, with only a thin stagnant layer very close to the channel sides.
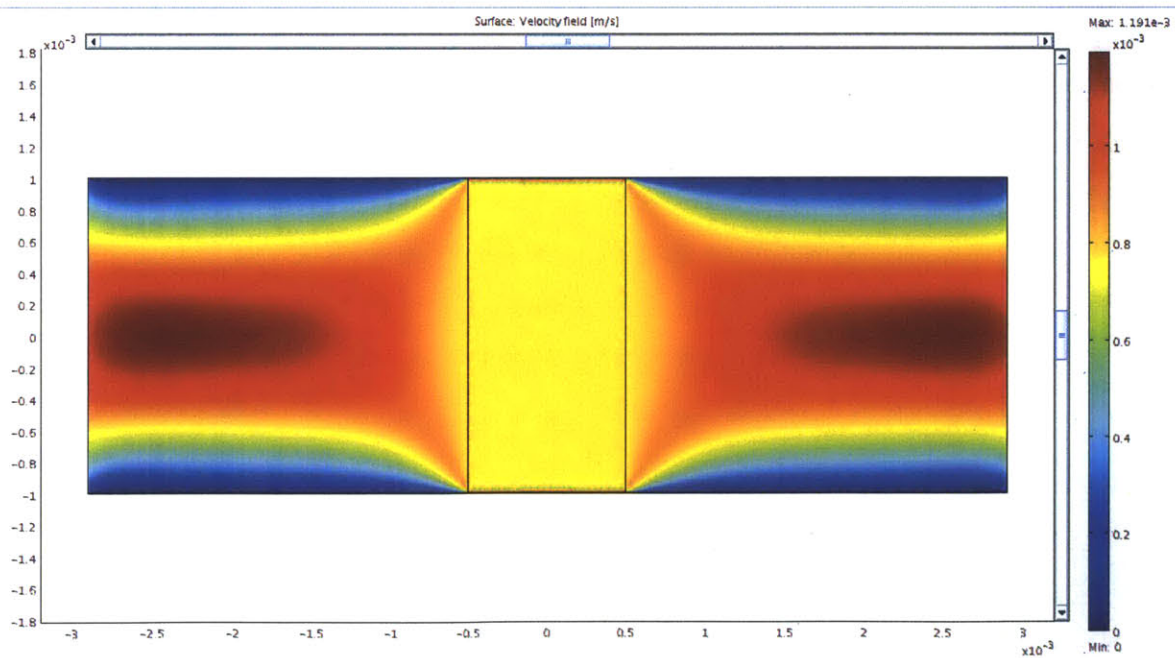
Fig. A-1: Velocity map from simulated flow as it passes from an open channel to a rectangular porous filter, and back to an open channel.

Appendix B

Effect of element geometry on interception efficiency of nanoporous posts

The majority of the work in this thesis focused on the simple geometrical configuration of circular posts. This was chosen in order to develop and refine the understanding of particle interception and porous media flow using a simple model system, for which analytical solutions have been found for solid post flow systems. However, some preliminary work was performed to explore the effect of changing the post geometry on particle interception.

This work focused on geometries to improve interception efficiency for a set post width, whilst also keeping in mind that the designs need to maximize cell-surface contact time and allow for some rolling to occur. Figure A-2(a) show pictures of the device designs we tested, which combined two strategies for interception improvement. The first is to reduce the 'characteristic length' of the nanoporous element by making it hollow. This keeps the same footprint area, and interception width, whilst increasing the overall Darcy number of the element. In fact, Singh and Gupta [135] had found that for a porous cylinder with a circular cavity inside, the effect on drag is identical to that of a uniform porous cylinder with the permeability modified by:

$$\kappa' = \kappa \frac{b^2 + 2ab + 2a^2}{b^2 + 2ab} \tag{A.1}$$

where κ is the permeability of the porous material, a is the radius of the cavity, and $a+b$ is the radius of the overall cylinder. The second strategy uses an airfoil geometry to reduce the form drag of the element, so that the streamlines would wrap more tightly around it, increasing interception efficiency.

The nanoporous elements are patterned and bonded inside PDMS channels using the methods described in sections 3.1 and 3.2.1. All geometries were 1mm wide in footprint (d = 1mm) and 100μm high. The hollow elements had a shell thickness of 50μm. The channel was 2mm (W) x

8mm (L). The devices are wetted and blocked for non-specific binding using 0.5% Tween-20 in DI water. The hollow devices are left in a 4°C cold room in sealed petri dishes for 24 hours in order for the air pocket inside the hollow cavity to diffuse out. This occurs because PDMS is gas permeable, and boluses of fluid was left at the inlet and outlet of the channel to apply a slightly positive pressure towards the center of the channel. The degassing can be speeded up to around 1hr by actively applying a pressure source through the inlet whilst blocking the outlet. However, since there was only one pressure source, it was more efficient to prepare multiple devices using the passive pressure method. PDMS only devices are fabricated as in section 3.8. Particles used were 10μm polystyrene spheres (Duke Scientific) suspended in DI water with 0.1% Tween-20. They are injected at 10μL/min into the device using a syringe pump. Video analysis of the interception efficiency was performed as described in section 5.5.
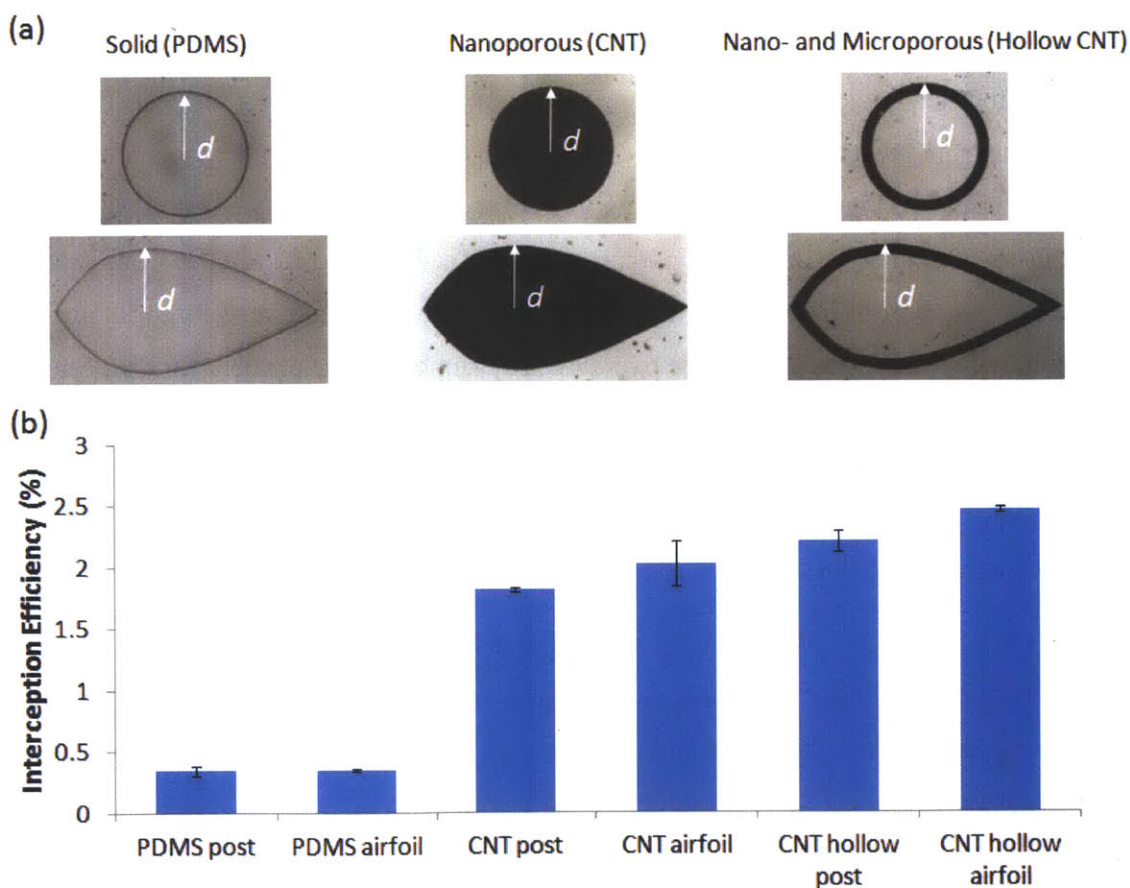
Fig. A-2: Inteception efficiencies for devices of different geometries. (a) pictures of the devices tested. d = 1mm for all geometries. (b) Interception efficiencies for 10μm particles for different device geometries.

100
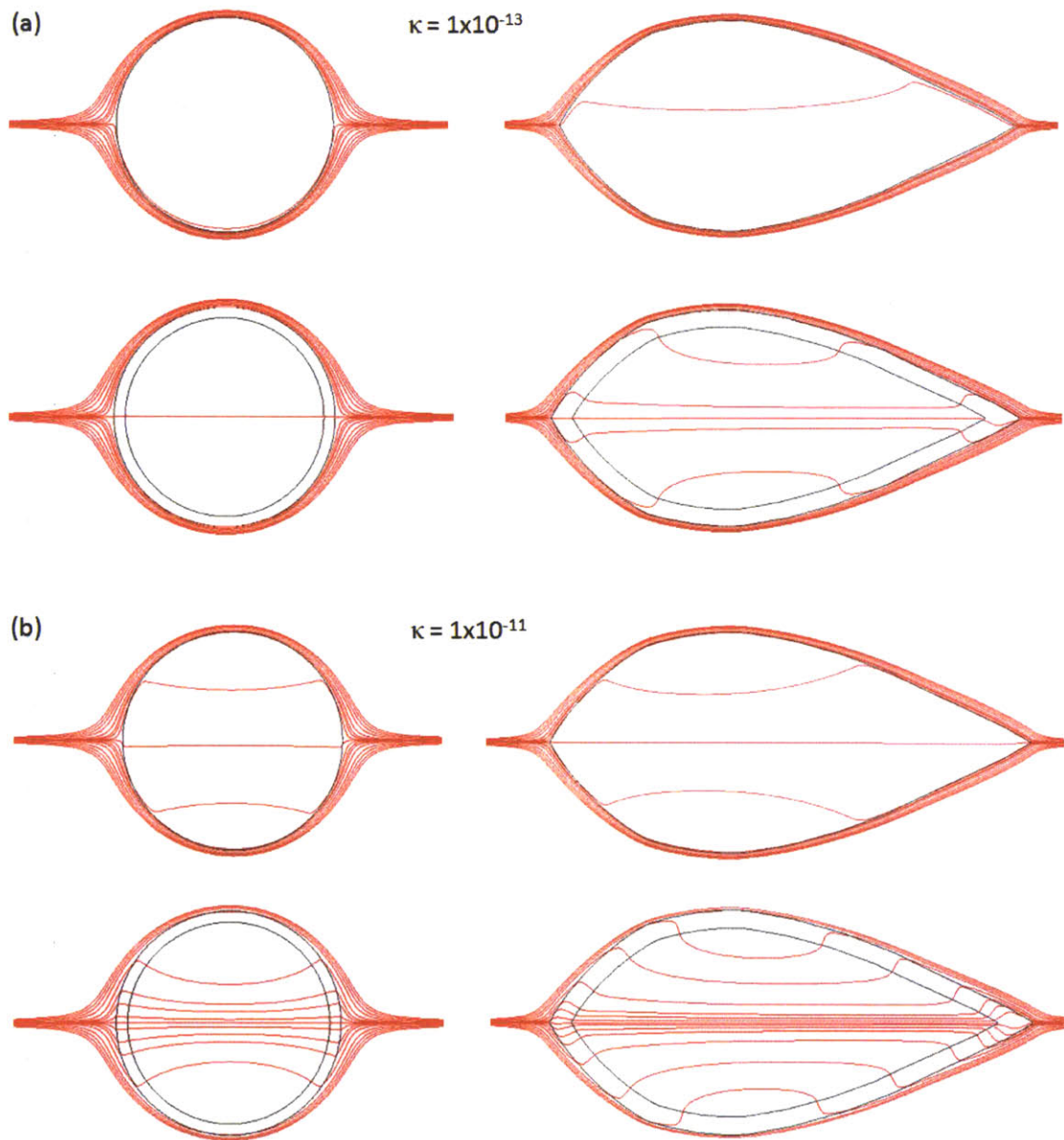
Fig. A-3: Model streamlines for 1mm wide posts of different geometries. (a) Streamlines for $\kappa = 1 \times 10^{-13}$, corresponding to a Darcy number of 10^{-7} for the 1mm diameter circular post. (b) Streamlines for $\kappa = 1 \times 10^{-11}$, corresponding to a Darcy number of 10^{-7} for the 1mm diameter circular post.

Figure A-2(b) shows interception efficiency results from the circular and airfoil elements for solid (PDMS), nanoporous (CNT), and nano- and microporous (hollow CNT) designs. It can be seen that, as previously observed, there is 5-fold improvement in interception going from the PDMS designs to the CNT circular post. The geometrical variations on the CNT designs showed

some efficiency increase, but only between 15% and 40%. To understand why the improvement is not as dramatic as we had hoped for, we look back at the streamline model for a circular post in figure 5.9. The 1mm posts we used for these experiments have a Darcy number of 10^{-7}. At this region of the curve, increases in Da by even 1 or 2 orders of magnitude only improves the interception efficiency slightly. Using equation (A.1), we see that a 1mm diameter 'hollow' post with a 50μm nanoporous shell has the same drag as a 300μm diameter 'full' post with the same permeability. This is equivalent to a Darcy number increase of 1 order of magnitude, which explains why we only saw a small improvement in interception efficiency. Modeling results in figure A-3(a) confirms our findings, and those in A-3(b) shows that if we can increase the material permeability of the nanoporous VACNT forests to $1 \times 10^{-11} \text{m}^2$, the same geometrical changes as in figure A-2 would result in much more dramatic interception efficiency increases. As discussed in section 6.2, much further work is needed using a combination of modeling and experiments to optimize device geometries for both interception and capture.

Bibliography

1.   Herzenberg, L.A., et al., *The history and future of the fluorescence activated cell sorter and flow cytometry: A view from Stanford.* Clinical Chemistry, 2002. **48**(10): p. 1819-1827.

2.   Di Carlo, D., et al., *Continuous inertial focusing, ordering, and separation of particles in microchannels.* Proceedings of the National Academy of Sciences of the United States of America, 2007. **104**(48): p. 18892-18897.

3.   Davis, J.A., et al., *Deterministic hydrodynamics: Taking blood apart.* Proceedings of the National Academy of Sciences of the United States of America, 2006. **103**(40): p. 14779-14784.

4.   Nilsson, J., et al., *Review of cell and particle trapping in microfluidic systems.* Analytica Chimica Acta, 2009. **649**(2): p. 141-157.

5.   Inglis, D.W., et al., *Microfluidic high gradient magnetic cell separation.* Journal of Applied Physics, 2006. **99**(8).

6.   Ramadan, Q., et al., *Magnetic-based microfluidic platform for biomolecular separation.* Biomedical Microdevices, 2006. **8**(2): p. 151-158.

7.   Wang, M.M., et al., *Microfluidic sorting of mammalian cells by optical force switching.* Nature Biotechnology, 2005. **23**(1): p. 83-87.

8.   Cheng, X.H., et al., *A microfluidic device for practical label-free CD4+T cell counting of HIV-infected subjects.* Lab on a Chip, 2007. **7**(2): p. 170-178.

9.   Chueh, B.-h., et al., *Leakage-free bonding of porous membranes into layered microfluidic array systems.* Analytical Chemistry, 2007. **79**(9): p. 3504-3508.

10.   Liu, J., et al., *Flow-through immunosensors using antibody-immobilized polymer monoliths.* Biosensors & Bioelectronics. **26**(1): p. 182-188.

11.   Hinds, B.J., et al., *Aligned multiwalled carbon nanotube membranes.* Science, 2004. **303**(5654): p. 62-65.

12.   Argus, A. *Particulate filtration theory.* 12/04/11]; Available from: http://www.argus-group.com/tech/pages/tech_app_niosh42.htm.

13.   Goren, S.L. and M.E. O'Neill, *On the hydrodynamic resistance to a particle of a dilute suspension when in the neighbourhood of a large obstacle.* Chemical Engineering Science, 1971. **26**(3): p. 325-338.

14.   Murthy, S.K., et al., *Effect of flow and surface conditions on human lymphocyte isolation using microfluidic chambers.* Langmuir, 2004. **20**(26): p. 11649-11655.

15. Adams, A.A., et al., *Highly efficient circulating tumor cell isolation from whole blood and label-free enumeration using polymer-based microfluidics with an integrated conductivity sensor.* Journal of the American Chemical Society, 2008. **130**(27): p. 8633-8641.

16. Kotz, K.T., et al., *Clinical microfluidics for neutrophil genomics and proteomics.* Nature Medicine, 2010. **16**(9): p. 1042-U142.

17. Wang, P.C., D.L. DeVoe, and C.S. Lee, *Integration of polymeric membranes with microfluidic networks for bioanalytical applications.* Electrophoresis, 2001. **22**(18): p. 3857-3867.

18. Yu, C., et al., *Preparation of monolithic polymers with controlled porous properties for microfluidic chip applications using photoinitiated free-radical polymerization.* Journal of Polymer Science Part a-Polymer Chemistry, 2002. **40**(6): p. 755-769.

19. Long, Z.C., et al., *Integration of nanoporous membranes for sample filtration/preconcentration in microchip electrophoresis.* Electrophoresis, 2006. **27**(24): p. 4927-4934.

20. Xiang, F., et al., *An integrated microfabricated device for dual microdialysis and on-line ESI ion trap mass spectrometry for analysis of complex biological samples.* Analytical Chemistry, 1999. **71**(8): p. 1485-1490.

21. Chon, K., et al., *Bio-particle separation using microfluidic porous plug for environmental monitoring.* Desalination, 2007. **202**(1-3): p. 215-223.

22. Throckmorton, D.J., T.J. Shepodd, and A.K. Singh, *Electrochromatography in microchips: Reversed-phase separation of peptides and amino acids using photopatterned rigid polymer monoliths.* Analytical Chemistry, 2002. **74**(4): p. 784-789.

23. Burg, T.P., et al., *Weighing of biomolecules, single cells and single nanoparticles in fluid.* Nature, 2007. **446**(7139): p. 1066-1069.

24. Lee, H., et al., *Chip-NMR biosensor for detection and molecular analysis of cells.* Nature Medicine, 2008. **14**(8): p. 869-874.

25. Patolsky, F., et al., *Electrical detection of single viruses.* Proceedings of the National Academy of Sciences of the United States of America, 2004. **101**(39): p. 14017-14022.

26. Gupta, A., D. Akin, and R. Bashir, *Single virus particle mass detection using microresonators with nanoscale thickness.* Applied Physics Letters, 2004. **84**(11): p. 1976-1978.

27. *http://www.findmall.com/read.php?40,792113.* 01/05/2012].

28. *http://www.cgenetool.com/products/beckman_ultracentrifuge.shtml.* 01/05/12].

29. Robards K, J.P., Haddad PR, *Principles and practice of modern chromatographic methods* 1ed1995: Academic press.

30. Snyder LR, K.J., Dolan JW, *Introduction to modern liquid chromatography*. 3 ed2009: Wiley.

31. Shapiro, A.L., E. Vinuela, and J.V. Maizel, *MOLECULAR WEIGHT ESTIMATION OF POLYPEPTIDE CHAINS BY ELECTROPHORESIS IN SDS-POLYACRYLAMIDE GELS.* Biochemical and Biophysical Research Communications, 1967. **28**(5): p. 815-&.

32. Kaltschm.E and H.G. Wittmann, *RIBOSOMAL PROTEINS .7. 2-DIMENSIONAL POLYACRYLAMIDE GEL ELECTROPHORESIS FOR FINGERPRINTING OF RIBOSOMAL PROTEINS.* Analytical Biochemistry, 1970. **36**(2): p. 401-&.

33. *http://www.bdbiosciences.com/research/stemcell/workflow/index.jsp.* 01/05/2012].

34. Haukanes, B.I. and C. Kvam, *APPLICATION OF MAGNETIC BEADS IN BIOASSAYS.* Bio-Technology, 1993. **11**(1): p. 60-63.

35. Miltenyi, S., et al., *HIGH-GRADIENT MAGNETIC CELL-SEPARATION WITH MACS.* Cytometry, 1990. **11**(2): p. 231-238.

36. Safarik, I. and M. Safarikova, *Use of magnetic techniques for the isolation of cells.* Journal of Chromatography B, 1999. **722**(1-2): p. 33-53.

37. Cuatreca.P, *PROTEIN PURIFICATION BY AFFINITY CHROMATOGRAPHY - DERIVATIZATIONS OF AGAROSE AND POLYACRYLAMIDE BEADS.* Journal of Biological Chemistry, 1970. **245**(12): p. 3059-&.

38. March, S.C., I. Parikh, and Cuatreca.P, *SIMPLIFIED METHOD FOR CYANOGEN-BROMIDE ACTIVATION OF AGAROSE FOR AFFINITY CHROMATOGRAPHY.* Analytical Biochemistry, 1974. **60**(1): p. 149-152.

39. Whitesides, G.M., *The origins and the future of microfluidics.* Nature, 2006. **442**(7101): p. 368-373.

40. Sethu, P., A. Sin, and M. Toner, *Microfluidic diffusive filter for apheresis (leukapheresis).* Lab on a Chip, 2006. **6**(1): p. 83-89.

41. Andersson, H., et al., *Micromachined flow-through filter-chamber for chemical reactions on beads.* Sensors and Actuators B-Chemical, 2000. **67**(1-2): p. 203-208.

42. Hamblin, M.N., et al., *Selective trapping and concentration of nanoparticles and viruses in dual-height nanofluidic channels.* Lab on a Chip, 2010. **10**(2): p. 173-178.

43. Russom, A., et al., *Differential inertial focusing of particles in curved low-aspect-ratio microchannels.* New Journal of Physics, 2009. **11**.

44.   Bhagat, A.A.S., S.S. Kuntaegowdanahalli, and I. Papautsky, *Enhanced particle filtration in straight microchannels using shear-modulated inertial migration.* Physics of Fluids, 2008. **20**(10).

45.   Huang, L.R., et al., *Continuous particle separation through deterministic lateral displacement.* Science, 2004. **304**(5673): p. 987-990.

46.   Ashkin, A. and J.M. Dziedzic, *OPTICAL TRAPPING AND MANIPULATION OF VIRUSES AND BACTERIA.* Science, 1987. **235**(4795): p. 1517-1520.

47.   Kovac, J.R. and J. Voldman, *Intuitive, image-based cell sorting using optofluidic cell sorting.* Analytical Chemistry, 2007. **79**(24): p. 9321-9330.

48.   Pohl, H.A., *THE MOTION AND PRECIPITATION OF SUSPENSOIDS IN DIVERGENT ELECTRIC FIELDS.* Journal of Applied Physics, 1951. **22**(7): p. 869-871.

49.   Voldman, J., et al., *A microfabrication-based dynamic array cytometer.* Analytical Chemistry, 2002. **74**(16): p. 3984-3990.

50.   Hughes, M.P. and H. Morgan, *Dielectrophoretic trapping of single sub-micrometre scale bioparticles.* Journal of Physics D-Applied Physics, 1998. **31**(17): p. 2205-2210.

51.   Lapizco-Encinas, B.H., et al., *Dielectrophoretic concentration and separation of live and dead bacteria in an array of insulators.* Analytical Chemistry, 2004. **76**(6): p. 1571-1579.

52.   Li, Y.L. and K. Kaler, *Dielectrophoretic fluidic cell fractionation system.* Analytica Chimica Acta, 2004. **507**(1): p. 151-161.

53.   Norris, J.V., et al., *Acoustic Differential Extraction for Forensic Analysis of Sexual Assault Evidence.* Analytical Chemistry, 2009. **81**(15): p. 6089-6095.

54.   Wiklund, M. and H.M. Hertz, *Ultrasonic enhancement of bead-based bioaffinity assays.* Lab on a Chip, 2006. **6**(10): p. 1279-1292.

55.   Neild, A., et al., *Simultaneous positioning of cells into two-dimensional arrays using ultrasound.* Biotechnology and Bioengineering, 2007. **97**(5): p. 1335-1339.

56.   Pamme, N., *Magnetism and microfluidics.* Lab on a Chip, 2006. **6**(1): p. 24-38.

57.   Chen, G.D., et al., *Concentration and Purification of Human Immunodeficiency Virus Type 1 Virions by Microfluidic Separation of Superparamagnetic Nanoparticles.* Analytical Chemistry, 2010. **82**(2): p. 723-728.

58.   Wolff, A., et al., *Integrating advanced functionality in a microfabricated high-throughput fluorescent-activated cell sorter.* Lab on a Chip, 2003. **3**(1): p. 22-27.

59.   Nagrath, S., et al., *Isolation of rare circulating tumour cells in cancer patients by microchip technology.* Nature, 2007. **450**(7173): p. 1235-U10.

60.   Phillips, J.A., et al., *Enrichment of Cancer Cells Using Aptamers Immobilized on a Microfluidic Channel.* Analytical Chemistry, 2009. **81**(3): p. 1033-1039.

61.   de Jong, J., R.G.H. Lammertink, and M. Wessling, *Membranes and microfluidics: a review.* Lab on a Chip, 2006. **6**(9): p. 1125-1139.

62.   Kim, J.E., J.H. Cho, and S.H. Paek, *Functional membrane-implanted lab-on-a-chip for analysis of percent HDL cholesterol.* Analytical Chemistry, 2005. **77**(24): p. 7901-7907.

63.   Chirica, G., J. Lachmann, and J. Chan, *Size exclusion chromatography of microliter volumes for on-line use in low-pressure microfluidic systems.* Analytical Chemistry, 2006. **78**(15): p. 5362-5368.

64.   Sun, X., et al., *Affinity monolith integrated poly(methyl methacrylate) microchips for on-line protein extraction and capillary electrophoresis.* Analytical Chemistry, 2008. **80**(13): p. 5126-5130.

65.   Mallik, R. and D.S. Hage, *Affinity monolith chromatography.* Journal of Separation Science, 2006. **29**(12): p. 1686-1704.

66.   Uhlir, A., *ELECTROLYTIC SHAPING OF GERMANIUM AND SILICON.* Bell System Technical Journal, 1956. **35**(2): p. 333-347.

67.   Bomchil, G., A. Halimaoui, and R. Herino, *POROUS SILICON - THE MATERIAL AND ITS APPLICATIONS IN SILICON ON INSULATOR TECHNOLOGIES.* Applied Surface Science, 1989. **41-2**: p. 604-613.

68.   Lysenko, V., et al., *Gas permeability of porous silicon nanostructures.* Physical Review E, 2004. **70**(1).

69.   Shen, Z.X., et al., *Porous silicon as a versatile platform for laser desorption/ionization mass spectrometry.* Analytical Chemistry, 2001. **73**(3): p. 612-619.

70.   DeLouise, L.A. and B.L. Miller, *Enzyme immobilization in porous silicon: Quantitative analysis of the kinetic parameters for glutathione-S-transferases.* Analytical Chemistry, 2005. **77**(7): p. 1950-1956.

71.   Dancil, K.P.S., D.P. Greiner, and M.J. Sailor, *A porous silicon optical biosensor: Detection of reversible binding of IgG to a protein A-modified surface.* Journal of the American Chemical Society, 1999. **121**(34): p. 7925-7930.

72.   Liu, Z., et al., *Carbon Nanotubes in Biology and Medicine: In vitro and in vivo Detection, Imaging and Drug Delivery.* Nano Research, 2009. **2**(2): p. 85-120.

73.   Balasubramanian, K. and M. Burghard, *Chemically functionalized carbon nanotubes.* Small, 2005. **1**(2): p. 180-192.

74.   Chen, R.J., et al., *Noncovalent functionalization of carbon nanotubes for highly specific electronic biosensors*. Proceedings of the National Academy of Sciences of the United States of America, 2003. **100**(9): p. 4984-4989.

75.   Maehashi, K., et al., *Label-free protein biosensor based on aptamer-modified carbon nanotube field-effect transistors*. Analytical Chemistry, 2007. **79**(2): p. 782-787.

76.   Star, A., et al., *Electronic detection of specific protein binding using nanotube FET devices*. Nano Letters, 2003. **3**(4): p. 459-463.

77.   Shao, N., E. Wickstrom, and B. Panchapakesan, *Nanotube-antibody biosensor arrays for the detection of circulating breast cancer cells*. Nanotechnology, 2008. **19**(46).

78.   Yu, X., et al., *Protein immunosensor using single-wall carbon nanotube forests with electrochemical detection of enzyme labels*. Molecular Biosystems, 2005. **1**(1): p. 70-78.

79.   Kam, N.W.S., et al., *Nanotube molecular transporters: Internalization of carbon nanotube-protein conjugates into mammalian cells*. Journal of the American Chemical Society, 2004. **126**(22): p. 6850-6851.

80.   Chen, J.Y., et al., *Functionalized Single-Walled Carbon Nanotubes as Rationally Designed Vehicles for Tumor-Targeted Drug Delivery*. Journal of the American Chemical Society, 2008. **130**(49): p. 16778-16785.

81.   Cai, D., et al., *Highly efficient molecular delivery into mammalian cells using carbon nanotube spearing*. Nature Methods, 2005. **2**(6): p. 449-454.

82.   Kam, N.W.S., Z. Liu, and H.J. Dai, *Functionalization of carbon nanotubes via cleavable disulfide bonds for efficient intracellular delivery of siRNA and potent gene silencing*. Journal of the American Chemical Society, 2005. **127**(36): p. 12492-12493.

83.   Gannon, C.J., et al., *Carbon nanotube-enhanced thermal destruction of cancer cells in a noninvasive radiofrequency field*. Cancer, 2007. **110**(12): p. 2654-2665.

84.   Fan, Z.J., et al., *Electromagnetic and microwave absorbing properties of multi-walled carbon nanotubes/polymer composites*. Materials Science and Engineering B-Solid State Materials for Advanced Technology, 2006. **132**(1-2): p. 85-89.

85.   Nednoor, P., et al., *Carbon nanotube based biomimetic membranes: Mimicking protein channels regulated by phosphorylation*. Journal of Materials Chemistry, 2007. **17**(18): p. 1755-1757.

86.   Garcia, E.J., et al., *Fabrication of composite microstructures by capillarity-driven wetting of aligned carbon nanotubes with polymers*. Nanotechnology, 2007. **18**(16).

87.   Fachin, F., *3DMEMS via (Post-)Buckling of Micromachined Structures and*

Integration of Bulk Nanoporous Elements inMicrofluidic Devices, in *Aeronautics and Astronautics*2011, Massachusetts Institute of Technology: Cambridge, MA.

88.   Wardle, B.L., et al., *Fabrication and characterization of ultrahigh-volume-fraction aligned carbon nanotube-polymer composites.* Advanced Materials, 2008. **20**(14): p. 2707-+.

89.   McDonald, J.C. and G.M. Whitesides, *Poly(dimethylsiloxane) as a material for fabricating microfluidic devices.* Accounts of Chemical Research, 2002. **35**(7): p. 491-499.

90.   Vaddiraju, S., et al., *Hierarchical Multifunctional Composites by Conformally Coating Aligned Carbon Nanotube Arrays with Conducting Polymer.* Acs Applied Materials & Interfaces, 2009. **1**(11): p. 2565-2572.

91.   Joseph, P., et al., *Slippage of water past superhydrophobic carbon nanotube forests in microchannels.* Physical Review Letters, 2006. **97**(15).

92.   De Volder, M., et al., *Diverse 3D Microarchitectures Made by Capillary Forming of Carbon Nanotubes.* Advanced Materials, 2010. **22**(39): p. 4384-+.

93.   Futaba, D.N., et al., *Shape-engineerable and highly densely packed single-walled carbon nanotubes and their application as super-capacitor electrodes.* Nature Materials, 2006. **5**(12): p. 987-994.

94.   Lee, S.L. and J.H. Yang, *Modeling of Darcy-Forchheimer drag for fluid flow across a bank of circular cylinders.* International Journal of Heat and Mass Transfer, 1997. **40**(13): p. 3149-3155.

95.   Urban, J. and P. Jandera, *Polymethacrylate monolithic columns for capillary liquid chromatography.* Journal of Separation Science, 2008. **31**(14): p. 2521-2540.

96.   Neeves, K.B. and S.L. Diamond, *A membrane-based microfluidic device for controlling the flux of platelet agonists into flowing blood.* Lab on a Chip, 2008. **8**(5): p. 701-709.

97.   Du, K.F., D. Yang, and Y. Sun, *Fabrication of high-permeability and high-capacity monolith for protein chromatography.* Journal of Chromatography A, 2007. **1163**(1-2): p. 212-218.

98.   Fletcher, P.D.I., et al., *Permeability of silica monoliths containing micro- and nanopores.* Journal of Porous Materials, 2010. **18**(4): p. 501-508.

99.   Vafai, K., *Handbook of porous media*2005: Taylor and Francis.

100.   Ergun, S., *Fluid Flow through Packed Columns.* Chemical Engineering Progress, 1952. **48**(2): p. 89-94.

101. Hart, A.J., *Chemical, mechanical, and thermal control of substrate-bound carbon nanotube growth*, in *Aeronautics and Astronautics*2006, Massachusetts Institute of Technology: Cambridge, MA.

102. Yamamoto, N., et al., *High-yield growth and morphology control of aligned carbon nanotubes on ceramic fibers for multifunctional enhancement of structural composites.* Carbon, 2009. **47**(3): p. 551-560.

103. Wei, Y.Y., et al., *Effect of catalyst film thickness on carbon nanotube growth by selective area chemical vapor deposition.* Applied Physics Letters, 2001. **78**(10): p. 1394-1396.

104. Katz, E. and I. Willner, *Biomolecule-functionalized carbon nanotubes: Applications in nanobioelectronics.* Chemphyschem, 2004. **5**(8): p. 1085-1104.

105. Daniel, S., et al., *A review of DNA functionalized/grafted carbon nanotubes and their characterization.* Sensors and Actuators B-Chemical, 2007. **122**(2): p. 672-682.

106. Bahr, J.L. and J.M. Tour, *Covalent chemistry of single-wall carbon nanotubes.* Journal of Materials Chemistry, 2002. **12**(7): p. 1952-1958.

107. Guo, Z.J., P.J. Sadler, and S.C. Tsang, *Immobilization and visualization of DNA and proteins on carbon nanotubes.* Advanced Materials, 1998. **10**(9): p. 701-703.

108. Azamian, B.R., et al., *Bioelectrochemical single-walled carbon nanotubes.* Journal of the American Chemical Society, 2002. **124**(43): p. 12664-12665.

109. Shim, M., et al., *Functionalization of carbon nanotubes for biocompatibility and biomolecular recognition.* Nano Letters, 2002. **2**(4): p. 285-288.

110. Chen, R.J., et al., *Noncovalent sidewall functionalization of single-walled carbon nanotubes for protein immobilization.* Journal of the American Chemical Society, 2001. **123**(16): p. 3838-3839.

111. Pulley, R.A. and J.K. Walters, *The Effect of Interception on Particle Collection by Spheres and Cylinders.* Journal of Aerosol Science, 1990. **21**(6): p. 733-743.

112. Wessel, R.A. and J. Righi, *Generalized Correlations for Inertial Impaction of Particles on a Circular-Cylinder.* Aerosol Science and Technology, 1988. **9**(1): p. 29-60.

113. Shimeta, J. and P.A. Jumars, *Physical-Mechanisms and Rates of Particle Capture by Suspension-Feeders.* Oceanography and Marine Biology, 1991. **29**: p. 191-257.

114. Palmer, M.R., H.M. Nepf, and T.J.R. Pettersson, *Observations of particle capture on a cylindrical collector: Implications for particle accumulation and removal in aquatic systems.* Limnology and Oceanography, 2004. **49**(1): p. 76-85.

115. Spielman, L.A., *Particle Capture from Low-Speed Laminar Flows.* Annual Review of Fluid Mechanics, 1977. **9**: p. 297-319.

116. Probstein, R.F., *Physicochemical Hydrodynamics: An Introduction*2005: Frontmatter.

117. Schrijver, J.H.M., C. Vreeken, and J.A. Wesselingh, *Deposition of Particles on a Cylindrical Collector.* Journal of Colloid and Interface Science, 1981. **81**(1): p. 249-256.

118. Spielman, L.A. and Fitzpatr.Ja, *Theory for Particle Collection under London and Gravity Forces.* Journal of Colloid and Interface Science, 1973. **42**(3): p. 607-623.

119. Chang, D.P.Y., *Particle collection from aqeous suspensions by solid and hollow fibers*, 1973, California Institute of Technology.

120. Yamamoto, K., *Flow of Viscous-Fluid at Small Reynolds-Numbers Past a Porous Body.* Journal of the Physical Society of Japan, 1973. **34**(3): p. 814-820.

121. Verma, P.D. and B.S. Bhatt, *Flow past a porous circular cylinder at small reynolds number.* Proc. Ind. Acad. Sci. A, 1973. **8**(8): p. 908-914.

122. Yu, P., et al., *Steady flow around and through a permeable circular cylinder.* Computers & Fluids, 2009. **42**(1): p. 1-12.

123. Bhattacharyya, S., S. Dhinakaran, and A. Khalili, *Fluid motion around and through a porous cylinder.* Chemical Engineering Science, 2006. **61**(13): p. 4451-4461.

124. Brinkman, H.C., *A Calculation of the Viscous Force Exerted by a Flowing Fluid on a Dense Swarm of Particles.* Applied Scientific Research Section a-Mechanics Heat Chemical Engineering Mathematical Methods, 1947. **1**(1): p. 27-34.

125. Padmavathi, B.S. and T. Amaranath, *A Solution for the Problem of Stokes-Flow Past a Porous Sphere.* Zeitschrift Fur Angewandte Mathematik Und Physik, 1993. **44**(1): p. 178-184.

126. Beavers, G.S. and D.D. Joseph, *Boundary Conditions at a Naturally Permeable Wall.* Journal of Fluid Mechanics, 1967. **30**: p. 197-&.

127. Jones, I.P., *Low Reynolds-Number Flow Past a Porous Spherical Shell.* Proceedings of the Cambridge Philosophical Society, 1973. **73**(JAN): p. 231-238.

128. Ochoatapia, J.A. and S. Whitaker, *Momentum-Transfer at the Boundary between a Porous-Medium and a Homogeneous Fluid .1. Theoretical Development.* International Journal of Heat and Mass Transfer, 1995. **38**(14): p. 2635-2646.

129. Partha, M.K., P. Murthy, and G.P.R. Sekhar, *Viscous flow past a porous spherical shell - Effect of stress jump boundary condition.* Journal of Engineering Mechanics-Asce, 2005. **131**(12): p. 1291-1301.

130. Kuznetsov, A.V., *Influence of the stress jump condition at the porous-medium/clear-fluid interface on a flow at a porous wall.* International Communications in Heat and Mass Transfer, 1997. **24**(3): p. 401-410.

131.   Verma, P.D. and B.S. Bhatt, *Flow past a porous circular cylinder at small reynolds number.* Proc. Ind. Acad. Sci. A, 1977. **8**(8): p. 908-914.

132.   Noymer, P.D., L.R. Glicksman, and A. Devendran, *Drag on a permeable cylinder in steady flow at moderate Reynolds numbers.* Chemical Engineering Science, 1998. **53**(16): p. 2859-2869.

133.   Visser, J., *On Hamaker constants: A comparison between Hamaker constants and Lifshitz-van der Waals constants.* Advances in Colloid and Interface Science, 1972. **3**(4): p. 331-363.

134.   Farhoud, M., et al., *Fabrication of 200 nm period nanomagnet arrays using interference lithography and a negative resist.* Journal of Vacuum Science & Technology B, 1999. **17**(6): p. 3182-3185.

135.   Singh, M.P. and J.L. Gupta, *The Flow of a Viscous Fluid Past an Inhomogeneous Porous Cylinder.* ZAMM, 1971. **51**: p. 17-25.